P-85
304452

NASA
Technical
Paper
2786

May 1988

Gas-Jet and Tangent-Slot Film Cooling Tests of a 12.5° Cone at Mach Number of 6.7

Robert J. Nowak

NASA

NASA Technical Paper 2786

1988

Gas-Jet and Tangent-Slot Film Cooling Tests of a 12.5° Cone at Mach Number of 6.7

Robert J. Nowak

Langley Research Center
Hampton, Virginia

National Aeronautics and Space Administration

Scientific and Technical Information Division

Summary

An experimental investigation was conducted in the Langley 8-Foot High-Temperature Tunnel at a Mach number of 6.7 to determine the effects of gaseous nitrogen ejection on the aerothermal environment of a 3-ft-diameter base, 12.5° half-angle conical model. The free-stream total temperature and unit Reynolds number per foot were 3300°R and 1.4×10^6, respectively. (The total temperature is a nearly true temperature simulation for a Mach number of 6.7.) Two mass addition noses were tested; one was an ogive frustum with a forward-facing 0.8-in-radius gas jet tip, and the other was a 3-in-radius hemispherical tip with a 0.243-in-high rearward-facing tangential slot. The gas-jet configuration was tested at angles of attack from 0° to 10°, but the tangent-slot configuration was tested at only an angle of attack of 0°. Data include model surface pressures and wall heating rates, shock shapes, and shock-layer profiles of static pressure, pitot pressure, total temperature, and calculated Mach numbers. The data with coolant are compared with baseline data (no cooling) obtained with 1-in- and 3-in-radius solid nose tips.

Model surface pressures were reduced with the gas-jet coolant ejection, due partly to apparent increased nose bluntness; but model pressures were affected little by coolant ejection through the rearward-facing slot. For the gas jet, high coolant flow rates were effective in reducing the heat flux far downstream of the orifice; however, low coolant flow rates caused apparent transition to turbulence and increased the heating. For the tangent slot, high coolant flow rates were effective in reducing the heating far downstream from the slot; low coolant flow rates apparently caused immediate transition downstream of the slot with slightly increased heating. Shock-layer profiles show significant reductions, compared with baseline data, of pitot pressure, Mach number, and total temperature even far downstream from the region of coolant ejection for both gas-jet and tangent-slot noses. Shadowgraphs and schlierens of both the gas-jet and the tangent-slot noses indicate that the coolant flow field interactions were basically steady with only small fluctuations for the gas jet and were similar to those observed by other experimenters. Insight into the gas-jet heat-flux mechanisms was obtained by using the measured shock-layer rake data with established semiempirical (no-cooling) heat-transfer methods.

Introduction

Mass addition film cooling (forced ejection of a fluid from the surface) is an effective method of providing thermal protection from hostile aerodynamic heating. Film cooling is an active system that could supplement passive thermal protection systems in local areas experiencing excessive heating loads. Although many experimental and analytical studies have been conducted on film cooling (for example, refs. 1 through 5), little experimental data exist for high-temperature hypersonic flow conditions. To add to the high-temperature test stream film-cooling data base, a test program was conducted in the Langley 8-Foot High-Temperature Tunnel to study the cooling effectiveness of ejection of gaseous nitrogen coolant through both a forward-facing orifice and a rearward-facing tangent slot.

A large 12.5° half-angle cone, 3-ft base diameter, with interchangeable nose shapes was tested at a free-stream Mach number of 6.7, a near flight simulation total temperature of 3300°R, and a free-stream unit Reynolds number per foot of 1.4×10^6. The two coolant ejection shapes tested were the gas jet, an ogive frustum with a forward-facing 0.8-in-radius orifice; and the tangent slot, a 3-in-radius hemispherical tip with a 0.243-in-high rearward-facing tangential slot. The gas jet was tested at angles of attack from 0° to 10°, but the tangent-slot configuration was only tested at an angle of attack of 0° because of time constraints on the test program. Two no-cooling nose shapes consisting of a 3-in-radius tip and a 1-in-radius tip on the ogive frustum were tested to provide baseline (no-cooling) data; the results from these tests were reported in reference 6. The advantages of testing the large conical model were the capability of obtaining cooling effects data far downstream from the region of coolant ejection, and the capability of incorporating three sets of rakes that measured shock-layer static and pitot pressures and total temperatures. Model surface pressures and heat-flux distributions, shock shapes, and shock-layer profiles were obtained over a range of coolant flow rates.

The purpose of this paper is to present the data obtained with the coolant ejection nose shapes and to compare the data with the baseline (no-cooling) data which were reported in reference 6. Both plots and tables of the data are given along with details of the flow conditions so that additional parametric comparisons can be made. The baseline data are compared with predictions in reference 6. Existing semiempirical heat-transfer relations plus shock-layer data are used to give insight into the gas-jet heat-flux mechanisms. Some data with coolant including shock shapes were compared with a sophisticated prediction method in reference 7.

Symbols

A	area, in^2
B	nondimensional orifice plate geometry parameter
C	nondimensional orifice discharge coefficient
c_p	specific heat, Btu/lbm-°R
$f(T)$	temperature-dependent terms in h (see eq. (12))
h	convective heat-transfer coefficient, Btu/ft^2-sec-°R
I.D.	inside diameter
k	thermal conductivity, Btu-in/ft^2-hr-°R
L	surface length of sharp cone, 83.16 in. (fig. 7)
M	Mach number
$\dot{m}$	coolant flow rate, lbm/sec
O.D.	outside diameter
Pr	Prandtl number, $c_p\mu/k$
p	pressure, psia
$\dot{q}$	heat flux, Btu/ft^2-sec
$\dot{q}_s$	calculated 1-in-radius stagnation-point heat flux, Btu/ft^2-sec
R	gas constant, ft-lbf/lbm-°R
Re	unit Reynolds number per foot, $\rho V/\mu$
r_n	effective nose radius, in.
St	Stanton number, $h/\rho V c_p$
s	surface distance from stagnation point, in. (fig. 7)
s_a	surface distance from sharp cone apex, in. (fig. 7)
s_c	surface distance from start of cone frustum, in. (fig. 7)
T	temperature, °R
t	time, sec
V	velocity, ft/sec
x	axial distance from stagnation point to nose, in.
α	angle of attack, deg
γ	ratio of specific heats
η	distance normal to surface, in. (fig. 7)
μ	viscosity, lbm/ft-sec
ϕ	circumferential angle, deg (fig. 8)
ρ	density, lbm/ft^3
τ	skin thickness, in.

Subscripts:

aw	recovery or adiabatic wall
c	coolant condition
e	boundary-layer edge conditions
o	total condition
s	stagnation point
t	free-stream total conditions
tg	tunnel test gas
w	model wall
1	conditions upstream of coolant flow-rate orifice plate
2	conditions downstream of coolant flow-rate orifice plate

Superscript:

*	conditions at reference temperature (see eq. (7))

Apparatus and Tests

Model

The model, shown in figure 1 mounted in the test section of the Langley 8-Foot High-Temperature Tunnel, consisted of a cone frustum, interchangeable nose tips, three shock-layer survey rakes, and a boat-tail base. The structure of the model is shown in figure 2. The cone frustum was 63.43 in. long with a 3-ft-diameter base and a 12.5° half-angle. This frustum consisted of a 0.060- (± 0.003) in-thick René 41 skin supported by a load-bearing structural shell. The skin was attached to the structural shell only at the forward end of the frustum which was threaded for attaching the noses. The skin was supported by the shell through five support rings. These support rings were made of segmented insulated pads interconnected by a spring-loaded mechanism that allowed the rings to expand as the skin expanded upon heating. This mechanism was designed to allow the skin to reach temperatures up to about 1800°R without buckling. A 1-in-thick blanket of high-temperature insulation was strapped to the structural shell between the rings, as shown in figure 2, to reduce heat losses from the skin. The surface contour of the skin was measured and found to have a concave depression of about 0.050 in. at 24 in. from the front of the cone frustum. The outside surface of the skin was painted to provide a uniform surface emissivity (0.8 ± 0.1). Details of the coolant manifold are given in the section "Cooling System."

The boattail cover shown in figure 2 had a 19.7° half-angle, was 36.3 in. long, and was made from 0.13-in-thick stainless steel. The purpose of the boattail was to protect the instrumentation wires and the remote multiplexed data system from the base flow. Additional details of the remote multiplexed data system are given in reference 6. The rear of the boattail was attached to the sting, and the front was supported, but not restrained, by an aluminum ring. A 0.30-in. gap between the boattail and the cone frustum and a 0.15-in. backward-facing step allowed thermal growth and venting of the model during the entire test sequence. (See detail in fig. 2.)

The present paper gives results from tests with the model using the four noses that attached to the front of the model. Two of the noses are baseline (no cooling). The results from the baseline tests were also reported in more detail in reference 6; in that report, the results from a sharp tip were also given but are not used in the present report. The two baseline (no-coolant) noses are shown in figure 3. The nose shown in figure 3(a) has a 3-in-radius spherical tip, attached to a 12.5° half-angle frustum adapter, and is made from 0.9-in-thick mild steel. Surface pressure taps were located at wetted surface distances s of 0, 1.31, 2.62, 4.06, and 6.06 in.; pressure data are presented in reference 6. This nose configuration is referred to in the report as "nose R-3." (R designates radius and the 3 designates the nose radius in inches.) The nose shown in figure 3(b), referred to as "nose R-1," has a solid 1-in-radius spherical tip of stainless steel with a 0.040-in-I.D. stagnation-point pressure tube. This tip was attached to a (measured) 0.083- ($\pm$ 0.001) in-thick stainless-steel ogive frustum which has an 84.43-in. radius. (In reference 6, the ogive radius was incorrectly given as 74.15-in.) The 1-in-radius tip was internally spring mounted to allow thermal growth of the ogive shell without deformations (the spring is shown schematically in fig. 4). High-temperature insulation was placed against the inside of the ogive skin to reduce heat losses. All the junctions between each of the model segments were smooth except for the ogive frustum where the base was oversized resulting in a rearward-facing step about 0.023 in. (In ref. 6, the rearward-facing step was incorrectly given as 0.005 in.)

The gas-jet nose is shown in figure 4. A forward-facing straight orifice tube, made of stainless steel, with an internal radius of 0.800 in., and a sharp 0.032-in-thick lip replaced the 1-in-radius solid tip of nose R-1. The rear of the orifice tube screwed into a spring-loaded floating coupling; thus, the ogive skin, which was pinned only at the rear, was free to thermally expand by compressing the springs. (Posttest inspection of the ogive revealed no evidence of skin deformations.) At the front of the 12.5° cone threaded internal structural shell, the coolant manifold was attached and sealed with O-rings, the rear of the orifice tube was also sealed with an O-ring.

The tangent-slot nose was shown in figure 5. It had the same external radius, 3.00 in., as the R-3 nose, but it was 1.35 in. longer to accommodate the rearward-facing slot. The skin was made of 0.040- ($\pm$ 0.005) in-thick René 41; the measured internal height of the exit slot was a mean 0.243 in., with a standard deviation of 0.010 in. The calculated mean slot exit area is 5.638 in^2. Forty-two straight fins plus six rods supported the skin. The 0.006-in-thick fins were spaced approximately 0.5 in. apart. The surface distance from the stagnation point to the slot lip was 7.73 in. (No manifold pitot probe is shown because it broke off during the first test with the gas-jet nose which was tested prior to the tangent-slot nose.)

Instrumentation

Survey rakes. Three sets of rake assemblies were used to survey the flow within the shock layer at three axial stations. Photographs of a rake assembly extended from the surface and retracted are shown in figure 6(a). Each rake consisted of three parallel struts spaced 1.245 in. apart, a cover plate with a sharp beveled edge, and a floor plate with two static-pressure orifices between the struts. (See fig. 6(b).) Each strut contained either five pitot-pressure tubes, five sharp conical-tip static-pressure probes, or five stagnation-temperature probes. The center strut was perpendicular to the surface. The heights of the probes above the surface on each of the struts were 0.20, 0.45, 0.82, 1.25, and 1.75 in. Since the struts were parallel, the struts of the static pressure and temperature probes were not normal to the surface; the angles that these two struts made with the normal were 10.8°, 5.1°, and 4.3° for rakes 1, 2, and 3, respectively. These angles resulted in normal distant errors for the static pressure and temperature probes of 1.8, 0.4, and 0.3 percent for rakes 1, 2, and 3, respectively. Data plots were not corrected for these percentage errors. The pitot probes were 0.50 in. long from the leading edge of the strut to the orifice and had a flat edge with 0.060-in. O.D. and a 0.040-in. I.D. The static-pressure probes had a 7.1° half-angle conical tip with overall length of 1.38 in. and 0.060-in. O.D. Two sets of two 0.020-in-diameter orifices spaced 90° apart and staggered 0.020 in. axially were a mean distance of 0.87 in. from the leading edge of the strut. Platinum versus platinum + 13-percent-rhodium thermocouple (30-gage wire, 0.010-in. diameter) beads with single shielding platinum tubes were used for the temperature probes. These flat edge platinum shields were 0.090 in. O.D. and 0.072 in. I.D., and the end of each shield was 0.5 in. from the leading edge of the strut. The 0.017-in-diameter bead was 0.093 in. from the end of the platinum shield; four 0.0176-in-diameter vent holes, 90° apart were 0.031 in. from the end of the platinum shield. Each rake was injected into the flow field of the cone by a double-acting pneumatic piston. Local thermal distortions of the rake assembly sometimes prevented a rake from fully extending into the flow; thus, rake data were not obtained for several model runs. Additional information on the rake assemblies can be found in reference 6.

Model. The inside surface of the René 41 skin of the cone frustum was instrumented with 101 Chromel-Alumel 30-gage thermocouples and 30 surface pressure orifices. The circumferential angular position ϕ and the surface distance s_a measured from the apex of a sharp 12.5° cone are used to locate surface pressure orifices and thermocouples. Figure 7 gives the instrumentation coordinate system. The distance s_a to an instrument on the cone surface thus is the same for each nose. The coordinates for the instrumentation on the cone frustum and on the noses are given in tables I and II; and the thermocouple, pressure orifices, and rake locations are shown schematically in figure 8(a). The thermocouples (denoted by T) are located at increments of 22.5° and the pressure orifices (denoted by p) are at increments of 45°. The pressure tubes, 0.090 in. O.D. and 0.060 in. I.D., were welded to the inside of the skin of the cone frustum and connected to strain-gage-type pressure transducers located within the model. Each tube was leak checked after installation. Two pressure tubes, one on the most windward and one on the most leeward rays, were attached to the boattail skin 3 in. from the base of the cone to measure the base pressure of the model.

Noses. The ogive frustum used for nose R-1 and the gas jet contained 24 Chromel-Alumel 30-gage thermocouples spot-welded to the inside surface along three longitudinal rays (fig. 8(b)). Nose R-1 also had a single pressure orifice at the stagnation point on the axis of symmetry. To measure the coolant exit conditions, the tangent-slot nose was instrumented at the slot exit plane with two pressure orifices and four 28-gage beaded thermocouples on the 2.31-in-long adapter ring, as noted in the detail in figure 5. The two 0.040-in-I.D. static-pressure orifices were located at the exit plane of the slot at $\phi = 0°$ and 180°. The four thermocouple beads were at the exit plane at half the slot height—one each at $\phi = -90°$ and +90°, one at $\phi = 16°$, and one at $\phi = -164°$.

Cooling System

A simplified schematic of the cooling system is shown in figure 9(a). Dry nitrogen was stored at about 5000 psi. A regulator controlled the flow rate of the nitrogen and the pressure drop to be able to deliver the nitrogen at the required flow rate and pressure at the manifold. (See fig. 9(b) for manifold details.) Three orifice plates designed according to ASME standards (ref. 8) were used to accurately measure the range of coolant flow rates. The orifice plates were calibrated in place against a precision venturi nozzle which was connected to the coolant supply line inside the tunnel test section. This was done before the model and coolant manifold were installed in the tunnel. (The venturi nozzle was laboratory calibrated against a standard, traceable to the National Bureau of Standards, and found to be accurate to ±0.3 percent.) Thus the entire cooling system was in place for calibration of the orifice plates with the exception of the coolant manifold (inside the model) and the noses. After calibration of the orifice plates and installation of the model and the gas-jet nose, the entire cooling system was again leak checked by plugging the exit orifice of the gas-jet nose.

The coolant manifold (fig. 9(b)) consisted of a 15.0-in-long by 2.87-in-I.D. stainless-steel cylinder. Inside the manifold, just downstream of its entrance tube were two flow-straightener plates, each with 61 0.173-in-diameter holes; the holes in the two straightener plates were in line. The 11° angle on the inlet tube (fig. 9(b)) was required to avoid interference with the rake 1 mechanism. The nitrogen coolant temperature was measured with a Chromel-Alumel thermocouple located downstream of the entrance tube but ahead of the flow-straightener plates. The coolant exit pitot and static pressures were measured downstream of the flow straighteners, 0.9-in. prior to the exit end of the manifold. (The pitot tube broke at the wall during the first coolant test with the ogive; however, sufficient data were obtained to show that at the highest coolant flow rate of 4.6 lbm/sec the static pressure was within approximately 94 percent of the pitot pressure.)

The coolant flow rate was calculated from the following orifice plate equation which can be obtained from reference 8:

$$\dot{m} = 1.08ABC\left[\frac{p_1(p_1 - p_2)}{T_1}\right]^{0.5} \tag{1}$$

where A is the area of the orifice, B is a function of the ratio of the orifice to the pipe diameter, and C is the discharge coefficient which was obtained by calibration of the orifice plates against the precision venturi. Equation (1) includes the condition that nitrogen obeys the perfect gas law and that $\gamma = 1.4$. The venturi nozzle equation can also be found in reference 8; it is

$$\dot{m} = 0.523Ap_oT_o^{-0.5} \tag{2}$$

where A is the area at the throat, and the coefficient includes the assumption of a discharge coefficient of 1.0 and the perfect gas assumption for nitrogen. The total condition, subscript o, refers to the coolant manifold.

In order to periodically check the functioning of the orifice plates and associated instrumentation (fig. 9(a)), equation (2) was applied to conditions at the gas-jet exit orifice and the tangent-slot exit plane. By assuming a discharge coefficient of 1.0 and sonic flow at the exit, equation (2) gave agreement within 4 percent of equation (1).

Test Facility

The Langley 8-Foot High-Temperature Tunnel (fig. 10) is a large blowdown tunnel that simulates aerodynamic heating and pressure loading for a nominal Mach number of 7 at altitudes between 80 000 and 120 000 ft. The high energy needed for simulation is obtained by burning a mixture of methane and air under pressure in the combustor and expanding the products of combustion through a conical-contoured nozzle into the open-jet test chamber. The flow enters a supersonic diffuser where it is pumped by an air ejector through a mixing tube and exhausted to the atmosphere through a subsonic diffuser. The tunnel operates at total temperatures from 2400°R to 3600°R, free-stream dynamic pressure from 250 to 1800 psf, free-stream unit Reynolds number per foot from 0.3×10^6 to 2.2×10^6, and has a maximum run time of 120 sec.

The 12.5° cone model was stored in the pod below the test stream to protect it from adverse tunnel start-up loads. Once the desired flow conditions were established, the model was inserted into the test stream on a hydraulically actuated elevator. Insertion time from the position where the top of the cone entered the flow until the nose was at the nozzle centerline was typically 1.5 sec. The model pitch system provides a range of angle of attack to 20°. More detailed information about the tunnel can be found in reference 9. A single-pass on-axis schlieren system with 2-ft-diameter mirrors, a horizontal knife edge, a 5-μsec-duration xenon-arc lamp, and a 70-mm camera, which operated up to 20 frames/sec, was used for obtaining either schlierens or shadowgraphs.

Test Conditions and Procedures

The model with the four nose configurations was tested for a total of 23 tests; the tunnel and coolant flow conditions are as summarized in table III. The tangent-slot model was tested only at an angle of attack of 0° because of a time constraint on the test schedule. The total temperature T_t was measured in the combustor. Free-stream unit Reynolds number and Mach numbers were calculated with measured pressures and temperatures from free-stream surveys; a typical survey is reported in reference 9 and the thermal, transport, and flow properties of methane-air combustion products are reported in reference 10. The stagnation-point heating rates were not measured but were calculated for a 1-in-radius hemispherical nose by the method of Fay and Riddell (ref. 11) using the properties in reference 10. (Stagnation-point heating rates for the 3-in-radius noses can be calculated by dividing by $\sqrt{3}$ because the stagnation-point heating rate is inversely proportional to the square root of the radius.) Various nitrogen coolant parameters are also tabulated.

The test procedure consisted of first manually setting steady nitrogen flow rates in the cooling system—the nitrogen flow was turned on for up to 2 min prior to model insertion, then tunnel test conditions were established, and next the model was pitched to the desired angle of attack and inserted into the test stream. The three shock-layer flow survey rakes were usually extended from the model after the flow was established about the model. However, for tests 98-9, 98-17, and 98-47, the rakes were fixed in the out position prior to model insertion; heating rates and model surface pressure results are not presented for these tests because of downstream interference effects behind the rakes.

Data Reduction and Uncertainties

Pressure data were obtained with strain-gage transducers having a combined nonlinearity and hysteresis error of approximately 1/4 percent of full scale. The gage ranges for the cone frustum were 10 psi; rake static-pressure gages, 5 psi, and the rake pitot pressure gages, 50 psi. Pressure gage error bands were ±0.025 psi, ±0.013 psi, and ±0.125 psi for the cone frustum, rake static pressure, and rake pitot pressure, respectively. Thermocouples for measuring model temperature were premium-grade Chromel-Alumel thermocouple wire which is accurate to ±2.0°R; the thermocouple reference temperature junction was also accurate to ±2.0°R.

Heating rates were calculated from the temperature-time slope by using the one-dimensional transient heat balance equation:

$$\dot{q} = (\rho c_p \tau)_w \frac{dT_w}{dt} \tag{3}$$

The temperature-time slope dT_w/dt was calculated every 1/20 sec with time steps dt of 1.0 sec by using a central difference method. This method produced scatter in the curves for dT_w/dt versus time because of the electronic noise and the digital method of recording temperature. At a time after the model was fully into the stream and the model pressures had stabilized, the computer-calculated values of dT_w/dt were time averaged over a period of 1 sec to reduce the scatter. (More sophisticated difference methods such as higher order central difference approximations and differentiation of second- and third-order curve fits of the temperature time histories were investigated but did not result in appreciable differences from the time-averaged dT_w/dt values.) The wall temperature T_w of the model was generally not at ambient temperature (540°R) by the time the model reached the flow centerline and the model pressures had stabilized. The maximum T_w reached before equation (3) could be applied was 840°R (on the windward side at an angle of attack of 10° without coolant).

The calculated values of the heat-transfer rate, both with and without coolant, were not extrapolated to the initial isothermal wall temperature of 540°R, based on the assumption of a constant heat-transfer coefficient, as was done in reference 6, because of the uncertainty of the heat-transfer coefficient and adiabatic wall temperature T_{aw} with coolant ejection. Calculation of the adiabatic wall temperature is discussed in more detail in the section "Analysis of Gas-Jet Heat Flux."

Uncertainty in the calculation of the heat-transfer rate from equation (3) depends directly on the uncertainty in the wall properties (ρ, c_p, and τ) and dT_w/dt. In addition, possible data reduction errors and conduction, convection, and radiation losses contribute to the uncertainty. The physical properties for the ogive frustum and the cone frustum skins are given in table IV. For the purpose of banding the uncertainty in calculated heat-transfer rates, the following possible percentage errors have been estimated: (1) ρ, ±2 percent; (2) c_p, ±2 percent; (3) τ, ±3 percent; (4) dT_w/dt, ±3 percent; (5) electronic instrumentation, ±1 percent; (6) conduction loss in skin, −1 percent; (7) effective thickness of the curved skin, +2.5 percent; and (8) maximum conduction loss in thermocouple and error due to added mass of thermocouple junction, −7 percent (calculated according to the methods described in ref. 12). Convection and radiation losses are considered negligible. These errors give a most probable (root-mean-square) overall error in measured heat-transfer rate of ±3.0 percent. No corrections for these errors were made.

Shock shapes were obtained from prints of shadowgraphs or schlierens. Because a collimated light beam was used in the test section, no relative displacement errors in shock standoff distance occurred between schlierens and shadowgraphs. Shock-layer Mach numbers were calculated from measured static and pitot pressure measurements by the Rayleigh pitot formula using $\gamma = 1.4$. Possible sources of error for static pressures after model insertion were investigated and are discussed in reference 6. According to that investigation, the net error is about +2 percent in Mach number; no corrections were made in the Mach number data. The Mach number data were also not corrected for possible flow misalignment when the model was tested at an angle of attack of 2.5°. Static pressure probe measurements are accurate to 1 percent for local probe misalignment up to 5°, with pitot probes less sensitive according to reference 13.

Discussion of Results

The results in the present paper consist primarily of model pressures and heating rates. However, shock shapes and shock-layer data were also measured in order to characterize the flow field around the model, and these data are presented first. The shock-layer rake data are listed in table V. Baseline pressure and heating-rate data are given in an overview format to characterize data trends without coolant. Then the model pressure and heating-rate data are presented for the gas-jet and the tangent-slot noses; these data are not compared with prediction but are compared with the baseline data. Not all model pressure and heating data are discussed in this report; however, all model data are tabulated—the pressure data in table VI and the heat-transfer data in table VII. The temperature data at each location at the time the heating rate was calculated are also given in table VII.

Shock Flow Field

Baseline shock shape. Schlierens or shadowgraphs of the shock shape over the two baseline (R-3 and R-1) nose configurations are shown in figure 11 for $\alpha = 0°$. Scale factors on the figures were obtained from known dimensions of the noses. As seen in figure 11(a), weak shocks originating at the surface joints are present. The recompression shock coming off the 0.023-in. backward-facing step at the ogive-cone joint can be seen in figure 11(b). As discussed in reference 6, pressure measurements were in good agreement with predictions; thus, this indicates little effect of the weak shocks. Real gas effects were important in calculating shock profiles for the R-3 and R-1 noses. Also, as noted in reference 6, predicted shock-standoff distances calculated from the codes described in references 14 and 15 using $\gamma = 1.4$ were 26 percent greater than the measurements at the stagnation point; agreement improved to 5 percent farther downstream. However, approximating real gas effects by using an effective $\gamma = 1.275$ obtained from correct normal-shock density ratios resulted in shock-standoff agreement at the stagnation point to within 4 percent and excellent agreement farther downstream.

Gas-jet shock shape. The gas-jet and mainstream shocks are shown in figures 12(a) through 12(j) for angles of attack up to 10°. The shock shapes at $\alpha = 0°$ are similar to those presented in references 5, 16, and 17 and demonstrate the typical characteristics of mainstream bow shock, jet-mainstream stagnation point, jet-mainstream mixing region, jet normal shock, separation pocket, and secondary shocks as indicated in figure 12(a). Comparison of the present experimental shadowgraphs for $\dot{m} = 0$ and 2.0 lbm/sec (fig. 12(d)) with predictions by using Navier-Stokes laminar mixing models is made in reference 7 where the overall characteristics of the gas-jet and mainstream shocks in the nose region are in reasonable agreement with the present data. As can be seen from the present shadowgraphs, the shock-standoff distance increased with increasing coolant flow rate. The region of reattachment, at the end of the separated pocket, as indicated by the start of the reattachment shocks can be seen to move rearward, at $\alpha = 0°$, with increasing $\dot{m}$ and forward on the windward side with increasing angle of attack.

Inspection of the 70-mm frame sequences (taken at 20 frames/sec with 5-μsec exposure times) indicated that for all coolant flow rates and angles of attack, the mainstream bow shock structures in the stagnation region were basically steady. However, downstream of the stagnation region, the mainstream bow shock had some irregularities and some unsteadiness (small time fluctuations). The extent of the shock movement is small as shown in figure 12(h) where more than one shock position has been captured during the 5-μsec exposure.

Tangent-slot shock shape. Shadowgraphs of the tangent-slot nose for two coolant flow rates at $\alpha = 0°$ are shown in figures 12(k) and 12(l). The pressures ($p_c = p_e$) at the slot exit plane were matched for the lowest coolant flow rate of $\dot{m} = 0.3$ lbm/sec. The edge pressure ratio, $p_e/p_s = 0.076$, was obtained by interpolating measured pressures from nose R-3 and the cone frustum pressures as reported in reference 6. At matched pressures, there is a minimum of shock disturbances as predicted in reference 2; a weak recompression shock can be seen resulting from the edge stream and coolant expanding downstream of the (finite) 0.040-in-thick slot lip. At a higher coolant flow rate (fig. 12(k)), the underexpanded slot flow results in complex shock patterns downstream of the slot. As noted in reference 2, analysis of the coolant-boundary-layer mixing process is difficult for slot exit pressures greater than static pressures because of the resulting system of shocks as seen in figure 12(l). The present tangent-slot nose is not an optimum design in the sense that the slot lip thickness is not small compared with the slot height—the lip is 16 percent of the slot height. (Structural considerations dictated the lip thickness.) An additional consideration is the large slot height compared with the laminar boundary-layer thickness; that is, the coolant is not injected into the boundary layer, but rather the coolant ejection is a major disturbance to the laminar boundary layer. The boundary layer upstream of the tangent slot is laminar, based on heating rates, as noted in reference 6.

Gas-jet shock-layer surveys. Shock-layer flow-field survey results are presented in figures 13 through 16 for the gas-jet nose. The data are also given in table V. (The rakes were inserted from the model into the shock layer by a pneumatic system and sometimes the rakes failed to operate; thus, not all the runs have rake data nor were data from all three rakes always obtained for a particular run.) The shock-layer data with coolant are compared with baseline (no coolant) data. Data are plotted as a function of the approximately normal distance from the cone surface. (See description of rake assemblies for normal distance errors.) The average of the two floor plate pressure readings are plotted at zero normal distance. For the present tests, both with and without coolant, the measured Mach numbers were obtained from the Rayleigh pitot formulation using $\gamma = 1.4$. Discussion of the accuracy of the baseline shock-layer Mach number and total temperature data are given in reference 6.

As indicated in figure 13, for the high coolant flow rate, the static pressures are significantly reduced compared with the profiles from both baseline R-1 and R-3 noses, at least up to $s_a/L = 0.68$ (the third rake at $s_a/L = 0.92$ did not operate). The pitot pressures were more affected than the static pressures when compared with the baseline data. At $\dot{m} = 1.2$ lbm/sec, the pitot-pressure profiles for all three rake locations were very close to the profiles with the baseline R-3 nose but significantly reduced compared with the profiles with the R-1 nose; however, at $\dot{m} = 4.6$ lbm/sec, the pitot-pressure profiles were significantly reduced. The Mach number profile trends with coolant generally follow the pitot pressure trends and show a low Mach number region far downstream from the stagnation region for large coolant flow rates. The reduction in shock-layer pressure and Mach numbers with gas-jet coolant ejection appears to be due to the increased effective bluntness of the body as manifested by the increased shock radius and standoff with coolant. This increased effective bluntness is discussed later. Love (ref. 18) investigated the flow field about an ellipse with a forward-facing gas jet at a free-stream Mach number of 1.62. Pitot-tube surveys in the boundary-layer and surface pressure distributions were obtained. Love found that, for a laminar boundary layer without blowing, the gas jet promoted transition to turbulent flow and the Mach number distribution in the boundary layer was reduced.

The total-temperature profiles, compared with the baseline data for R-3 and R-1 noses, appear to be reduced, due to coolant, only for the forward rake position for $\dot{m} = 1.2$ lbm/sec; however for the maximum flow rates, the total temperatures were significantly reduced for $\alpha = 0°$, at least up to the second rake location ($s_a/L = 0.68$). Reduction in shock-layer temperatures reflect the downstream cooling effectiveness of the ejected gas.

At $\alpha = 2.5°$, rake data with coolant are not compared with baseline data (no cooling) because none exist. As seen in figure 14 at $s_a/L = 0.68$, the maximum coolant flow rate for the present tests caused a significant reduction in shock-layer profiles compared with the low coolant flow rate. For the high flow rates, the shock-layer profiles are the same for $\alpha = 0°$ and $2.5°$; this indicates that the high flow rate masked the effect of small angle of attack.

Gas-jet effective nose radius correlation. The purpose of this section is to examine how the gas-jet Mach number and total-temperature shock-layer profiles correlate with the effective nose radius due to coolant ejection. The effective radius is taken as the radius of the interface between the gas jet and the mainstream shock layer in figure 12(a). If an increase in effective nose radius is the cause of the reduced Mach numbers, then the Mach number data plotted against η normalized by the effective nose radius r_n should show similar profiles at given normalized distances x/r_n from the stagnation point. Normalizing the coordinates, η and x, by r_n is suggested by the work of Cleary (ref. 19).

For the two gas-jet tests 98-29 and 98-47 ($\dot{m} = 4.6$ and 1.2 lbm/sec at $\alpha = 0°$), the effective nose radii r_n of 4.1 and 2.3 in., respectively, were obtained from the shadowgraphs. (Shadowgraph data were not taken for test 98-47; therefore, the image obtained from test 98-33 (fig. 12(c)) was used.) Two independent measurements can be made to determine the effective nose radius since both the shock radius of curvature and the shock-standoff distance at the centerline are uniquely defined by the flow conditions and body shape according to reference 20. The procedure used to obtain the effective nose radius r_n was (1) from the baseline R-3 nose data, calculate ratios of shock-standoff distance to nose radius and shock centerline radius of curvature to nose radius and (2) from these ratios and the gas-jet shock-standoff distances and centerline shock radius of curvature, calculate two values of the effective nose radius. (The shock's centerline radius of curvature was calculated from a best hyperbola fit of the measured shock shape.) For test 98-29, the calculated effective nose radii using these two ratios agreed to within 6 percent. But agreement was only within 18 percent for test 98-33 because of the somewhat irregular apparent nose shape. (See fig. 12(c).) Values used are from the shock centerline radius-of-curvature measurements.

Baseline and gas-jet shock-layer Mach numbers are plotted in figure 15 against η/r_n. (The three rake locations can be distinguished, if desired, by the different tick positions.) Generally, for a given η/r_n, the Mach number would be expected to increase as x/r_n increases. Baseline data, as seen in figure 15(a), correlate into two bands. One band, $x/r_n = 14.76$ to 68.21, clearly indicates a continuous trend in Mach number for both the R-1 and R-3 noses as η/r_n decreases. (This trend is not evident with the data plotted against only η in fig. 13.) The decrease in baseline Mach number for η/r_n less than 0.6, as seen in figure 15(a) is due to the entropy layer caused by the effective nose bluntness and is not an indication of the boundary-layer thickness. Based on boundary-layer-thickness calculations done in reference 6, the turbulent-boundary-layer thickness is only $\eta/r_n = 0.16$. The two data points at

$\eta/r_n = 0.58$ that are greater than Mach number 6.0 (and exceed the sharp cone Mach number of 5.2 for $\gamma = 1.4$) are also associated with the bluntness-induced entropy layer as discussed by Cleary (ref. 19). The second distinct group at $x/r_n = 7.12$ has approximately the same slope but is lower than the first group; thus, a more rapid drop off in Mach number is indicated as x/r_n decreases.

Gas-jet Mach number data are given in figure 15(b). Again the data fall into two bands according to x/r_n, except at low η/r_n. Data for the two coolant flow rates of 4.6 and 1.2 lbm/sec group together; thus, the validity of using the effective nose radius is indicated. Convergence of the data at η/r_n less than about 0.1 indicates that near the surface the Mach number reduction is independent of downstream location.

Comparison of the baseline Mach number data and the gas-jet data is more easily made in figure 15(c) where for clarity, the data symbols are omitted. Here it is easily seen that the data at the higher x/r_n range for the gas jet nearly overlap the baseline data, whereas for the low x/r_n ranges, the baseline and gas-jet data are very distinct. Overall, it appears that the effective nose radius does correlate the Mach number data for both gas jet and baseline beyond $x/r_n = 14$ but not for lower x/r_n. The reason appears to be that in the stagnation region for the gas jet, the ejection process gives an effective body shape that is more complicated than can be described by an effective nose radius of a simple blunt conical body; farther downstream, as the coolant mixes with the conical test gas flow, the shock-layer flow field probably approaches the kind of flow that can be described by a blunt cone.

Total-temperature profiles are plotted against η/r_n in figure 16. The baseline (uncooled) data are shown in figure 16(a) and, within the scatter of measurements, group into one band. The decrease in temperature starting at $\eta/r_n = 0.6$ to 0.8 is an indication of the location at which the total temperature decreases toward the surface because of viscous effects in the shock layer. The decrease in temperature is not an indication of the boundary-layer thickness because as noted, the estimated boundary-layer thickness, based on velocity ratio, is $\eta/r_n = 0.16$.

For the gas jet, temperature data with coolant are plotted in figure 16(b). The close agreement of the data in the middle band ($x/r_n = 11.78$ to 12.69) for the wide range of flow rates (1.2 to 4.6 lbm/sec) indicates that at a given x/r_n the temperature variation in the shock layer is independent of coolant flow rates.

Comparison of baseline and gas-jet coolant data is made in figure 16(c). Convergence of gas-jet and baseline data at about $x/r_n = 0.7$ indicates similarity of the η/r_n extent of temperature gradients in the shock layer.

The relative success of correlating the gas-jet Mach number and temperature data with the effective nose radius has been shown. Because of variable entropy associated with nose bluntness and the apparently fully viscous shock layer, Mach numbers and temperatures vary continuously through the shock layer near the wall and thus do not indicate a conventional boundary-layer edge.

Tangent-slot shock-layer surveys. Tangent-slot nose data are presented in figure 17 for three coolant flow rates, $\dot{m} = 0.3$, 1.2, and 2.3 lbm/sec. Static-pressure shock-layer profiles showed a small reduction compared with the R-3 nose baseline profiles. For all rake locations the pitot pressure, compared with the baseline profiles, decreased with increasing coolant flow rate. Mach number profiles followed the same reduction trends with increasing coolant flow rate as did the pitot pressures. Total temperatures were reduced mostly near the model's surface with significant reduction shown at $s_a/L = 0.40$ for $\dot{m} = 2.3$ lbm/sec. (See fig. 17(c).)

Comparisons of gas-jet and tangent-slot coolant ejection effects on shock-layer profiles can be made at $\alpha = 0°$ and the same coolant flow rate of 1.2 lbm/sec by comparing the cooling data in figures 13 and 17(b) and using the R-3 data as a reference. The pitot pressure, Mach number, and total temperature were lower for tangent-slot ejection than for gas-jet ejection.

Pressure and Heating-Rate Distributions

Baseline. Normalized longitudinal pressure and heating distributions from the baseline (no coolant) results are presented in figures 18 and 19 for noses R-1 and R-3, respectively. The baseline values are used to compare the coolant data in the following sections. The heating rates were normalized by the calculated stagnation-point heating rate, for a 1-in-radius hemispherical nose, obtained by the method of Fay and Riddell (ref. 11). The surface pressures and local heating rates are given in tables VI and VII, respectively. Circumferential distributions are not plotted but were presented in reference 6. No predictions are given in the present report, but the baseline data were compared with predictions in reference 6. Pressure measurements were compared with the predictions from a code described in reference 14. On the windward ray, agreement was good for both noses up to $\alpha = 10°$; however, on the leeward ray, the code overpredicted the pressures immediately downstream of the nose and predicted the measured pressures near the rear of the cone to within experimental accuracy. In reference 6, laminar heating rates were compared with the theory of Hamilton (ref. 21), and the agreement was good. Turbulent heating was compared with the semiempirical method described in references 22 and 23, but this method underpredicted the fully turbulent heating by about 15 percent. Based on the measured heating rates for both baseline noses, the flow is laminar over the front portion of the model—up to about $s_a/L = 0.30$ and 0.70 for the R-1 and R-3 nose configurations, respectively. Fully turbulent flow was reached on the R-1 nose configuration at about $s_a/L = 0.80$.

Gas jet. Model surface pressures on the windward ray are presented in figure 20 and are compared with the baseline R-1 and R-3 distributions (only the R-1 distribution at $\alpha = 2.5°$). Repeatability of the data with coolant is indicated by the data symbols with and without ticks at $\dot{m} = 4.6$ lbm/sec and $\alpha = 0°$ (fig. 20(a)). At $\alpha = 0°$, the model pressure distributions for the lower coolant flow rates closely follow the R-3 nose baseline distribution. Overall, it appears that the pressure distribution is substantially reduced by high coolant flow rates, with the longitudinal extent of reduction increasing with $\dot{m}$ and decreasing with angle of attack. The magnitude of the reduction in pressure increases with both angle of attack and coolant flow rate over the forward portion of the model. This reduction in pressure with increasing coolant flow rate is probably related to the increase in effective nose bluntness. Within the scatter of the pressure data, the coolant ejection did not have any affect on base (boattail) pressures.

Windward ($\phi = 0°$) and leeward ($\phi = 180°$) model heating rates are presented in figures 21, 22, and 23. Compared with the baseline R-1 heating rates, the gas jet significantly reduced the heating rates over the ogive nose for all $\dot{m}$ and angles of attack on both the $\phi = 0°$ and 180° rays. The heating rates near the front of the ogive were significantly reduced for all coolant flow rates even to the point of going negative for the higher flow rates because of the low coolant exit temperature. Downstream of the ogive nose for $\dot{m} = 0.8$ lbm/sec, the gas jet appears to have tripped the boundary layer causing higher heating rates than with the R-1 nose for $\alpha = 0°$ and 2.5°; the tripping of the boundary layer is manifested by the heating profile slopes paralleling the transitional R-1 data. At maximum flow rates, the heating was reduced down the entire length of the model for up to $\alpha = 2.5°$ and up to $s_a/L = 0.40$ for $\alpha = 10°$. At $\alpha = 0°$, downstream of the ogive nose, the heating distributions with the lower coolant flow rate match those with the R-1 nose, whereas with the higher flow rate, the distributions match those with the R-3 nose. A similar trend in distribution matchup occurs on the leeward side. As with the pressure distributions, these comparisons suggest that there is a correlation between the model surface heat-transfer rate far downstream from the point of coolant injection, and the apparent bluntness of the gas-jet model due to the interface of the gas-jet and the flow-field shocks.

To better see the details of the heating distribution over the ogive and the cone frustum just downstream of the ogive, an enlargement of part of figures 21 through 23 is presented in figure 24 but without the baseline data. Good continuity of heating profile slopes between the ogive and the cone is an indication of the validity of the constants used to calculate the heating rates. At angle of attack, the effectiveness of the coolant in reducing the heating rate is a stronger function of the coolant flow rate for the windward ray than the leeward ray.

Figures 25, 26, and 27 give the circumferential model pressure distributions for $s_a/L = 0.33$ and 0.92 for various coolant flow rates and angles of attack. Generally, the effect of the gas-jet ejection was to decrease the windward-side surface pressures more than the leeward-side surface pressures with the amount of reduction increasing with flow rate. Figures 28 through 32 give the circumferential heating distributions for various s_a/L, $\dot{m}$, and angles of attack. Figure 28 shows that at $\alpha = 0$, the heating distributions are symmetrical indicating symmetrical coolant ejection and spreading, which was also indicated by the pressure distributions. At moderate angles of attack, high coolant flow rates are effective in reducing the heating on both the windward and leeward sides for the entire model. As discussed in reference 6, disturbances caused by the roughness of the rakes cover plate and frame (fig. 6(a)) promoted transition even when retracted; thus, downstream data were affected. Shown in figures 29 through 32 are the circumferential regions of the model (noted by the arrows) that are in the wake of the rakes. It is apparent that the retracted rakes affected the baseline data more than the coolant data; see, for example, the jump in baseline data in figure 29(a) at $\phi = -45°$.

Tangent slot. The tangent-slot model was only tested at $\alpha = 0°$ because of a restricted test schedule. The data from the tangent-slot model are compared with those from the baseline R-3 nose. Longitudinal data are given in figure 33. Increased coolant flow rate caused a reduction in model surface pressure far downstream of the slot, even though the pressure in the near-downstream region of the slot did not indicate any significant alteration. The ejection of the coolant from the slot caused transition; this can be seen in figure 33(b) for the coolant flow rate, $\dot{m} = 0.3$ lbm/sec, at which the pressures were matched at the slot exit. However increased flow rates caused a substantial reduction in heating in the near region downstream of the slot but adversely increased the heating levels farther downstream. For $\dot{m}$ greater than 1.2 lbm/sec, the heat flux was not reduced any more in the near region downstream of the slot since the heat flux was already nearly zero.

Circumferential pressure and heating distributions are given in figures 34 and 35, respectively. Pressure distributions, both with and without coolant ejection, indicate greater uniformity at $s_a/L = 0.33$ than at $s_a/L = 0.92$. Good heating agreement for the $\phi = 0^\circ$ and 180° rays in the near-region downstream of the slot shows that the coolant ejection was symmetrical; but farther downstream the agreement decreases because of the unevenness of transition. As noted earlier and discussed in reference 6, the baseline heating rate data for the R-3 model were affected by the presence of the retracted rakes; the wake regions of the retracted rakes are indicated in figure 35 by the solid arrows, but the coolant data appear to be less affected by the retracted rake disturbances. Even as far downstream as $s_a/L = 0.92$, significant coolant is present at $\dot{m} = 2.3$ lbm/sec as indicated by the total temperature profiles in figure 17(c).

Analysis of Gas-Jet Heat Flux

Alternation of the heat flux with gas-jet coolant ejection was due to more than just the cooling effect of the gas on the flow field because coolant ejection affected the model pressure and shock-layer Mach number distributions. Shock-layer rake survey data have not been previously obtained in other gas-jet investigations. (Love, ref. 18, did make Mach number boundary-layer surveys over an ellipse with upstream ejection but at ambient temperature in low supersonic flow.) The purpose of this section is to utilize these shock-layer pressure, Mach number, and total-temperature data in existing semiempirical, engineering equations to examine the gas-jet heat-flux data and gain insight into the mechanisms that drive the heat flux.

Equations. The following semiempirical, engineering equation for turbulent heating is described in references 22 and 23 and also derived in reference 24:

$$\mathrm{St}^\star = 0.035\mathrm{Pr}^{\star -2/3}\,(\mathrm{Re}^\star s)^{-1/5} \tag{4}$$

The upper range of $\mathrm{Re}^\star s$ is 10^7. (The equation for laminar heating is similar except that the coefficient is 0.575 and the exponent for $(\mathrm{Re}^\star s)$ is 1/2.) Equation (4) was developed for nonfilm cooling geometries and it is assumed valid for the gas-jet model far downstream from the point of ejection. Since St is defined as $h/\rho^\star V_e c_p^\star$ and $\dot{q}$ can be written as

$$\dot{q} = (T_{aw} - T_w)\,h \tag{5}$$

then the equation can be rewritten as follows where the terms in brackets ([ ]) make up the convective heat-transfer coefficient, h:

$$\dot{q} = (T_{aw} - T_w)\left[0.031c_p^\star(p_e M_e)T_e^{1/2} \times \frac{1}{T_e^\star}\mathrm{Pr}^{\star -2/3}\,(\mathrm{Re}^\star s)^{-1/5}\right] \tag{6}$$

The equation for laminar heating is similar except that the coefficient is 0.516 and the exponent for $\mathrm{Re}^\star s$ is $-1/2$. For the gas jet, s is measured from the centerline end of the ogive. The properties indicated by the superscript $\star$ are evaluated at the reference temperature $T^\star$ defined by the following equation (see ref. 23):

$$T^\star = T_e + 0.50(T_w - T_e) + 0.22(T_{aw} - T_e) \tag{7}$$

The following two perfect gas relations were used:

$$T_e = \frac{T_o}{1 + \frac{\gamma - 1}{2}\,M_e^2} \tag{8}$$

$$\rho^\star V_e = p_e M_e\,\frac{1}{T_e^\star}\left(\frac{\gamma}{R}\right)^{1/2} T_e^{1/2} \tag{9}$$

Thermodynamic properties ($\mathrm{Pr}^\star$, $c_p^\star$, $\mu^\star$, $\gamma = 1.38$, and $R = 55.03$) at an equivalence ratio of 0.7 for methane-air combustion products from reference 10 were used. The quantities T_{aw}, T_w, T_e, and $p_e M_e$ are obtained from the measured rake data and the wall temperature. The recovery temperature T_{aw} was calculated by the following expression:

$$T_{aw} = \mathrm{Pr}^{\star 1/3}\,(T_o - T_e) + T_e \tag{10}$$

where T_o is the measured total temperature from the shock-layer rake data. The exponent for $\mathrm{Pr}^\star$ is 1/3 for turbulent flow as shown and 1/2 for laminar flow. Equation (10) is an established method for boundary layers without mass injection and should be valid for the gas-jet model far downstream from the point of ejection. Gas-jet data with the highest coolant flow rate of 4.6 lbm/sec from test 98-29 were examined. Experimental rake data at $s_a/L = 0.40$ and 0.68 were available. The R-1 baseline nose configuration was used for turbulent heating comparison and the

R-3 nose for laminar comparison. Nose R-1 rake and heat-flux data were obtained from test 98-17 in which the rakes were fixed out; heat-flux data on the $\phi = 0°$ ray were not affected by the fixed rakes.

Results. Whether the gas-jet boundary layer is laminar, transitional, or turbulent is discussed before the heat-flux data are analyzed. Figure 36 gives the R-1 and R-3 baseline and the gas-jet longitudinal heat-flux data (presented as faired curves for clarity). Heat-flux calculations were made by using the shock-layer data from the first probe at $\eta = 0.20$ in. from the wall. For the R-1 data, turbulent calculations are in good agreement with the turbulent portion of the data. For the R-3 data, laminar calculations are in good agreement with the laminar portion of the data. For the gas-jet data, laminar calculations underpredict the data; this indicates that the gas-jet boundary layer is not laminar. The laminar predictions of Macaraeg (ref. 7) when compared with the present experimental gas-jet data also indicated that the gas-jet boundary layer is not laminar.

Since the gas-jet boundary layer is not laminar, the turbulent equation is used to obtain the heat-flux components. Rather than arbitrarily select the shock-layer values at the first probe, equation (6) is evaluated at each η/r_n location in the shock layer, with the corresponding local shock-layer values used as boundary-layer edge conditions, until agreement with the measured wall heat flux is obtained. Components of the baseline and gas-jet heat fluxes are then compared. Figure 37 shows the calculated gas-jet heating rates versus η/r_n and the measured gas-jet wall heat flux. At $x/r_n = 7.1$, and 12.6, the turbulent calculations agree with the measurements using shock-layer properties close to the wall at $\eta/r_n = 0.07$ and 0.12, respectively. For comparison, for the baseline R-1 nose at $x/r_n = 48.5$ and 67.9, the turbulent calculations agree with the measurements at $\eta/r_n = 0.2$ and 0.4, respectively.

Additional evidence that the gas-jet boundary layer is not laminar can be seen as follows. At $x/r_n = 7.1$ (fig. 37(a)) laminar calculations agree with the measured heat flux at $\eta/r_n = 0.4$ but which is too far from the wall to be reasonable because this suggests a laminar boundary-layer thickness greater than the turbulent thickness, $\eta/r_n = 0.12$, at $x/r_n = 12.6$. At $x/r_n = 12.6$ (fig. 37(b)), laminar calculations and measured heat flux clearly do not agree and would seem not to converge even using local conditions extrapolated beyond the present shock-layer measurements.

The change in components of the heat flux due to coolant ejection can now be deduced as follows. From equation (6), the turbulent heat-transfer coefficient can be written as follows:

$$h = \left(0.064 s^{-1/5}\right) (p_e M_e)^{4/5}\ f(T) \qquad (11)$$

where $f(T)$ represents the temperature-dependent transport terms in the heat-transfer coefficient and is given as

$$f(T) = c_p^{\star} \mu^{\star 1/5} \mathrm{Pr}^{\star -2/3}\ T_e^{2/5} T^{\star -4/5} \qquad (12)$$

The heat-transfer coefficient h is expressed in terms of $p_e M_e$ because these are the local quantities that are measured. The gas properties in the shock layer are only temperature dependent and not pressure dependent for the range of temperatures involved in the present calculations. Individual turbulent heat-transfer terms in equation (6) for both the gas-jet and R-1 baseline configurations are given in table VIII.

Percentage changes in h and $\dot{q}$ components, compared with baseline R-1 values, are illustrated in figure 38. (Because the individual terms are multiplied, the percentage changes in the bar figures do not add to 100 percent.) At $s_a/L = 0.40$, the 93-percent reduction in heat flux is due primarily to the 84-percent reduction in temperature driving potential $T_{aw} - T_w$; however, an additional reduction is obtained through a 57-percent reduction in the heat-transfer coefficient. Farther downstream, at $s_a/L = 0.68$, the heat flux is reduced 76 percent due to a 55-percent reduction in driving potential and a 47-percent reduction in the convective heat-transfer coefficient. Clearly, the coolant effect on the temperature driving potential dissipates because of mixing. The reduction in convective heat-transfer coefficient is due to a reduction in the pressure–Mach number term which results from the increase in the apparent bluntness of the gas-jet nose. However, the temperature-dependent transport terms $f(T)$ actually increase. Based on the small change in the pressure–Mach number term from $s_a/L = 0.40$ to 0.68, the result of the increased effective nose bluntness is felt far downstream from the point of coolant ejection.

The alteration of the temperature-dependent transport terms in the heat-transfer coefficient h indicates the importance of knowing the mixture gas properties accurately in the shock layer. For the present calculations, the gas properties for the products of combustion (ref. 10) were used; for the actual gas-jet case of a mixture of nitrogen and combustion products in the shock layer, there could be some error in not knowing the actual gas composition. Some preliminary measurements of surface gas sampling that were done near the front of the model during the present tests were reported in reference 25 and indicate that gas sample measurements in the shock layer would be a difficult task.

Concluding Remarks

Two film-cooling nose shapes on a 12.5° half-angle cone model having a 3-ft-base diameter were tested in the Mach number 6.7 stream of the NASA Langley 8-Foot High-Temperature Tunnel. The nominal test stream total temperature was 3300°R and the nominal free-stream unit Reynolds number per foot was 1.4×10^6. One nose shape, the gas jet, was an ogive frustum with a forward-facing 0.8-in-radius orifice; this configuration was tested with gaseous nitrogen coolant at angles of attack up to 10°. The second nose shape, the tangent slot, was a 3-in-radius tip with a 0.243-in-high rearward-facing slot; this configuration was only tested at an angle of attack of 0°. Shock shapes, shock-layer profiles, surface-pressure distributions, and surface heating-rate distributions were measured and compared with measurements obtained from baseline (no coolant) 1-in- and 3-in-radius solid nose tips. Shock-layer profiles included static and pitot pressures and total temperatures. The results are summarized as follows.

Analysis of the local heat flux for gas-jet cooling using existing, semiempirical, engineering relationships and present shock-layer flow-field data showed that close to the region of coolant ejection the reduction in heat flux is due primarily to the reduction in temperature driving potential (recovery temperature minus wall temperature). Farther downstream, the reduction in heat flux is about equally due to reductions in driving potential and heat-transfer coefficient; the latter caused by a reduction in the shock-layer pressure–Mach number product.

Generally, gas-jet coolant ejection significantly reduced the heat flux, even at an angle of attack of 10° over the model just downstream of coolant ejection. However, coolant ejection caused earlier transition and for the lowest coolant flow rate resulted in higher heating rates over the transition region compared with baseline data.

For the gas jet, longitudinal surface pressures decreased with increasing coolant flow rate. Part of the reduction was caused by an increase in effective bluntness of the gas-jet nose.

Shock-layer profiles for the gas-jet nose showed that the static pressure, pitot pressure, Mach number, and temperature profiles were significantly reduced compared with the baseline data. Increased effective bluntness of the gas-jet nose with coolant ejection partly accounted for the reduced Mach numbers.

Shadowgraphs showed that, for the gas jet, the complex bow-shock and separation-reattachment regions were basically steady for all coolant flow rates and angles of attack.

Tangent-slot coolant ejection generally caused a reduction in heat flux to zero just downstream of the slot, and compared with baseline data, significantly reduced the heat-flux farther downstream from the slot exit. However, for the lowest flow rate, coolant ejection caused earlier transition resulting in increased heat flux.

Tangent-slot coolant ejection caused reduced surface pressures, compared with the baseline data, over the rear portion of the model.

Shock-layer profiles for the tangent-slot nose showed that coolant ejection caused reductions in pitot pressure, Mach number, and total temperature when compared with baseline data.

Shadowgraphs showed that, for the tangent slot, the complex shock expansion system just downstream of the slot was steady with time.

NASA Langley Research Center
Hampton, Virginia 23665-5225
March 9, 1988

References

1. Goldstein, Richard J.: Film Cooling. *Advances in Heat Transfer, Volume 7,* Thomas F. Irvine, Jr., and James P. Hartnett, eds., Academic Press, Inc., 1971, pp. 321–379.
2. Cary, A. M., Jr.; Bushnell, D. M.; and Hefner, J. N.: Predicted Effects of Tangential Slot Injection on Turbulent Boundary Layer Flow Over a Wide Speed Range. *J. Heat Transf.*, vol. 101, no. 4, Nov. 1979, pp. 699–704.
3. Eiswirth, E. A.; Kipp, H. W.; Brandon, H. J.; and Masek, R. V.: An Experimental Investigation of Ogive Film Cooling. 76-ENAs-39, American Soc. of Mechanical Engineers, July 1976.
4. Klich, George F.; and Leyhe, Edward W.: *Experimental Results of Cooling a 12.5° Semivertex Angle Cone by Ejection of Hydrogen and Helium From Its Apex at Mach 7.* NASA TN D-2478, 1964.
5. Schiff, Lewis B.: The Axisymmetric Jet Counterflow Problem. AIAA Paper 76-325, July 1976.
6. Nowak, Robert J.; Albertson, Cindy W.; and Hunt, L. Roane: *Aerothermal Tests of a 12.5° Cone at Mach 6.7 for Various Reynolds Numbers, Angles of Attack, and Nose Shapes.* NASA TP-2345, 1985.
7. Macaraeg, Michele G.: *Application of CFD to Aerothermal Heating Problems.* NASA TM-87670, 1986. (Available as AIAA-86-0232.)
8. *Flow Measurement. Part 5—Measurement of Quantity of Materials, Supplement to ASME Power Test Codes,* PTC 19.5; 4—1959, American Soc. of Mechanical Engineers, c.1959.

9. Deveikis, William D.; and Hunt, L. Roane: *Loading and Heating of a Large Flat Plate at Mach 7 in the Langley 8-Foot High-Temperature Structures Tunnel.* NASA TN D-7275, 1973.
10. Leyhe, E. W.; and Howell, R. R.: *Calculation Procedure for Thermodynamic, Transport, and Flow Properties of the Combustion Products of a Hydrocarbon Fuel Mixture Burned in Air With Results for Ethylene-Air and Methane-Air Mixtures.* NASA TN D-914, 1962.
11. Fay, J. A.; and Riddell, F. R.: Theory of Stagnation Point Heat Transfer in Dissociated Air. *J. Aeronaut. Sci.*, vol. 25, no. 2, Feb. 1958, pp. 73–85, 121.
12. Larson, M. B.; and Nelson, E.: Variables Affecting the Dynamic Response of Thermocouples Attached to Thin-Skinned Models. *Trans. ASME, Ser. C: J. Heat Transf.*, vol. 91, no. 1, Feb. 1969, pp. 166–168.
13. Liepmann, H. W.; and Roshko, A.: *Elements of Gasdynamics.* John Wiley & Sons, Inc., c.1957.
14. Marconi, Frank; and Yaeger, Larry: *Development of a Computer Code for Calculating the Steady Super/Hypersonic Inviscid Flow Around Real Configurations. Volume II—Code Description.* NASA CR-2676, 1976.
15. Moretti, Gino; and Bleich, Gary: Three-Dimensional Flow Around Blunt Bodies. *AIAA J.*, vol. 5, no. 9, Sept. 1967, pp. 1557–1562.
16. Romeo, David J.; and Sterrett, James R.: Flow Field for Sonic Jet Exhausting Counter to a Hypersonic Mainstream. *AIAA J.*, vol. 3, no. 3, Mar. 1965, pp. 544–546.
17. Donohoe, John C.; Blackstock, Thomas A.; and Keyes, J. Wayne: Experimental Verification of the Technique for Measurement of Ablation of the Gasjet Nose Tip. AIAA Paper 77-786, June 1977.
18. Love, Eugene S.: *The Effects of a Small Jet of Air Exhausting From the Nose of a Body of Revolution in Supersonic Flow.* NACA RM L52I19a, 1952.
19. Cleary, Joseph W.: *An Experimental and Theoretical Investigation of the Pressure Distribution and Flow Fields of Blunted Cones at Hypersonic Mach Numbers.* NASA TN D-2969, 1965.
20. Billig, Frederick S.: Shock-Wave Shapes Around Spherical- and Cylindrical-Nosed Bodies. *J. Spacecr.*, vol. 4, no. 6, June 1967, pp. 822–823.
21. Hamilton, H. Harris, II: *Calculation of Laminar Heating Rates on Three-Dimensional Configurations Using the Axisymmetric Analogue.* NASA TP-1698, 1980.
22. Johnson, H. A.; and Rubesin, M. W.: Aerodynamic Heating and Convective Heat Transfer—Summary of Literature Survey. *Trans. ASME*, vol. 71, no. 5, July 1949, pp. 447–456.
23. Kays, W. M.: *Convective Heat and Mass Transfer.* McGraw-Hill Book Co., Inc., c.1966.
24. White, Frank M.: *Viscous Fluid Flow.* McGraw-Hill, Inc., c.1974.
25. Wood, George M., Jr.; Lewis, Beverley W.; Upchurch, Billy T.; Nowak, Robert J.; Eide, Donald G.; and Paulin, Patricia A.: Developing Mass Spectrometric Techniques for Boundary Layer Measurement in Hypersonic High Enthalpy Test Facilities. *ICIASF '83 Record*, IEEE Publ. 83CH1954-7, IEEE, 1983, pp. 259–270.

Table I. Location of Thermocouples† on Model

Thermocouple locations at circumferential positions ϕ of—																	s_a/L
−180.0°	−157.5°	−135.0°	−112.5°	−90.0°	−67.5°	−45.0°	−22.5°	0°	22.5°	45.0°	67.5°	90.0°	112.5°	135.0°	157.5°	180.0°	
Ogive nose frustum																	
T142				T134				T126								T142	0.112
T143				T135				T127								T143	0.124
T144				T136				T128								T144	0.138
T145				T137				T129								T145	0.140
T146				T138				T130								T146	0.161
T147				T139				T131								T147	0.173
T148				T140				T132								T148	0.186
T149				T141				T133								T149	0.199
12.5° cone frustum																	
																(‡)	0.219
T51																T51	0.229
T52								T1								T52	0.241
T53								T2								T53	0.266
T54								T3								T54	0.293
T55	T71	T76	T80	T84	T87	T92	T97	T4	T20	T25	T29	T33	T36	T41	T46	T55	0.317
T56								T5								T56	0.344
T57								T6								T57	0.374
T58								T7								T58	0.404
T59								T8								T59	0.434
T60								T9								T60	0.494
T61	T72	T77	T81	T85	T88	T93	T98	T10	T21	T26	T30	T34	T37	T42	T47	T61	0.534
T62								T11								T62	0.575
T63								T12								T63	0.649
T64	T73	T78	T82		T89	T94	T99	T13	T22	T27	T31		T38	T43	T48	T64	0.686
T65								T14								T65	0.708
T66								T15								T66	0.788
T67	T74	T79			T90	T95	T100	T16	T23	T28			T39	T44	T49	T67	0.818
T68								T17								T68	0.841
T69	T75		T83	T86	T91	T96	T101	T18	T24		T32	T35	T40	T45	T50	T69	0.907
T70								T19								T70	0.944

†Thermocouple numbers are designated by the notation "T_."
‡Start of cone frustum.

Table II. Location of Pressure Orifices[†] on Model

Orifice	ϕ, deg	s_a/L
P1	0	0.228
P2	0	0.253
P3	0	0.279
P4	0	0.303
P5	0	0.328
P6	0	0.358
P7	0	0.389
P8	0	0.417
P9	0	0.446
P10	0	0.512
P11	0	0.553
P12	0	0.594
P13	0	0.660
P14	0	0.731
P15	0	0.797
P16	0	0.852
P17	0	0.916
P18	0	0.967
P19	45	0.328
P20	90	0.328
P21	90	0.916
P22	135	0.328
P23	135	0.916
P24	180	0.328
P25	180	0.916
P26	−135	0.328
P27	−90	0.328
P28	−90	0.916
P29	−45	0.328
P30	−45	0.916

[†]Pressure-orifice numbers are designated by the notation "P_."

Table III. Test Matrix Summary

Test	Nose	Model test time, sec	α, deg	M	T_t (combustor), °R	Re × 10^{-6}, 1/ft	p_s, psia	$\dot{q}_s$ (calculated 1-in. radius), Btu/ft^2-sec	T_c, °R (†)	$\dot{m}$, lbm/sec	$\frac{p_c}{p_{tg}}$ (‡)	ρV (coolant exit), lbm/ft^2-sec	ρV^2 (coolant exit), lbm/ft-sec^2 (‡)	$\frac{(\rho V)_c}{(\rho V)_{tg}}$ (♯)	$\frac{(\rho V^2)_c}{(\rho V^2)_{tg}}$ (♯)
98-8	R-3	40	0.0	6.6	3260	1.45	17.80	129.2	*	*	*	*	*	*	*
98-9	R-3	4	0.0	6.8	3290	1.36	18.00	139.9	*	*	*	*	*	*	*
98-11	R-3	30	5.0	6.6	3230	1.46	18.00	128.2	*	*	*	*	*	*	*
98-12	R-3	15	10.0	6.6	3180	1.48	18.27	126.1	*	*	*	*	*	*	*
98-14	R-1	25	0.0	6.6	3250	1.45	17.92	129.2	*	*	*	*	*	*	*
98-15	R-1	25	2.5	6.7	3380	1.41	18.10	133.4	*	*	*	*	*	*	*
98-16	R-1	15	10.0	6.6	3180	1.47	18.16	126.1	*	*	*	*	*	*	*
98-17	R-1	4	0.0	6.4	3211	1.51	17.80	115.0	*	*	*	*	*	*	*
98-27	GAS JET	25	0.0	6.6	3213	1.44	18.11	130.6	496.0	4.6	5.58	329.5	333900	25.73	0.81
98-28	GAS JET	25	2.5	6.5	3133	1.50	17.98	120.5	485.0	4.4	5.12	315.1	315800	*	*
98-29	GAS JET	25	0.0	6.6	3206	1.48	18.07	125.4	487.0	4.6	5.05	329.5	330800	25.43	0.82
98-31	GAS JET	25	10.0	6.6	3277	1.47	18.09	126.8	492.0	3.8	4.34	272.2	274700	*	*
98-33	GAS JET	25	0.0	6.6	3310	1.44	18.10	131.3	487.0	1.2	1.55	85.9	86300	6.72	0.20
98-36	GAS JET	25	2.5	6.6	3241	1.45	18.11	129.2	491.0	1.2	1.50	85.9	86600	*	*
98-37	GAS JET	15	10.0	6.8	3470	1.33	17.84	142.4	505.0	1.2	1.46	85.9	87900	*	*
98-40	GAS JET	25	0.0	6.7	3318	1.40	17.97	134.4	495.0	2.0	2.46	143.2	145000	11.41	0.35
98-42	GAS JET	15	2.5	6.7	3357	1.41	17.99	132.3	517.0	0.8	1.11	57.3	59300	*	*
98-43	GAS JET	15	0.0	6.8	3319	1.34	17.82	139.9	515.0	0.8	1.18	57.3	59200	4.68	0.14
98-46	GAS JET	15	6.0	6.8	3320	1.34	17.80	140.3	521.0	1.2	1.47	85.9	89300	*	*
98-47	GAS JET	5	0.0	6.7	3220	1.43	18.10	131.6	523.0	1.2	1.44	85.9	89400	6.73	0.21
98-51	TAN SLOT	15	0.0	6.8	3411	1.32	17.74	142.0	514.0	1.2	3.26	31.9	45700	3.61	1.06
98-55	TAN SLOT	15	0.0	6.9	3643	1.18	17.14	150.3	521.0	0.3	0.99	7.4	9000	0.89	0.21
98-57	TAN SLOT	15	0.0	6.8	3440	1.32	17.74	142.4	487.0	2.3	6.79	57.7	68100	6.56	1.57

†Coolant temperature: for gas jet, temperature in manifold; for tan slot, temperature at exit plane.

‡c refers to coolant: for gas jet, static pressure in manifold; for tan slot, static pressure at exit plane.
tg refers to tunnel gas: for gas jet, stagnation pressure; for tan slot, edge pressure at exit plane.

♯c refers to coolant: for gas jet, orifice exit conditions; for tan slot, slot exit conditions.
tg refers to tunnel gas: for gas jet, normal bowshock conditions; for tan slot, edge conditions at exit plane.

*Not applicable.

Table IV. Physical Properties of Ogive-Frustum and 12.5° Cone-Frustum Skins

Physical property	Ogive frustum	12.5° cone frustum
Material	Stainless steel	René 41
Thickness, in.	0.083	0.060
Density, lbm/in^3	0.29	0.30
Specific heat, Btu/lbm-°R	0.12	0.11
Thermal conductivity at 640°R, $Btu\text{-}in/ft^2\text{-}hr\text{-}°R$	112.0	71.0

Table V. Shock-Layer Rake Data

		Rake 1, $s_a/L = 0.40$				Rake 2, $s_a/L = 0.68$				Rake 3, $s_a/L = 0.92$			
Test	η, in.	Static pressure, psia	Pitot pressure, psia	M	$\frac{T}{T_t}$	Static pressure, psia	Pitot pressure, psia	M	$\frac{T}{T_t}$	Static pressure, psia	Pitot pressure, psia	M	$\frac{T}{T_t}$
98-9	0.00	1.04	*	*	*	1.32	*	*	*	1.41	*	*	*
98-9	0.00	1.12	*	*	*	1.42	*	*	*	1.41	*	*	*
98-9	0.20	0.92	6.0	2.17	0.918	1.20	11.9	2.71	0.920	1.28	14.8	2.94	0.879
98-9	0.45	0.90	10.2	2.90	0.942	1.18	16.7	3.26	0.933	1.27	23.1	3.71	0.897
98-9	0.82	0.90	14.3	3.46	0.948	1.11	27.0	4.30	0.948	1.18	35.7	4.81	0.924
98-9	1.25	0.92	20.5	4.12	*	1.11	37.8	5.11	0.957	1.22	45.7	5.36	0.924
98-9	1.75	0.84	30.2	5.25	0.964	1.03	50.5	6.14	0.960	1.22	62.5	6.28	0.948
98-17	0.00	1.32	*	*	*	1.26	*	*	*	1.24	*	*	*
98-17	0.00	1.46	*	*	*	1.30	*	*	*	1.18	*	*	*
98-17	0.20	1.38	*	*	*	1.24	31.7	4.42	0.959	1.21	26.5	4.08	0.934
98-17	0.45	1.35	36.4	4.54	0.965	1.17	47.3	5.57	0.997	1.27	43.0	5.09	0.975
98-17	0.82	1.06	42.9	5.57	*	1.19	49.6	5.66	0.997	1.17	44.5	5.40	0.984
98-17	1.25	1.08	43.3	5.55	*	1.21	49.4	5.60	0.997	1.23	50.6	5.62	0.987
98-17	1.75	1.18	*	*	0.969	1.27	53.2	5.67	0.993	1.44	62.5	5.78	0.969
98-28	0.00	*	*	*	*	0.90	*	*	*	*	*	*	*
98-28	0.00	*	*	*	*	0.85	*	*	*	*	*	*	*
98-28	0.20	*	*	*	*	0.86	5.0	2.03	0.552	*	*	*	*
98-28	0.45	*	*	*	*	0.85	6.8	2.42	0.609	*	*	*	*
98-28	0.82	*	*	*	*	0.79	6.7	2.49	0.656	*	*	*	*
98-28	1.25	*	*	*	*	0.80	7.7	2.66	0.738	*	*	*	*
98-28	1.75	*	*	*	*	0.74	10.5	3.22	0.823	*	*	*	*
98-29	0.00	0.95	*	*	*	0.93	*	*	*	*	*	*	*
98-29	0.00	0.84	*	*	*	0.91	*	*	*	*	*	*	*
98-29	0.20	0.77	3.5	1.77	0.296	0.89	5.0	2.00	0.521	*	*	*	*
98-29	0.45	0.67	4.1	2.09	0.337	0.86	6.8	2.40	0.590	*	*	*	*
98-29	0.82	0.65	4.8	2.31	0.393	0.81	6.7	2.47	0.652	*	*	*	*
98-29	1.25	0.66	5.4	2.45	0.505	0.80	7.9	2.67	0.733	*	*	*	*
98-29	1.75	0.61	6.4	2.79	0.627	0.74	10.6	3.28	0.830	*	*	*	*
98-36	0.00	1.49	*	*	*	*	*	*	*	*	*	*	*
98-36	0.00	1.43	*	*	*	*	*	*	*	*	*	*	*
98-36	0.20	1.45	1.3	*	0.343	*	*	*	*	*	*	*	*
98-36	0.45	1.35	1.5	0.39	0.370	*	*	*	*	*	*	*	*
98-36	0.82	1.28	7.7	2.07	0.722	*	*	*	*	*	*	*	*
98-36	1.25	0.98	15.0	3.40	0.905	*	*	*	*	*	*	*	*
98-36	1.75	0.91	27.9	4.84	0.991	*	*	*	*	*	*	*	*
98-42	0.00	*	*	*	*	1.16	*	*	*	*	*	*	*
98-42	0.00	*	*	*	*	1.10	*	*	*	*	*	*	*
98-42	0.20	*	*	*	*	1.13	16.1	3.28	0.827	*	*	*	*
98-42	0.45	*	*	*	*	1.12	24.0	4.04	0.915	*	*	*	*
98-42	0.82	*	*	*	*	1.06	34.3	4.98	0.944	*	*	*	*
98-42	1.25	*	*	*	*	1.17	43.4	5.36	0.968	*	*	*	*
98-42	1.75	*	*	*	*	1.11	55.1	6.18	0.977	*	*	*	*
98-47	0.00	0.83	*	*	*	1.13	*	*	*	1.22	*	*	*
98-47	0.00	*	*	*	*	1.12	*	*	*	1.04	*	*	*
98-47	0.20	0.83	3.9	1.81	0.590	1.13	10.9	2.15	0.749	1.14	17.5	2.43	0.857
98-47	0.45	0.84	6.9	2.45	0.698	1.13	17.3	3.40	0.869	1.16	22.5	3.83	0.890
98-47	0.82	0.85	10.4	3.02	0.821	1.06	25.0	4.24	0.921	1.10	30.3	4.59	0.854
98-47	1.25	0.91	20.0	4.09	0.944	1.10	39.0	5.21	0.965	1.16	40.0	5.14	0.962
98-47	1.75	0.92	24.5	4.76	0.988	1.14	54.0	6.03	0.988	1.29	62.0	6.08	0.980
98-51	0.00	*	*	*	*	1.12	*	*	*	1.16	*	*	*
98-51	0.00	*	*	*	*	1.10	*	*	*	1.12	*	*	*
98-51	0.20	*	*	*	*	1.07	6.5	2.08	*	1.14	11.0	2.67	0.782
98-51	0.45	*	*	*	*	1.04	9.7	2.62	0.785	1.14	13.9	3.02	0.830
98-51	0.82	*	*	*	*	1.01	13.4	3.15	0.878	1.07	20.3	3.79	0.759
98-51	1.25	*	*	*	*	1.05	24.4	4.21	0.960	1.13	34.0	4.80	0.935
98-51	1.75	*	*	*	*	0.98	40.0	5.60	0.975	1.34	61.7	5.95	0.949
98-55	0.00	0.88	*	*	*	1.10	*	*	*	1.17	*	*	*
98-55	0.00	0.85	*	*	*	1.08	*	*	*	1.10	*	*	*
98-55	0.20	0.93	3.6	1.62	0.616	1.10	7.1	2.15	*	1.12	11.4	2.75	0.848
98-55	0.45	0.84	5.9	2.25	0.787	1.11	11.3	2.74	0.887	1.18	15.4	3.12	0.889
98-55	0.82	0.84	10.4	3.04	0.892	1.01	17.9	3.66	0.943	1.10	24.8	4.14	0.850
98-55	1.25	0.83	14.8	3.72	0.900	1.07	29.0	4.55	0.968	1.16	38.9	5.07	0.986
98-55	1.75	0.75	17.4	4.20	0.959	1.00	40.1	5.55	0.980	1.33	50.9	5.42	0.982
98-57	0.00	0.99	*	*	*	1.07	*	*	*	1.12	*	*	*
98-57	0.00	0.97	*	*	*	1.02	*	*	*	1.08	*	*	*
98-57	0.20	0.94	4.4	1.80	0.176	1.01	5.3	1.92	*	1.07	8.8	2.45	0.715
98-57	0.45	0.92	5.2	2.01	0.270	0.99	7.2	2.30	0.624	1.07	10.3	2.67	0.757
98-57	0.82	0.89	6.5	2.29	0.606	0.96	8.3	2.52	0.750	*	13.9	*	0.725
98-57	1.25	0.92	11.2	3.01	0.801	0.98	14.9	3.39	0.892	*	24.7	*	0.917
98-57	1.75	0.88	16.0	3.71	0.942	0.99	26.4	4.51	0.957	*	*	*	0.962

*Instrumentation failed.

Table VI. 12.5° Cone Frustum Pressure Data

Pressure orifice	p/p_s for test—								
	98-8	98-11	98-12	98-14	98-15	98-16	98-27	98-28	98-29
1	0.06806	0.09210	0.14292	0.06248	0.08207	0.18025	0.05319	0.06053	0.05353
2	0.06041	0.08463	0.14059	0.06272	0.08482	0.16925	0.04835	0.05555	0.04899
3	0.05899	0.08679	0.15316	0.06489	0.08717	0.17108	0.04796	0.05539	0.04837
4	0.05741	0.08656	0.15599	0.06567	0.08713	0.16375	0.04627	0.05401	0.04692
5	0.05511	0.08839	0.16240	0.06539	0.08698	0.16920	0.04442	0.05266	0.04507
6	0.05229	0.08991	0.16975	0.06410	0.08619	0.16718	0.04123	0.05018	0.04177
7	0.05360	0.09426	0.17250	0.06575	0.08745	0.16477	0.04168	0.05179	0.04244
8	0.05603	0.09892	0.17412	0.06877	0.09142	0.17034	0.04408	0.05524	0.04492
9	0.05658	0.10154	0.17015	0.06771	0.08997	0.16164	0.04365	0.05554	0.04439
10	0.06158	0.11227	0.17281	0.07170	0.09339	0.16701	0.04579	0.06182	0.04704
11	0.06529	0.11972	0.18000	0.07444	0.09645	0.17430	0.04781	0.06681	0.04904
12	0.06636	0.12008	0.17680	0.07238	0.09404	0.17268	0.04837	0.06920	0.04986
13	0.07021	0.12424	0.17772	0.07372	0.09607	0.17569	0.05020	0.07488	0.05182
14	0.07093	0.11748	0.16868	0.06791	0.09187	0.17050	0.05220	0.07846	0.05401
15	*	*	*	*	*	*	*	*	*
16	0.07300	0.11664	0.17000	0.07177	0.09414	0.17441	0.05713	0.08783	0.05910
17	0.07419	0.11475	0.16850	0.07248	0.09309	0.16856	0.06012	0.09068	0.06144
18	0.07731	0.11893	0.17690	0.07528	0.09723	0.17418	0.06230	0.09546	0.06385
19	0.05487	0.07578	0.11862	0.06455	0.07985	0.12828	0.04335	0.04954	0.04403
20	0.05460	0.05167	0.05358	0.06320	0.06124	0.05694	0.04255	0.04285	0.04315
21	0.07465	0.07280	0.06678	0.07754	0.07354	0.06435	0.06167	0.06205	0.06253
22	0.05179	0.03797	0.02737	0.06197	0.04771	0.02137	0.04213	0.03926	0.04250
23	0.06994	0.04211	0.02114	0.07116	0.05676	0.02577	0.05621	0.04420	0.05757
24	0.04893	0.03262	0.02304	0.06012	0.04337	0.02023	0.04110	0.03717	0.04148
25	0.06599	0.03977	0.02666	0.06416	0.05383	0.02538	0.05615	0.04284	0.05739
26	0.05163	0.03837	0.02821	0.06346	0.04888	0.02249	0.04268	0.03995	0.04317
27	0.05258	0.05208	0.05586	0.06307	0.06226	0.06243	0.04267	0.04383	0.04359
28	0.06720	0.06392	0.06133	0.06691	0.06348	0.06193	0.05392	0.05561	0.05580
29	0.04710	0.06717	0.10871	0.05600	0.06895	0.11437	0.04114	0.04749	0.04202
30	0.06754	0.09845	0.13192	0.06971	0.08285	0.13261	0.05747	0.07902	0.05880

Pressure orifice	p/p_s for test—										
	98-31	98-33	98-36	98-37	98-40	98-42	98-43	98-46	98-51	98-55	98-57
1	0.10985	0.05283	0.06734	0.17816	0.05183	0.07720	0.05938	0.10926	0.06676	0.06613	0.07342
2	0.11113	0.04944	0.06316	0.16420	0.04781	0.07052	0.05466	0.10725	0.05965	0.06096	0.05959
3	0.12033	0.05061	0.06736	0.16777	0.04818	0.07264	0.05589	0.11161	0.05868	0.05891	0.05884
4	0.12740	0.05041	0.06794	0.16186	0.04782	0.07272	0.05589	0.11190	0.05644	0.05608	0.05604
5	0.13852	0.05054	0.06948	0.16289	0.04731	0.07389	0.05551	0.11492	0.05573	0.05446	0.05609
6	0.15322	0.04871	0.06911	0.16397	0.04516	0.07374	0.05369	0.11632	0.05259	0.05095	0.05316
7	0.16954	0.05087	0.07304	0.15997	0.04691	0.07727	0.05613	0.12043	0.05390	0.05242	*
8	0.18413	0.05483	0.07869	0.16679	0.05036	0.08325	0.06017	0.12943	0.05599	0.05431	0.05401
9	0.18097	0.05507	0.07941	0.15793	0.05068	0.08248	0.06021	0.12528	0.05561	0.05440	0.05671
10	0.17956	0.06154	0.08844	0.16422	0.05624	0.09075	0.06637	0.13016	0.05966	0.05966	0.05910
11	0.18219	0.06487	0.09410	0.17333	0.06022	0.09742	0.07059	0.13799	0.06249	0.06355	0.06120
12	0.17447	0.06605	0.09369	0.16981	0.06120	0.09607	0.07038	0.13394	0.06247	0.06427	0.06175
13	0.17745	0.06790	0.09578	0.17636	0.06388	0.09714	0.07192	0.13520	0.06440	0.06714	0.06297
14	0.17175	0.06833	0.09209	0.17206	0.06525	0.09337	0.07072	0.12853	0.06571	0.06886	0.06362
15	*	*	*	*	*	*	*	*	*	*	*
16	0.17628	0.07164	0.09230	0.17668	0.06891	0.09430	0.07238	0.12897	0.06953	0.07278	0.06663
17	0.17166	0.07292	0.09205	0.17340	0.07066	0.09330	0.07306	0.12635	0.07160	0.07452	0.06888
18	0.17729	0.07452	0.09434	0.18001	0.07238	0.09585	0.07441	0.13133	0.07274	0.07592	0.06966
19	0.09806	0.04920	0.06314	0.12840	0.04619	0.06788	0.05562	0.09403	0.05551	0.05407	*
20	0.04467	0.04724	0.04911	0.05043	0.04428	0.05258	0.05363	0.04962	0.05415	0.05182	0.07445
21	0.07031	0.07261	0.07387	0.06726	0.07103	0.07411	0.07537	0.07167	0.07260	0.07394	0.07436
22	0.02825	0.04817	0.04109	0.02549	0.04451	0.04297	0.05435	0.03374	0.05494	0.05250	0.05317
23	0.04898	0.06836	0.05363	0.02355	0.06644	0.05528	0.07096	0.03748	0.06807	0.06959	0.06302
24	0.02709	0.04639	0.03726	0.02488	0.04326	0.03863	0.05272	0.03038	0.05347	0.05104	0.05297
25	0.05132	0.05835	0.05089	0.04882	0.05696	0.05187	0.05911	0.03933	0.05924	0.06143	0.05596
26	0.02884	0.04859	0.04182	0.02611	0.04530	0.04339	0.05465	0.03481	0.05533	0.05338	0.05468
27	0.04668	0.05097	0.05030	0.05580	0.04601	0.05382	0.05528	0.05215	0.05540	0.05398	0.05516
28	0.06421	0.06338	0.06360	0.06161	0.06168	0.06354	0.06356	0.06384	0.06321	0.06606	0.06104
29	0.09675	0.04810	0.06063	0.12464	0.04447	0.06465	0.05140	0.09135	0.05312	0.05192	0.05237
30	0.13594	0.07089	0.08565	0.13849	0.06775	0.08549	0.07031	0.10806	0.06915	0.07259	0.06751

*Instrumentation failed.

Table VII. Heat-Transfer and Wall Temperature Data

[Data not included from tests 98-9, 98-17, and 98-47 because rakes were fixed in out-position]

Thermocouple no.	Test 98-8		Test 98-11		Test 98-12		Test 98-14		Test 98-15		Test 98-16		Test 98-27		Test 98-28		Test 98-29		Test 98-31	
	$\dot{q}/\dot{q}_s$	T_w, °R	$\dot{q}/\dot{q}_s$	T_w, °R	$\dot{q}/\dot{q}_s$	T_w, °R	$\dot{q}/\dot{q}_s$	T_w, °R	$\dot{q}/\dot{q}_s$	T_w, °R	$\dot{q}/\dot{q}_s$	T_w, °R	$\dot{q}/\dot{q}_s$	T_w, °R	$\dot{q}/\dot{q}_s$	T_w, °R	$\dot{q}/\dot{q}_s$	T_w, °R	$\dot{q}/\dot{q}_s$	T_w, °R
T1	0.049	594.1	0.069	593.0	0.097	603.6	0.045	625.6	0.067	599.2	0.356	841.1	0.007	539.7	0.007	538.6	0.001	533.8	0.092	580.4
T2	0.046	588.3	0.067	591.1	0.098	612.3	0.043	638.3	0.071	615.2	0.337	844.7	0.009	544.2	0.011	543.4	0.004	531.2	0.109	627.9
T3	0.044	589.5	0.065	593.5	0.100	623.7	0.045	640.6	0.075	636.8	0.318	837.5	0.011	548.1	0.015	547.7	0.005	541.4	0.131	657.0
T4	0.042	586.5	0.066	593.7	0.101	637.0	0.042	648.4	0.084	648.5	0.314	836.2	0.013	550.0	0.017	550.5	0.006	543.7	0.158	678.0
T5	0.040	588.5	0.066	602.2	0.111	651.5	0.049	658.5	0.099	664.9	0.317	836.7	0.015	554.7	0.023	556.0	0.009	547.3	0.188	712.9
T6	0.039	585.1	0.066	604.1	0.133	679.6	0.057	657.7	0.114	689.2	0.305	830.6	0.017	555.4	0.029	560.0	0.011	549.3	0.222	746.7
T7	0.038	589.5	0.068	610.6	0.155	705.3	0.066	671.1	0.130	705.4	0.301	827.9	0.020	559.3	0.034	566.6	0.014	554.0	0.254	772.7
T8	0.037	591.0	0.069	616.2	0.176	722.1	0.077	686.5	0.147	711.3	0.298	827.2	0.023	563.2	0.041	573.0	0.017	559.9	0.272	800.6
T9	0.037	587.1	0.071	625.3	0.218	752.7	0.101	705.1	0.162	739.0	0.290	822.3	0.029	569.9	0.056	584.4	0.024	566.4	0.290	819.0
T10	0.033	590.8	0.074	636.7	0.244	767.8	0.114	723.0	0.170	741.1	0.285	823.7	0.033	574.6	0.066	592.9	0.029	573.4	0.286	825.4
T11	0.034	595.1	0.090	652.0	0.278	791.5	0.126	745.4	0.180	756.4	0.293	830.8	0.038	582.0	0.078	604.2	0.034	580.1	0.296	834.0
T12	0.036	601.0	0.136	679.8	0.304	803.4	0.146	759.8	0.183	759.4	0.290	833.4	0.047	593.2	0.098	622.0	0.044	593.8	0.301	836.3
T13	0.040	616.0	0.178	726.8	0.318	833.3	0.154	785.9	0.187	782.9	0.296	860.4	*	*	*	*	*	*	*	*
T14	0.039	613.1	0.164	710.1	0.314	827.5	0.153	779.9	0.187	780.6	0.294	856.4	*	*	*	*	*	*	*	*
T15	0.049	634.1	0.215	762.6	0.316	845.3	0.161	795.5	0.188	791.8	0.289	869.9	0.066	638.1	0.141	676.8	0.062	641.1	0.310	878.6
T16	0.058	636.5	0.225	771.5	0.318	845.7	0.163	800.0	0.189	791.7	0.290	868.1	0.070	643.4	0.151	683.0	0.068	645.9	0.311	877.1
T17	0.065	643.0	0.225	776.9	0.313	850.3	0.162	797.8	0.188	792.7	0.287	870.2	0.073	654.0	0.156	690.8	0.073	658.8	0.305	883.8
T18	0.090	658.3	0.223	767.6	0.299	835.6	0.162	789.0	0.178	775.3	0.274	850.2	0.087	661.9	0.167	694.0	0.087	666.4	0.296	863.7
T19	0.110	675.2	0.229	781.9	0.310	847.7	0.169	799.9	0.182	784.4	0.276	858.8	0.098	681.8	0.177	707.5	0.096	685.1	0.296	874.8
T20	0.040	584.3	0.061	590.1	0.095	607.0	0.043	643.1	0.076	633.6	0.271	793.4	0.013	548.8	0.019	549.5	0.007	541.6	0.145	668.3
T21	0.036	591.9	0.068	625.7	0.214	739.0	0.118	724.0	0.177	726.8	0.277	815.7	0.035	575.2	0.064	589.3	0.029	573.6	0.283	812.7
T22	0.037	600.9	0.153	698.5	0.306	806.8	0.161	778.1	0.192	774.1	0.289	839.8	0.054	605.9	0.106	632.4	0.051	607.1	0.304	841.6
T23	0.057	624.1	0.221	753.6	0.314	821.2	0.170	792.0	0.192	781.6	0.285	845.7	0.072	639.1	0.147	670.5	0.071	642.8	0.306	849.1
T24	0.078	651.4	0.220	767.2	0.292	824.2	0.170	796.3	0.185	779.0	0.270	839.9	0.091	681.4	0.165	692.9	0.092	681.0	0.291	851.9
T25	0.040	583.9	0.055	585.9	0.074	599.3	0.047	628.4	0.068	628.9	0.208	732.3	0.013	549.1	0.016	548.6	0.008	542.7	0.109	632.1
T26	0.034	586.0	0.056	611.7	0.152	680.9	0.112	695.8	0.160	714.6	0.240	761.2	0.032	572.8	0.055	579.9	0.027	574.0	0.239	756.4
T27	0.038	595.1	0.118	662.0	0.251	745.2	0.154	748.0	0.176	752.1	0.244	774.5	0.052	598.4	0.093	613.0	0.047	602.3	0.257	784.3
T28	0.053	613.8	0.182	710.5	0.257	756.4	0.157	756.3	0.170	748.2	0.237	777.9	0.068	629.2	0.118	641.7	0.066	631.4	0.251	783.0
T29	0.040	583.4	0.050	580.4	0.056	578.5	0.049	623.5	0.064	625.3	0.159	685.8	0.012	547.8	0.013	545.2	0.008	544.3	0.072	598.0
T30	0.036	580.7	0.048	594.7	0.098	631.7	0.116	692.1	0.150	702.4	0.190	706.4	0.032	571.6	0.046	570.6	0.029	572.5	0.165	683.6
T31	0.037	593.4	0.078	626.8	0.180	684.0	0.147	728.8	0.157	724.8	0.186	708.0	0.049	595.1	0.074	595.1	0.048	600.4	0.195	717.1
T32	0.074	635.7	0.167	697.4	0.189	700.0	0.154	740.7	0.153	725.3	0.180	712.2	0.076	639.5	0.115	632.9	0.076	645.5	0.194	724.1
T33	0.040	580.8	0.041	571.9	0.040	564.6	0.049	614.2	0.055	609.4	0.108	636.9	0.013	545.2	0.009	540.9	0.006	542.7	0.044	570.1
T34	0.035	582.0	0.037	578.0	0.054	588.5	0.114	680.9	0.129	690.2	0.134	650.6	0.031	567.6	0.036	560.6	0.027	569.5	0.095	616.4
T35	0.133	676.8	0.126	659.1	0.134	647.6	0.159	734.6	0.143	706.7	0.125	648.5	0.076	635.0	0.092	607.8	0.073	642.2	0.146	667.9
T36	0.038	577.5	0.032	563.6	0.027	553.7	0.045	605.7	0.041	591.0	0.065	593.4	0.010	540.8	0.006	535.3	0.005	539.3	0.024	551.2
T37	0.036	585.9	0.030	572.2	0.026	566.9	0.120	690.5	0.113	675.7	0.094	618.9	0.030	569.1	0.024	554.2	0.025	569.0	0.053	580.4
T38	0.040	593.8	0.030	578.3	0.057	585.7	0.151	724.0	0.136	697.8	0.096	616.5	0.047	589.1	0.041	565.8	0.044	592.5	0.068	590.6
T39	0.046	607.1	0.093	626.8	0.084	601.0	0.153	724.8	0.133	691.9	0.087	610.3	0.063	612.0	0.055	578.6	0.061	616.9	0.075	598.5
T40	0.072	635.7	0.103	641.1	0.088	608.9	0.151	726.5	0.132	695.5	0.085	612.3	0.071	627.3	0.067	590.4	0.068	633.1	0.095	618.9
T41	0.038	578.3	0.028	560.0	0.018	545.3	0.047	607.8	0.033	579.3	0.033	563.3	0.011	538.1	0.003	531.7	0.005	537.7	0.010	537.9
T42	0.033	582.6	0.020	559.3	0.015	548.9	0.123	686.0	0.089	646.3	0.068	586.0	0.030	561.8	0.016	542.8	0.025	563.8	0.030	556.3
T43	0.038	594.5	0.023	564.5	0.024	555.0	0.157	726.9	0.125	680.0	0.075	587.7	0.047	583.1	0.028	551.9	0.044	588.7	0.039	562.6
T44	0.068	623.7	0.028	573.3	0.048	569.8	0.163	730.7	0.128	683.7	0.071	586.5	0.064	606.1	0.041	562.6	0.061	611.9	0.039	566.0
T45	0.088	641.1	0.050	586.1	0.050	578.2	0.154	723.0	0.126	680.2	0.065	584.6	0.071	616.7	0.049	570.1	0.069	625.4	0.042	567.6
T46	0.037	576.0	0.023	554.5	0.013	540.2	0.046	606.7	0.024	566.1	0.008	541.7	0.011	535.3	0.002	528.6	0.005	535.0	0.002	528.9
T47	0.039	580.9	0.015	552.4	0.010	542.0	0.123	672.5	0.064	612.1	0.049	561.1	0.028	556.2	0.011	535.3	0.023	558.6	0.014	538.6
T48	*	*	0.020	559.6	0.013	545.4	0.159	719.0	0.105	656.2	0.064	579.0	0.044	578.8	0.024	543.5	0.042	584.0	0.025	547.3
T49	0.086	631.9	0.029	567.6	0.027	554.4	0.166	731.5	0.123	673.6	0.070	583.5	0.063	602.1	0.031	551.1	0.061	608.7	0.028	551.5
T50	0.089	635.4	0.042	578.3	0.039	563.3	0.141	702.3	0.109	659.1	0.066	587.7	0.069	610.7	0.036	556.6	0.065	617.5	0.034	555.5
T51	*	*	0.009	542.1	*	*	0.017	544.2	*	*	0.003	525.0	*	*	0.001	533.0	*	*	0.000	532.7
T52	0.045	587.0	0.032	563.9	0.020	543.5	0.050	600.8	0.028	566.3	0.011	536.5	0.006	529.4	−0.001	526.0	0.001	529.7	0.000	526.3
T53	0.042	580.0	0.029	558.4	0.016	541.3	0.050	603.9	0.028	565.6	0.016	540.2	0.007	529.5	0.000	525.5	0.002	529.8	0.000	525.8
T54	0.040	578.0	0.026	556.1	0.014	540.0	0.050	606.7	0.028	566.5	0.020	543.2	0.010	531.8	0.002	526.5	0.004	531.9	0.000	526.5
T55	0.038	576.2	0.022	553.0	0.012	538.1	0.050	608.0	0.027	566.2	0.022	544.8	0.011	532.7	0.002	526.2	0.005	533.0	0.000	525.9
T56	0.035	574.1	0.021	551.4	0.010	536.8	0.049	609.9	0.026	566.5	0.026	547.4	0.013	534.9	0.004	526.9	0.007	534.9	0.000	525.8
T57	0.035	575.2	0.019	551.6	0.009	537.9	0.052	616.5	0.027	570.4	0.030	551.9	0.015	539.4	0.003	529.7	0.008	539.8	0.000	528.4
T58	0.034	575.7	0.019	551.1	0.008	538.0	0.058	625.5	0.035	581.3	0.033	554.5	0.018	542.5	0.004	530.4	0.011	542.9	0.001	528.9
T59	0.032	573.8	0.016	548.9	0.007	537.1	0.066	630.8	0.048	592.0	0.033	553.9	0.019	544.1	0.005	530.4	0.014	545.1	0.002	528.7
T60	0.031	576.5	0.014	549.4	0.004	539.0	0.089	657.3	0.081	623.8	0.038	557.7	0.023	550.9	0.008	533.2	0.019	553.6	0.006	532.0
T61	0.030	576.0	0.013	548.2	0.005	538.4	0.105	669.3	0.094	636.7	0.041	558.8	0.027	554.5	0.010	534.0	0.023	557.8	0.010	533.0
T62	0.032	580.0	0.011	548.5	0.005	540.0	0.122	686.4	0.101	642.3	0.040	558.8	0.032	560.8	0.012	536.3	0.026	562.4	0.013	535.8
T63	0.025	567.8	0.008	543.6	0.009	537.9	0.105	646.6	0.112	648.1	0.034	556.3	0.040	571.3	0.016	538.6	0.037	575.6	0.020	539.0

*Failed or no thermocouple.

Table VII. Continued

Thermocouple no.	Test 98-33		Test 98-36		Test 98-37		Test 98-40		Test 98-42		Test 98-43		Test 98-46		Test 98-51		Test 98-55		Test 98-57	
	$\dot{q}/\dot{q}_s$	T_w, °R	$\dot{q}/\dot{q}_s$	T_w, °R	$\dot{q}/\dot{q}_s$	T_w, °R	$\dot{q}/\dot{q}_s$	T_w, °R	$\dot{q}/\dot{q}_s$	T_w, °R	$\dot{q}/\dot{q}_s$	T_w, °R	$\dot{q}/\dot{q}_s$	T_w, °R	$\dot{q}/\dot{q}_s$	T_w, °R	$\dot{q}/\dot{q}_s$	T_w, °R	$\dot{q}/\dot{q}_s$	T_w, °R
T1	0.030	510.3	0.053	553.0	0.271	727.0	0.012	540.9	0.082	612.9	0.049	575.9	0.126	661.1	0.000	502.7	0.008	517.1	0.000	477.4
T2	0.035	516.0	0.065	567.5	0.297	751.3	0.017	547.0	0.091	626.9	0.056	584.9	0.149	692.7	0.001	504.1	0.027	533.7	0.000	480.9
T3	0.038	531.5	0.077	582.7	0.310	769.4	0.020	552.6	0.101	638.3	0.062	591.8	0.167	713.5	0.001	508.2	0.044	548.2	0.000	482.8
T4	0.042	543.5	0.088	595.4	0.318	779.8	0.024	556.2	0.112	648.2	0.068	596.4	0.184	730.5	0.002	512.3	0.056	557.5	0.000	453.9
T5	0.048	561.1	0.099	611.7	0.330	796.5	0.028	562.4	0.125	661.4	0.074	603.8	0.202	750.7	0.006	518.2	0.066	567.1	-0.001	457.1
T6	0.060	550.9	0.111	627.0	0.335	802.0	0.034	566.4	0.140	673.6	0.083	609.3	0.218	766.6	0.011	523.8	0.076	573.2	0.001	452.4
T7	0.068	549.4	0.123	644.8	0.337	807.3	0.040	573.4	0.153	686.6	0.091	617.8	0.231	783.1	0.017	534.0	0.085	581.1	0.001	470.7
T8	0.076	558.8	0.134	661.1	0.335	809.8	0.046	580.5	0.167	697.4	0.099	625.1	0.243	795.9	0.025	545.4	0.091	587.8	0.006	478.2
T9	0.093	584.0	0.158	691.2	0.336	813.5	0.060	594.5	0.187	718.4	0.116	638.7	0.253	809.4	0.041	565.9	0.103	597.3	0.015	489.5
T10	0.102	585.5	0.168	703.8	0.328	807.0	0.068	602.7	0.195	724.6	0.124	645.3	0.255	809.2	0.053	578.2	0.109	601.3	0.021	493.7
T11	0.110	604.8	0.183	722.2	0.335	813.5	0.078	611.9	0.208	735.0	0.136	654.7	0.264	817.8	0.065	592.2	0.117	607.7	0.023	498.1
T12	0.127	615.5	0.196	734.9	0.333	809.4	0.092	626.4	0.213	739.1	0.149	662.3	0.261	815.7	0.082	611.5	0.126	614.5	0.053	516.5
T16	*	*	*	*	*	*	*	*	*	*	*	*	*	*	*	*	0.134	630.5	0.061	531.8
T14	*	*	*	*	*	*	*	*	*	*	*	*	*	*	*	*	0.001	625.8	*	*
T15	0.152	661.1	0.205	772.0	0.333	843.1	0.120	670.0	0.220	769.9	0.170	695.4	0.260	844.2	0.112	664.6	0.148	647.8	0.092	561.7
T16	0.158	653.6	0.206	772.3	0.329	845.2	0.126	673.5	0.222	768.7	0.174	694.7	0.259	842.5	0.118	667.7	0.152	647.4	0.099	561.9
T17	0.157	675.6	0.204	773.9	0.326	848.5	0.130	678.0	0.218	770.5	0.173	697.0	0.259	844.8	0.122	673.7	0.001	715.6	*	*
T18	0.159	659.4	0.196	760.7	0.315	830.9	0.133	672.1	0.211	751.4	0.168	683.4	0.243	819.4	0.126	670.9	0.155	645.0	0.115	572.1
T19	0.164	664.4	0.196	775.8	0.314	847.5	0.140	680.6	0.216	758.7	0.172	688.0	0.246	826.5	0.133	680.0	0.159	649.8	0.124	581.6
T20	0.048	531.7	0.087	591.1	0.305	764.8	0.025	555.7	0.110	644.7	0.070	595.9	0.173	721.0	0.011	523.4	0.077	571.8	0.000	452.3
T21	0.104	590.5	0.167	696.9	0.323	794.7	0.068	602.5	0.272	722.1	0.126	644.2	0.252	802.3	0.066	592.8	0.110	601.8	0.030	501.4
T22	0.135	637.6	0.203	745.8	0.334	811.6	0.101	640.1	0.221	751.2	0.162	674.4	0.262	822.0	0.098	634.2	0.136	625.0	0.075	530.4
T23	0.160	663.5	0.211	760.3	0.328	817.9	0.127	667.4	0.224	760.0	0.178	688.8	0.260	825.5	0.120	663.8	0.154	640.9	0.102	548.5
T24	0.165	661.4	0.204	757.6	0.312	816.9	0.137	679.5	0.217	757.2	0.176	690.0	0.245	819.0	0.131	679.5	0.159	648.8	0.117	562.2
T25	0.046	538.1	0.077	580.3	0.261	713.8	0.025	558.3	0.099	634.6	0.068	593.9	0.147	687.3	0.003	510.4	0.062	559.1	-0.001	453.5
T26	0.097	599.7	*	*	0.258	736.2	*	*	*	*	*	*	*	*	0.056	573.9	0.104	588.3	0.023	503.7
T27	0.131	626.2	0.184	713.2	0.283	745.0	0.098	630.8	0.202	722.5	0.155	659.6	0.233	774.2	0.091	615.2	0.131	611.4	0.050	506.8
T28	0.146	642.9	0.186	718.1	0.271	741.0	0.118	652.2	0.197	720.9	0.163	666.0	0.222	767.8	0.112	642.8	0.143	623.4	0.082	529.7
T29	0.047	547.5	0.064	560.5	0.187	640.3	0.025	555.4	0.088	617.1	0.071	592.5	0.107	646.0	0.004	510.0	0.060	557.0	-0.003	452.7
T30	0.100	595.6	0.131	640.3	0.220	675.3	0.069	597.5	0.157	675.4	0.127	634.5	0.182	713.9	0.063	578.5	0.110	593.1	0.028	508.4
T31	0.126	623.5	0.159	673.9	0.215	671.2	0.096	627.2	0.177	692.4	0.151	652.1	0.189	722.2	0.095	613.7	0.129	606.7	0.061	515.6
T32	0.142	651.1	0.169	684.6	0.205	667.0	0.123	655.3	0.176	693.5	0.158	659.3	0.181	720.1	0.123	649.6	0.146	622.0	0.105	562.5
T33	0.043	558.9	0.050	547.1	0.110	570.9	0.023	552.0	0.072	598.0	0.068	587.7	0.072	606.2	0.020	527.8	0.078	566.4	0.004	460.0
T34	0.100	598.2	0.112	609.9	0.165	616.1	0.067	593.5	0.133	650.8	0.127	631.4	0.133	663.0	0.082	588.7	0.112	591.9	0.060	519.3
T35	0.140	648.2	0.145	679.9	0.143	640.9	0.121	649.7	0.163	675.1	0.157	655.5	0.143	677.0	0.122	654.2	0.142	616.8	0.107	588.0
T36	0.040	557.0	0.040	541.7	0.063	542.3	0.022	547.4	0.058	580.2	0.067	582.6	0.045	576.7	0.003	508.2	0.052	548.1	-0.002	487.3
T37	0.094	606.8	0.086	598.5	0.097	560.5	0.064	593.7	0.106	630.3	0.124	631.6	0.088	620.2	0.053	571.5	0.105	590.3	0.016	508.7
T38	0.122	634.8	0.109	638.7	0.113	594.7	0.093	623.0	0.130	649.9	0.150	650.6	0.107	637.3	0.089	616.1	0.125	604.4	0.050	550.6
T39	0.133	645.5	0.122	663.9	0.104	602.1	0.109	641.3	0.142	659.1	0.153	653.4	0.114	648.6	0.107	643.1	0.134	613.5	0.078	557.8
T40	0.140	652.9	0.126	674.4	0.095	612.0	0.120	653.4	0.141	661.9	0.156	657.6	0.113	648.2	0.119	655.8	0.142	620.4	0.056	559.9
T41	0.038	553.9	0.027	534.1	0.037	528.2	0.021	544.5	0.045	566.0	0.065	578.9	0.024	555.3	0.010	517.2	0.060	553.8	0.002	494.5
T42	0.092	602.1	0.071	577.2	0.051	522.7	0.062	586.4	0.084	600.9	0.123	626.3	0.054	582.5	0.062	579.6	0.109	589.3	0.037	527.1
T43	0.122	629.9	0.088	609.1	0.061	548.6	0.094	618.5	0.108	622.5	0.150	648.0	0.071	597.1	0.093	621.4	0.128	604.5	0.033	539.0
T44	0.136	641.4	0.104	642.3	0.064	562.2	0.112	639.6	0.128	641.1	0.161	653.7	0.088	619.1	0.111	643.0	0.138	612.6	0.088	575.2
T45	0.141	643.4	0.104	642.1	0.072	575.5	0.119	646.7	0.124	636.6	0.158	651.0	0.081	619.6	0.120	646.3	0.143	614.8	0.100	584.9
T46	0.038	551.4	0.020	532.0	0.014	515.7	0.020	542.2	0.038	556.8	0.064	575.5	0.010	539.6	0.003	509.0	0.060	551.4	-0.001	492.0
T47	0.087	593.8	0.048	558.5	0.023	502.8	0.058	579.3	0.065	580.5	0.117	616.6	0.025	552.1	0.055	572.6	0.102	582.5	0.023	520.5
T48	0.118	623.6	0.070	587.6	0.029	534.4	0.089	612.8	0.087	600.3	0.145	639.9	0.034	562.2	0.088	616.0	0.125	600.1	0.058	554.6
T49	0.140	640.4	0.085	661.9	0.028	533.4	0.111	636.7	0.114	623.5	0.164	653.1	0.052	583.0	0.111	639.2	0.141	610.9	0.088	577.0
T50	0.132	630.7	0.080	621.6	0.029	545.3	0.112	635.8	0.109	616.2	0.148	638.3	0.062	590.2	0.115	633.1	0.136	604.7	0.097	583.8
T51	*	*	*	*	-0.001	532.5	*	*	*	*	*	*	*	*	*	*	*	*	0.000	489.8
T52	0.022	536.4	0.011	531.7	0.003	522.2	0.009	531.5	0.026	545.3	0.044	559.4	0.005	533.8	0.000	506.0	0.011	517.7	0.000	482.0
T53	0.027	539.6	0.012	533.0	0.001	524.1	0.014	533.5	0.029	546.5	0.051	563.4	0.004	532.8	0.001	502.7	0.032	530.6	0.000	482.1
T54	0.032	544.9	0.015	525.5	0.001	502.0	0.016	537.0	0.032	549.5	0.056	568.4	0.006	533.5	0.002	504.7	0.050	542.8	-0.001	487.2
T55	0.037	548.0	0.017	538.4	0.000	493.5	0.020	539.2	0.035	551.3	0.062	572.4	0.006	533.5	0.004	507.5	0.061	549.7	-0.001	488.3
T56	0.043	552.7	0.020	544.8	-0.005	502.5	0.024	542.8	0.040	554.4	0.070	577.8	0.007	533.8	0.009	513.8	0.070	555.9	0.000	490.6
T57	0.048	561.6	0.023	551.8	-0.004	488.2	0.027	549.7	0.041	559.0	0.074	584.4	0.007	536.4	0.017	526.0	0.076	563.6	0.002	497.6
T58	0.056	568.4	0.027	557.1	-0.006	487.3	0.033	555.1	0.046	563.1	0.084	591.7	0.009	537.4	0.026	536.4	0.082	568.3	0.004	502.5
T59	0.061	571.4	0.032	559.6	-0.003	486.2	0.037	558.1	0.048	564.2	0.089	594.1	0.012	537.2	0.033	544.9	0.087	570.8	0.009	506.3
T60	0.077	586.1	0.033	568.6	-0.003	487.9	0.049	571.4	0.056	572.6	0.107	609.3	0.011	539.4	0.048	566.2	0.096	579.0	0.018	517.1
T61	0.084	592.5	0.040	573.3	-0.008	488.1	0.056	578.0	0.058	575.2	0.116	615.3	0.012	539.7	0.059	576.7	0.100	581.4	0.030	526.3
T62	0.092	599.2	0.047	564.8	-0.004	487.5	0.064	586.2	0.062	578.5	0.121	621.2	0.012	541.2	0.065	586.6	0.107	586.7	0.038	535.8
T63	0.110	614.5	0.060	571.8	-0.003	487.1	0.079	600.6	0.076	588.3	0.140	632.0	0.015	542.8	0.085	606.5	0.112	590.5	0.055	549.4

*Failed or no thermocouple.

Table VII. Continued

Thermocouple no.	Test 98-8		Test 98-11		Test 98-12		Test 98-14		Test 98-15		Test 98-16		Test 98-27		Test 98-28		Test 98-29		Test 98-31	
	$\dot{q}/\dot{q}_s$	T_w, °R	$\dot{q}/\dot{q}_s$	T_w, °R	$\dot{q}/\dot{q}_s$	T_w, °R	$\dot{q}/\dot{q}_s$	T_w, °R	$\dot{q}/\dot{q}_s$	T_w, °R	$\dot{q}/\dot{q}_s$	T_w, °R	$\dot{q}/\dot{q}_s$	T_w, °R	$\dot{q}/\dot{q}_s$	T_w, °R	$\dot{q}/\dot{q}_s$	T_w, °R	$\dot{q}/\dot{q}_s$	T_w, °R
T64	0.030	583.2	0.010	550.3	0.016	545.5	0.137	704.1	0.104	646.4	0.037	558.3	0.042	574.1	0.018	540.6	0.041	580.9	0.020	539.9
T65	0.033	588.0	0.009	549.7	0.020	546.8	0.145	709.8	0.104	646.0	0.038	558.1	0.046	579.8	0.018	540.9	0.041	583.0	0.020	540.2
T66	0.038	596.7	0.014	556.8	0.027	553.3	0.155	722.8	0.117	660.3	0.042	563.9	0.057	594.0	0.029	548.3	0.054	600.0	0.024	544.4
T67	*	*	0.019	591.8	*	*	0.156	721.8	*	*	*	*	0.061	599.3	0.033	551.1	0.059	605.6	0.024	545.8
T68	0.049	605.8	0.024	561.4	0.030	553.6	0.154	721.7	0.113	661.4	0.040	565.2	0.065	602.2	0.046	556.7	0.062	609.6	0.025	545.5
T69	0.068	619.1	0.032	573.2	0.038	559.6	0.146	711.6	0.114	672.1	0.056	583.1	0.066	606.6	0.057	560.7	0.066	617.4	0.028	560.1
T70	0.081	628.1	0.043	579.8	0.043	567.5	0.151	716.9	0.129	677.2	0.064	592.9	0.081	601.2	0.062	566.8	0.074	628.2	0.032	555.8
T71	0.037	577.2	0.024	556.3	0.013	541.1	0.081	626.0	0.103	629.9	0.010	542.7	0.010	535.8	0.002	529.9	0.005	535.7	0.001	530.3
T72	0.034	579.4	0.016	551.1	0.017	548.1	0.164	727.4	0.114	648.7	0.054	573.4	0.028	555.5	0.012	536.1	0.023	558.3	0.014	540.3
T73	0.032	588.0	0.015	556.0	0.021	549.9	0.155	723.0	0.115	662.8	0.065	579.5	0.045	577.2	0.021	544.2	0.040	582.5	0.026	547.3
T74	0.039	600.1	0.031	571.5	0.043	565.1	0.148	718.9	0.119	676.6	0.064	585.6	0.060	599.9	0.030	554.7	0.057	607.3	0.018	557.3
T75	0.061	616.1	0.050	583.3	0.056	574.7	0.150	716.6	0.133	695.3	0.069	607.4	0.066	616.7	0.068	572.0	0.066	624.3	0.034	568.1
T76	0.036	577.8	0.027	560.0	0.019	546.8	0.044	606.1	0.033	570.1	0.036	565.0	0.010	538.8	0.003	533.9	0.004	538.3	0.011	538.6
T77	0.032	579.3	0.020	557.8	0.022	552.9	0.161	723.5	0.085	619.4	0.075	590.8	0.027	557.3	0.016	541.6	0.023	559.3	0.031	556.0
T78	0.031	589.8	0.027	573.0	0.044	567.7	0.158	729.1	0.118	670.0	0.074	592.0	0.044	580.1	0.028	553.9	0.039	585.1	0.039	565.8
T79	0.040	602.4	0.047	587.2	0.054	576.7	0.153	725.0	0.125	683.8	0.069	590.4	0.059	602.2	0.046	567.2	0.057	609.9	0.039	573.6
T80	0.039	580.6	0.033	566.2	0.029	557.6	0.047	607.8	0.041	584.8	0.068	598.9	0.010	543.1	0.005	538.4	0.006	540.5	0.024	554.7
T81	0.033	580.9	0.037	574.9	0.027	563.3	0.111	677.4	0.104	655.3	0.104	614.7	0.028	561.3	0.023	551.8	0.023	563.7	0.052	577.8
T82	0.031	586.2	0.049	588.8	0.081	595.5	0.147	713.3	0.129	681.5	0.094	609.4	0.043	579.9	0.040	564.1	0.039	585.5	0.066	590.3
T83	0.067	625.6	0.112	640.8	0.098	618.2	0.153	727.0	0.136	702.4	0.097	623.8	0.066	616.4	0.081	594.3	0.065	623.9	0.085	617.7
T84	0.039	580.8	0.042	573.8	0.051	576.0	0.044	606.5	0.050	580.3	0.112	639.7	0.010	546.8	0.008	544.2	0.004	543.3	0.042	572.5
T85	0.031	580.4	0.051	592.2	0.130	635.0	0.111	678.5	0.122	672.4	0.149	659.2	0.029	565.0	0.034	562.7	0.025	566.7	0.102	627.0
T86	0.080	628.4	0.133	659.3	0.126	644.6	0.135	712.1	0.125	692.3	0.118	650.1	0.065	610.7	0.087	606.0	0.067	624.2	0.127	660.7
T87	0.040	578.9	0.053	586.1	0.058	581.6	0.051	614.6	0.065	606.3	0.207	709.2	0.012	549.0	0.012	545.8	0.006	543.5	0.071	597.1
T88	0.059	593.7	0.147	664.8	0.183	683.2	0.128	703.0	0.179	725.4	0.197	700.8	0.030	568.4	0.045	572.4	0.024	570.0	0.174	691.6
T89	*	*	*	*	*	*	*	*	*	*	*	*	*	*	*	*	*	*	*	*
T90	0.126	670.1	0.173	697.5	0.206	709.0	0.161	749.7	0.162	736.5	0.195	712.6	0.066	615.7	0.102	622.4	0.063	624.3	0.203	737.5
T91	0.127	677.2	0.176	706.7	0.197	710.7	0.151	750.8	0.153	730.8	0.189	719.7	0.072	628.3	0.112	640.0	0.070	643.0	0.197	734.0
T92	0.040	586.2	0.056	586.6	0.075	603.7	0.046	627.3	0.068	622.0	0.247	754.8	0.011	550.3	0.013	550.2	0.005	544.0	0.105	633.5
T93	0.111	655.4	0.165	687.7	0.205	720.5	0.169	763.4	0.193	756.0	0.240	763.0	0.030	569.7	0.054	581.9	0.026	570.6	0.240	767.2
T94	0.119	668.7	0.160	698.7	0.249	748.5	0.161	764.5	0.178	754.2	0.245	776.0	0.025	594.8	0.091	614.9	0.046	599.8	0.253	786.6
T95	0.124	675.5	0.188	719.4	0.255	758.0	0.155	761.6	0.169	750.5	0.238	774.3	0.066	620.5	0.120	643.9	0.063	627.3	0.252	791.5
T96	0.128	686.1	0.199	731.9	0.249	770.2	0.151	769.8	0.166	755.5	0.236	786.0	0.081	651.0	0.138	667.2	0.078	658.3	0.250	802.8
T97	0.039	583.3	0.063	585.9	0.093	642.5	0.045	638.4	0.078	630.7	0.305	815.8	0.012	548.1	0.017	549.8	0.006	541.6	0.146	645.9
T98	0.048	595.4	0.067	625.7	0.203	736.3	0.116	718.1	0.165	730.3	0.274	802.9	0.015	546.1	0.031	556.4	0.012	548.6	0.129	666.2
T99	0.107	645.8	0.144	682.9	0.289	788.1	0.159	774.9	0.174	755.1	0.276	817.3	0.050	596.4	0.104	625.6	0.049	597.7	0.286	820.9
T100	0.125	679.8	0.206	738.6	0.293	802.9	0.160	777.5	0.173	765.0	0.271	822.3	0.067	624.8	0.137	663.1	0.065	629.9	0.285	836.9
T101	0.132	698.2	0.212	765.9	0.278	819.2	0.151	785.9	0.172	774.9	0.258	833.1	0.075	652.2	0.155	690.8	0.076	659.1	0.275	846.6
T126	*	*	*	*	*	*	0.123	627.4	0.140	636.3	0.233	659.2	-0.004	530.1	-0.024	524.6	*	*	*	*
T127	*	*	*	*	*	*	0.116	622.9	0.134	624.6	0.219	653.5	-0.004	535.8	-0.009	533.0	-0.009	530.6	0.002	537.6
T128	*	*	*	*	*	*	0.100	625.7	0.124	624.4	0.200	652.8	-0.002	538.4	-0.006	536.6	-0.007	533.4	0.008	543.4
T129	*	*	*	*	*	*	0.097	613.8	0.116	616.1	0.183	651.1	0.000	540.4	-0.004	538.1	-0.005	535.7	0.016	547.8
T130	*	*	*	*	*	*	0.087	607.9	0.108	596.3	0.174	650.6	0.001	541.6	-0.002	539.4	-0.003	537.5	0.024	550.4
T131	*	*	*	*	*	*	0.077	615.8	0.098	597.8	0.175	665.5	0.002	541.9	-0.001	539.9	-0.002	537.8	0.038	544.2
T132	*	*	*	*	*	*	0.074	617.4	0.095	587.3	0.184	676.4	0.003	541.9	0.000	540.6	-0.002	538.2	0.044	561.1
T133	*	*	*	*	*	*	0.068	613.5	0.087	590.4	0.193	686.8	0.005	542.4	0.002	541.6	-0.001	538.9	0.057	572.3
T134	*	*	*	*	*	*	0.119	626.5	0.116	619.0	0.122	594.9	-0.004	529.3	-0.009	525.1	-0.008	523.7	-0.006	524.7
T135	*	*	*	*	*	*	0.106	623.3	0.105	606.7	0.110	590.9	-0.004	533.7	-0.009	532.2	-0.009	530.0	-0.005	533.4
T136	*	*	*	*	*	*	0.098	616.8	0.096	599.3	0.102	586.7	-0.002	536.2	-0.007	535.4	-0.007	533.0	-0.001	536.5
T137	*	*	*	*	*	*	0.093	615.2	0.091	599.5	0.105	587.0	-0.001	537.7	-0.005	536.8	-0.006	534.8	0.002	539.1
T138	*	*	*	*	*	*	0.086	608.4	0.083	591.7	0.092	586.6	0.001	538.6	-0.004	537.8	-0.004	536.2	0.004	539.7
T139	*	*	*	*	*	*	0.078	599.2	0.076	575.6	0.082	581.0	0.002	539.2	-0.002	538.7	-0.003	537.5	0.008	539.5
T140	*	*	*	*	*	*	0.072	595.1	0.068	574.1	0.079	583.2	0.003	539.6	-0.001	539.1	-0.002	538.2	0.010	542.8
T141	*	*	*	*	*	*	0.069	595.1	0.068	571.8	0.079	589.4	0.004	540.3	0.000	539.9	-0.001	539.1	0.014	545.6
T142	*	*	*	*	*	*	0.123	636.0	0.099	609.4	0.060	564.2	-0.004	525.5	-0.005	523.2	-0.007	520.7	-0.004	522.6
T143	*	*	*	*	*	*	0.108	621.3	0.082	594.0	0.043	554.2	-0.004	528.8	-0.007	530.1	-0.009	527.4	-0.004	530.1
T144	*	*	*	*	*	*	0.100	618.6	0.071	591.1	0.032	553.4	-0.002	534.1	-0.007	535.2	-0.008	533.3	-0.004	535.1
T145	*	*	*	*	*	*	0.094	611.0	0.065	582.8	0.025	545.6	-0.001	531.1	-0.006	531.3	-0.006	530.5	-0.003	531.2
T146	*	*	*	*	*	*	0.087	610.4	0.058	583.1	0.020	546.6	0.001	535.9	-0.004	536.2	-0.004	536.0	-0.002	535.6
T147	*	*	*	*	*	*	0.078	596.2	0.051	571.8	0.014	539.4	0.002	532.4	-0.003	532.2	-0.003	533.0	-0.001	531.8
T148	*	*	*	*	*	*	0.074	594.4	0.048	570.8	0.011	538.6	0.003	532.9	-0.003	532.6	-0.002	533.8	-0.001	532.0
T149	*	*	*	*	*	*	0.068	595.1	0.043	570.0	0.008	540.9	0.004	537.5	-0.002	537.0	-0.001	538.9	-0.001	536.1

*Failed or no thermocouple.

Table VII. Concluded

Thermocouple no.	Test 98-33		Test 98-36		Test 98-37		Test 98-40		Test 98-42		Test 98-43		Test 98-46		Test 98-51		Test 98-55		Test 98-57	
	$\dot{q}/\dot{q}_s$	T_w, °R	$\dot{q}/\dot{q}_s$	T_w, °R	$\dot{q}/\dot{q}_s$	T_w, °R	$\dot{q}/\dot{q}_s$	T_w, °R	$\dot{q}/\dot{q}_s$	T_w, °R	$\dot{q}/\dot{q}_s$	T_w, °R	$\dot{q}/\dot{q}_s$	T_w, °R	$\dot{q}/\dot{q}_s$	T_w, °R	$\dot{q}/\dot{q}_s$	T_w, °R	$\dot{q}/\dot{q}_s$	T_w, °R
T64	0.109	615.8	0.059	579.8	-0.002	487.2	0.086	607.9	0.075	589.8	0.138	633.0	0.015	543.1	0.082	608.9	0.120	595.7	0.058	555.5
T65	0.118	620.3	0.058	581.3	-0.004	488.4	0.085	608.0	0.075	589.8	0.135	633.1	0.015	543.4	0.088	614.2	0.125	598.7	0.067	561.1
T66	0.128	630.4	0.073	596.6	-0.003	491.0	0.100	625.6	0.095	605.5	0.150	644.3	0.024	553.7	0.104	629.0	0.132	604.1	0.082	573.7
T67	0.131	633.2	0.080	606.9	-0.009	496.7	0.106	630.6	0.109	620.0	0.154	645.7	0.033	572.4	0.109	632.2	0.136	606.4	0.089	577.5
T68	0.136	635.2	0.090	624.1	-0.005	498.7	0.109	633.9	0.115	617.9	0.156	646.7	0.036	569.3	0.112	634.6	0.140	607.4	0.093	580.3
T69	0.134	632.6	0.098	633.9	0.008	516.4	0.111	636.2	0.132	623.2	0.152	642.3	0.046	581.7	0.116	631.9	0.138	605.1	0.099	585.0
T70	0.140	635.8	0.098	632.4	0.006	531.0	0.119	641.5	0.127	625.3	0.156	644.9	0.054	585.2	0.121	633.9	0.142	606.0	0.106	588.9
T71	0.037	550.9	0.020	524.5	0.012	498.0	0.019	541.9	0.036	556.8	0.062	575.3	0.011	540.7	0.007	515.9	0.061	554.0	-0.001	489.3
T72	0.087	594.1	0.049	560.4	0.027	509.3	0.058	578.7	0.066	581.3	0.117	617.5	0.026	554.3	0.007	581.8	0.102	583.9	0.044	532.9
T73	0.115	617.3	0.065	600.7	0.029	543.8	0.086	608.7	0.085	598.9	0.142	638.0	0.038	564.9	0.091	616.0	0.122	596.7	0.069	558.1
T74	0.129	631.6	0.089	632.6	0.035	564.0	0.103	631.4	0.113	625.7	0.151	647.4	0.055	593.3	0.107	633.6	0.134	607.1	0.089	581.3
T75	0.138	635.1	0.096	649.9	0.056	576.0	0.116	638.6	0.137	640.2	0.157	645.6	0.073	613.4	0.119	636.9	0.144	607.0	0.103	586.2
T76	0.032	548.2	0.026	531.5	0.036	541.5	0.019	544.6	0.041	564.9	0.061	578.0	0.025	555.9	0.003	509.4	0.053	547.4	-0.004	492.6
T77	0.087	589.1	0.061	580.9	0.053	528.9	0.057	579.6	0.080	595.9	0.115	619.0	0.054	580.6	0.053	566.6	0.102	581.0	0.022	517.9
T78	0.114	623.5	0.078	626.6	0.064	555.6	0.086	611.0	0.100	618.2	0.140	641.4	0.070	598.1	0.085	611.5	0.122	598.9	0.054	551.9
T79	0.131	638.5	0.098	661.5	0.072	586.6	0.105	633.4	0.126	641.7	0.151	650.0	0.090	631.2	0.104	634.7	0.135	609.3	0.081	577.2
T80	0.038	557.3	0.036	549.6	0.062	567.8	0.021	548.6	0.054	580.8	0.064	584.3	0.045	578.5	0.003	508.1	0.055	551.2	0.000	489.6
T81	0.090	592.3	0.079	607.6	0.099	558.7	0.059	584.1	0.097	620.3	0.117	624.0	0.087	616.1	0.046	560.4	0.104	585.3	0.024	520.7
T82	0.115	620.6	0.100	637.1	0.112	595.7	0.086	609.5	0.121	637.5	0.138	639.6	0.105	633.0	0.086	605.1	0.121	596.3	0.056	549.7
T83	0.134	642.1	0.110	681.1	0.095	629.7	0.111	640.9	0.135	663.0	0.148	650.0	0.109	652.6	0.111	643.2	0.137	610.2	0.095	585.2
T84	0.038	556.6	0.045	561.7	0.112	596.3	0.021	552.0	0.065	596.1	0.063	588.3	0.072	606.4	0.011	520.5	0.072	564.1	0.000	490.5
T85	0.094	591.9	0.104	609.9	0.172	626.3	0.062	588.2	0.125	647.9	0.118	627.5	0.138	668.3	0.075	584.0	0.109	589.3	0.050	527.2
T86	0.126	633.4	0.125	684.0	0.125	646.3	0.107	633.9	0.140	661.4	0.138	641.2	0.134	669.8	0.106	635.7	0.128	604.7	0.097	573.8
T87	0.042	543.9	0.060	560.9	0.190	642.9	0.023	554.0	0.083	614.3	0.066	591.8	0.105	645.1	0.003	509.1	0.051	553.8	0.001	479.9
T88	0.100	574.6	0.123	642.6	0.226	681.7	0.064	593.1	0.150	673.2	0.120	633.3	0.176	717.3	0.053	573.4	0.105	590.6	0.025	504.8
T89	*	*	*	*	*	*	*	*	*	*	*	*	*	*	*	*	*	*	*	*
T90	0.139	641.6	0.166	701.6	0.221	683.0	0.111	642.8	0.181	701.0	0.156	659.9	0.193	733.8	0.110	632.5	0.140	615.2	0.086	536.4
T91	0.145	653.3	0.165	711.0	0.218	684.5	0.122	654.8	0.174	699.6	0.158	662.5	0.186	729.1	0.120	647.0	0.148	621.9	0.102	547.0
T92	0.043	531.2	0.070	576.2	0.253	706.7	0.022	556.3	0.094	630.5	0.064	594.6	0.139	684.4	0.004	512.2	0.063	562.3	0.000	457.9
T93	0.098	578.0	0.144	671.0	0.275	740.1	0.065	596.0	0.170	695.3	0.120	636.7	0.141	760.5	0.062	581.2	0.107	595.4	0.031	507.7
T94	0.126	618.5	0.174	708.0	0.281	744.6	0.093	627.3	0.192	717.2	0.146	657.6	0.226	771.2	0.092	618.0	0.127	611.5	0.068	526.0
T95	0.145	640.1	0.180	720.7	0.271	744.5	0.114	646.9	0.193	719.0	0.158	663.5	0.220	769.3	0.113	634.7	0.144	614.3	0.096	531.6
T96	0.154	651.9	0.180	735.7	0.268	757.0	0.128	665.6	0.194	728.1	0.163	673.6	0.218	779.6	0.124	661.3	0.151	633.1	0.110	553.5
T97	0.042	559.1	0.082	588.8	0.302	759.2	0.024	555.0	0.107	642.1	0.067	594.5	0.173	717.3	0.004	510.8	0.062	559.7	-0.001	452.2
T98	0.049	557.7	0.087	614.1	0.163	669.0	0.035	562.0	0.094	626.6	0.063	582.6	*	*	0.031	552.3	0.055	560.6	0.017	514.2
T99	0.135	609.2	0.190	727.4	0.318	787.4	0.098	629.7	0.207	732.1	0.152	662.4	0.253	801.6	0.093	620.6	0.132	615.4	0.069	516.5
T100	0.149	646.0	0.194	739.5	0.308	794.9	0.119	654.9	0.206	740.1	0.164	675.4	0.244	804.2	0.113	650.1	0.146	630.7	0.096	539.0
T101	0.159	660.7	0.188	751.0	0.296	810.4	0.130	675.9	0.199	747.8	0.164	686.3	0.230	809.5	0.125	675.8	0.152	649.4	0.112	562.4
T126	-0.007	514.7	*	*	*	*	*	*	*	*	*	*	*	*	*	*	*	*	*	*
T127	0.001	526.0	0.006	500.8	0.043	536.5	-0.004	530.2	0.018	547.1	0.014	546.7	0.012	552.3	*	*	*	*	*	*
T128	0.002	530.6	0.010	504.7	0.079	546.0	-0.001	534.5	0.026	553.9	0.019	551.0	0.025	561.1	*	*	*	*	*	*
T129	0.005	531.9	0.015	510.4	0.115	554.0	0.000	536.0	0.034	559.2	0.023	553.3	0.038	569.5	*	*	*	*	*	*
T130	0.010	527.2	0.019	514.2	0.149	576.0	0.002	537.2	0.042	563.8	0.027	555.0	0.053	576.6	*	*	*	*	*	*
T131	0.013	532.6	0.025	518.8	0.186	602.8	0.004	538.0	0.050	568.8	0.031	557.5	0.068	586.0	*	*	*	*	*	*
T132	0.014	526.4	0.032	523.1	0.226	624.5	0.006	539.2	0.059	574.8	0.036	560.1	0.085	597.0	*	*	*	*	*	*
T133	0.018	529.3	0.040	529.5	0.265	652.4	0.007	540.7	0.070	582.5	0.042	563.6	0.101	610.3	*	*	*	*	*	*
T134	-0.002	515.1	0.000	500.6	0.005	509.5	-0.008	518.5	0.009	534.2	0.009	537.0	0.001	537.7	*	*	*	*	*	*
T135	0.000	524.8	0.003	503.7	0.013	507.6	-0.004	529.0	0.013	541.4	0.014	543.5	0.004	543.2	*	*	*	*	*	*
T136	0.002	527.0	0.005	505.8	0.022	510.1	-0.001	532.9	0.017	545.6	0.018	547.0	0.008	546.8	*	*	*	*	*	*
T137	0.004	531.5	0.007	506.1	0.031	519.7	-0.001	534.4	0.022	549.4	0.021	550.3	0.013	550.1	*	*	*	*	*	*
T138	0.007	533.7	0.012	506.0	0.036	529.7	0.000	535.4	0.026	551.2	0.025	551.6	0.017	552.8	*	*	*	*	*	*
T139	0.009	534.5	0.014	513.5	0.043	532.8	0.002	535.8	0.030	552.6	0.028	552.6	0.022	554.8	*	*	*	*	*	*
T140	0.012	534.8	0.013	518.2	0.056	527.8	0.004	536.6	0.033	554.6	0.032	554.0	0.026	557.1	*	*	*	*	*	*
T141	0.015	537.2	0.021	519.0	0.067	533.9	0.006	538.3	0.038	559.2	0.037	557.7	0.032	562.1	*	*	*	*	*	*
T142	-0.003	512.5	-0.005	496.0	-0.003	510.2	-0.006	515.0	0.006	530.1	0.008	533.9	-0.003	533.6	*	*	*	*	*	*
T143	0.000	523.4	-0.002	508.1	0.000	513.9	-0.004	525.4	0.010	536.0	0.013	539.3	0.000	537.5	*	*	*	*	*	*
T144	0.002	530.9	-0.001	517.9	0.002	521.8	-0.001	532.6	0.011	542.3	0.017	546.3	0.001	543.1	*	*	*	*	*	*
T145	0.004	528.1	0.000	517.3	0.000	521.4	0.000	529.7	0.014	538.9	0.021	543.4	0.002	538.3	*	*	*	*	*	*
T146	0.007	533.7	0.002	522.7	0.000	527.6	0.001	535.0	0.016	544.4	0.025	550.0	0.002	543.1	*	*	*	*	*	*
T147	0.009	529.9	0.001	522.2	0.005	516.4	0.002	531.0	0.017	539.7	0.027	545.1	0.002	538.0	*	*	*	*	*	*
T148	0.011	531.0	0.003	522.8	0.002	518.9	0.003	531.7	0.019	540.7	0.031	547.6	0.003	538.5	*	*	*	*	*	*
T149	0.014	536.7	0.005	527.7	0.001	534.4	0.005	536.6	0.020	546.0	0.035	553.8	0.004	543.3	*	*	*	*	*	*

*Failed or no thermocouple.

Table VIII. Results of Gas-Jet Turbulent Heat-Flux Analysis

Test (nose)	s_a/L	T_w, °R	$\dot{q}$ (measured), Btu/ft^2-sec	h, Btu/ft^2-sec-°R	T_{aw}, °R	$T_{aw} - T_w$, °R	$p_e M_e$, psia	M_e	Re*, 1/ft	Re$^\star s$	T_e, °R	$T^\star$, °R	$c_p^\star$, Btu/lbm-°R	$\mu^\star$, lbm/ft-sec	Pr*
98-17 (R-1)	0.40	595	8.89	0.01054	2762	2167	4.83	3.50	0.830×10^6	1.86×10^6	881	1152	0.284	19.4×10^{-6}	0.754
98-17 (R-1)	0.68	653	20.67	0.00915	2763	2110	5.48	4.42	0.862×10^6	3.62×10^6	628	1100	0.282	18.7×10^{-6}	0.758
98-29 (Gas jet)	0.40	554	1.81	0.00474	892	338	1.36	1.77	0.518×10^6	1.01×10^6	571	636	0.267	12.9×10^{-6}	0.747
98-29 (Gas jet)	0.68	606	6.13	0.00497	1563	957	1.78	2.00	0.475×10^6	1.83×10^6	922	905	0.276	16.3×10^{-6}	0.754

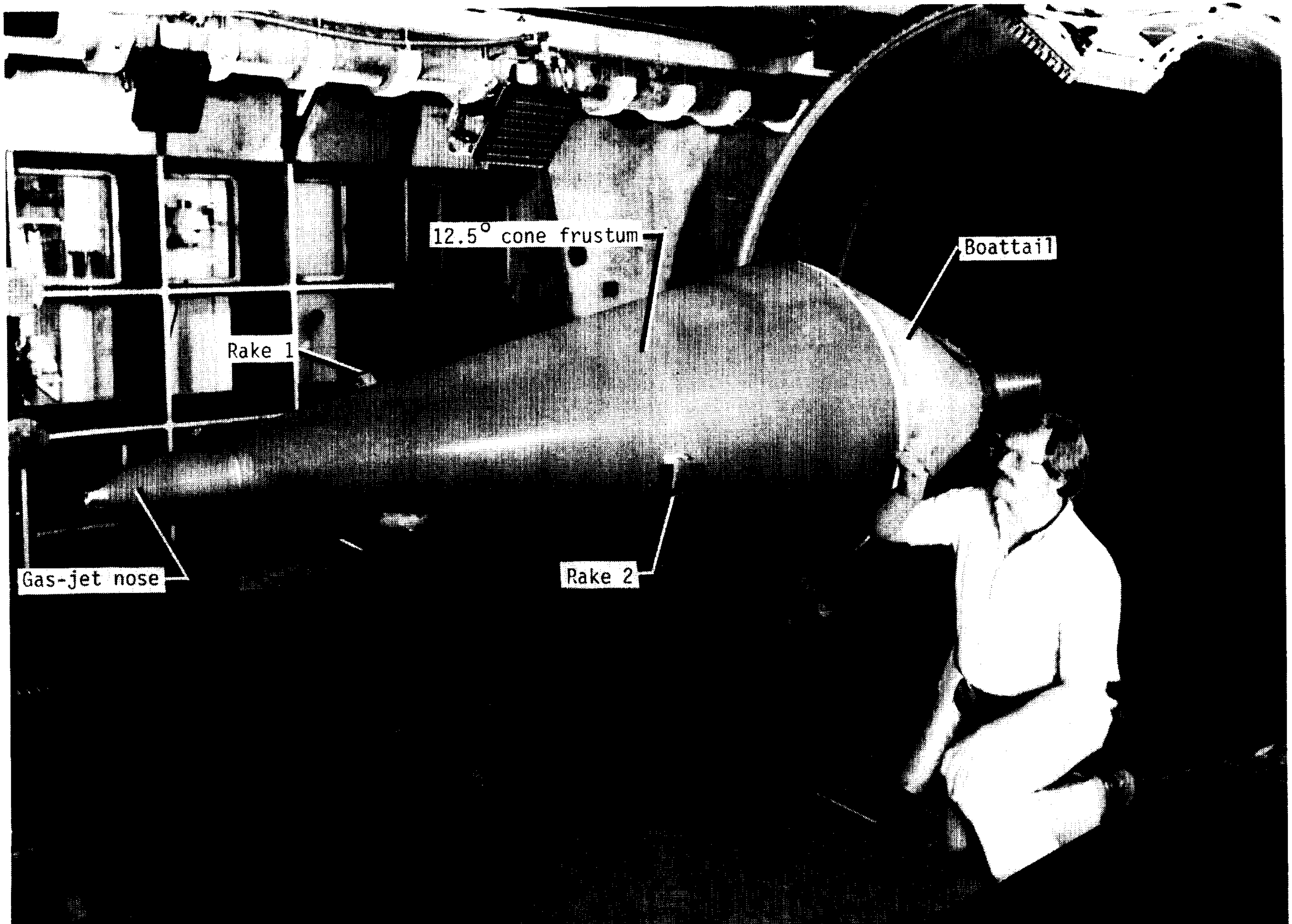

L-88-56

Figure 1. Model in Langley 8-Foot High-Temperature Tunnel.

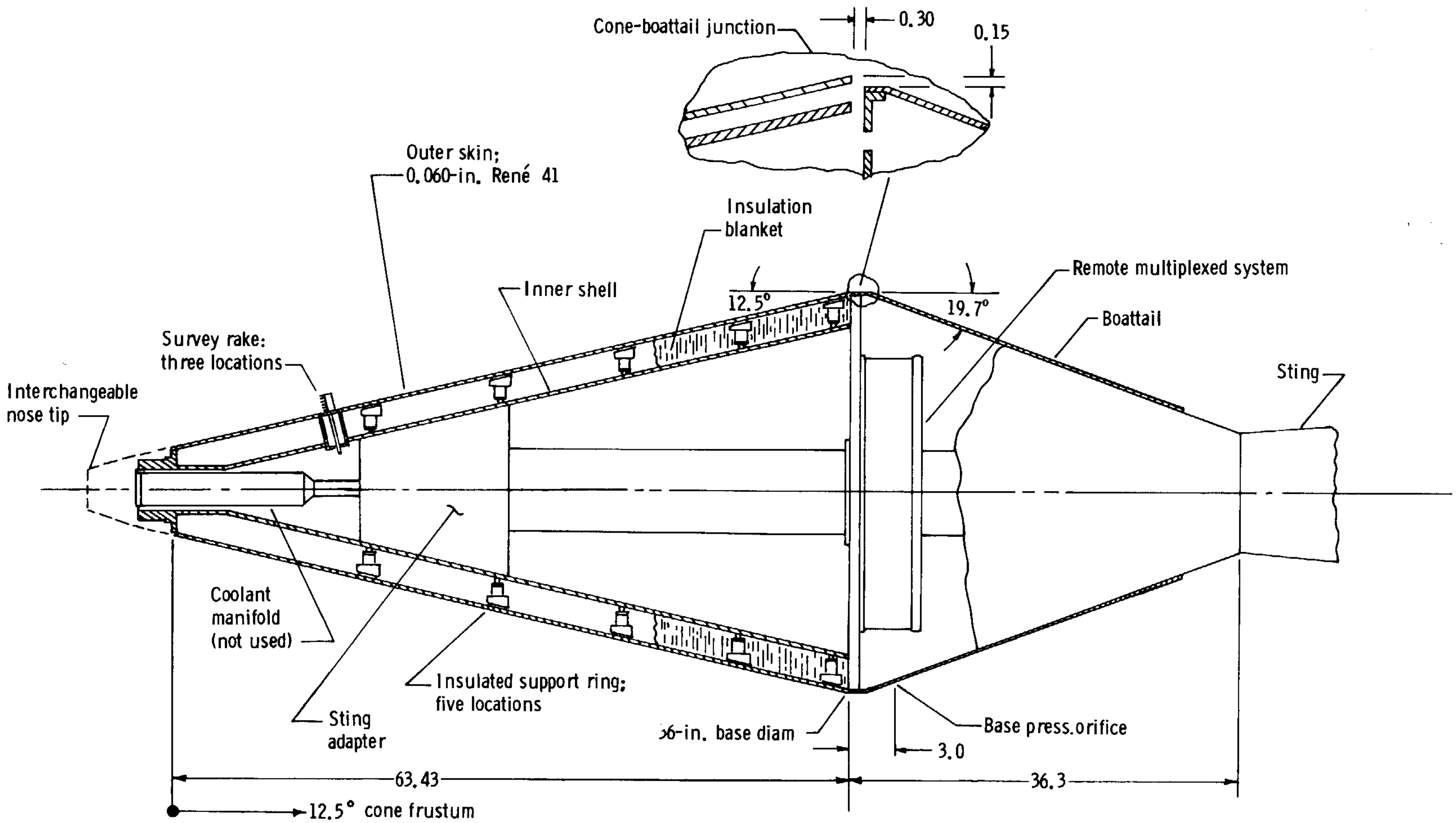

Figure 2. Schematic drawing of model assembly. Linear dimensions are given in inches.

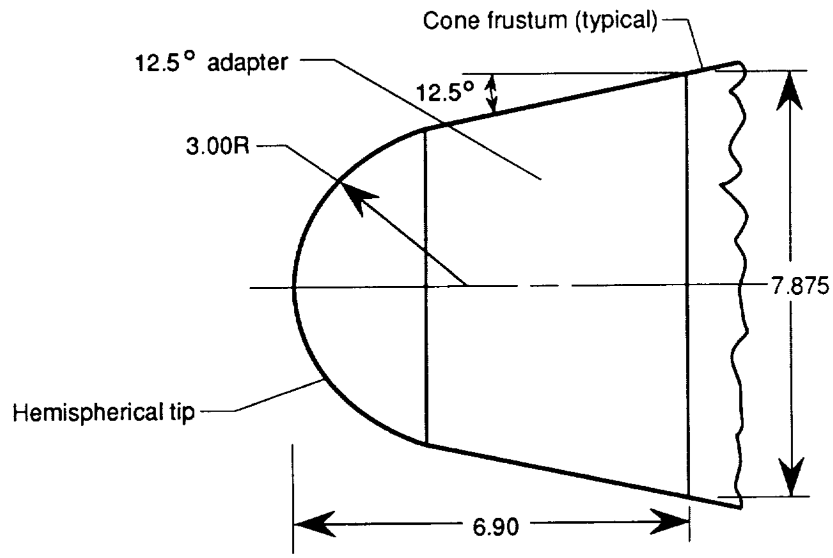

(a) Nose R-3, 3-in-radius tip on 12.5° cone frustum.

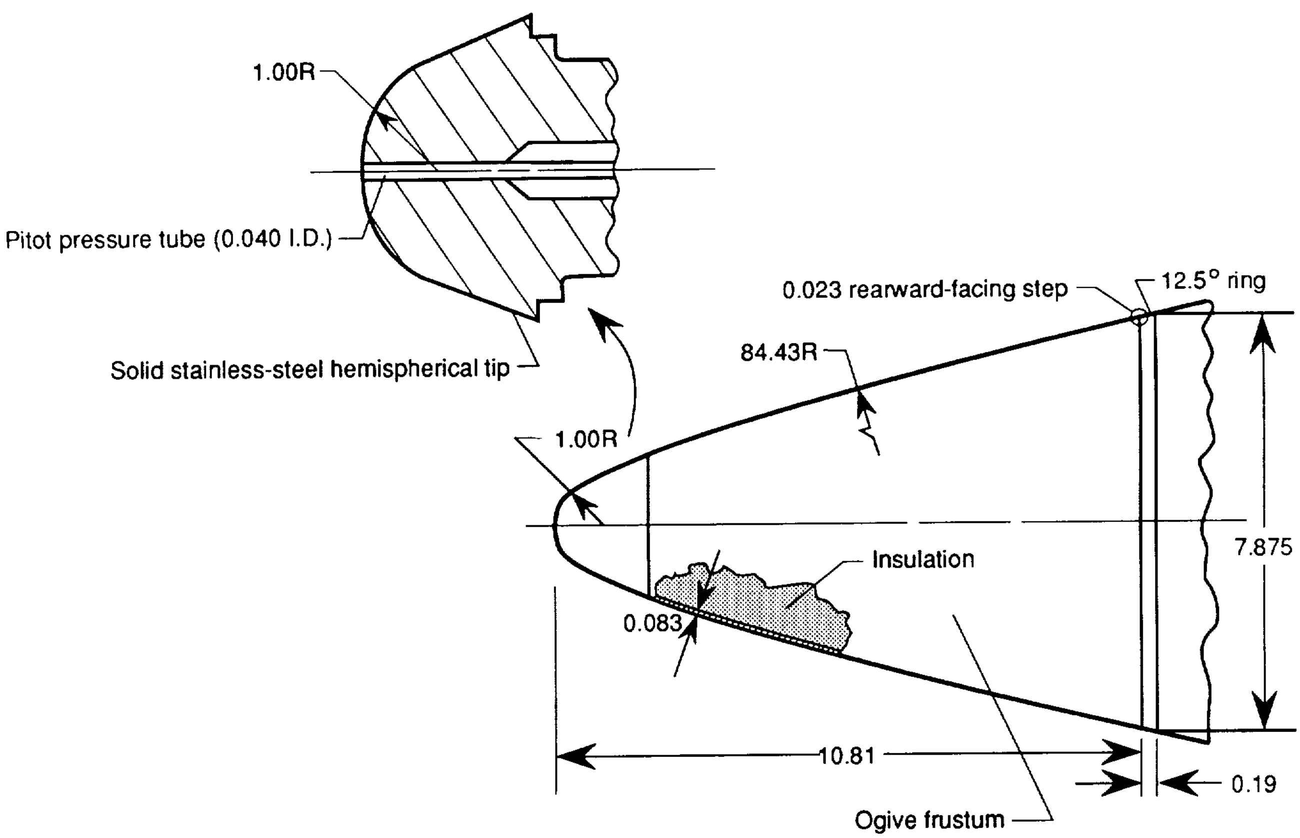

(b) Nose R-1, 1-in-radius tip on ogive frustum.

Figure 3. Baseline nose shapes for attachment to 12.5° cone frustum. Linear dimensions are in inches.

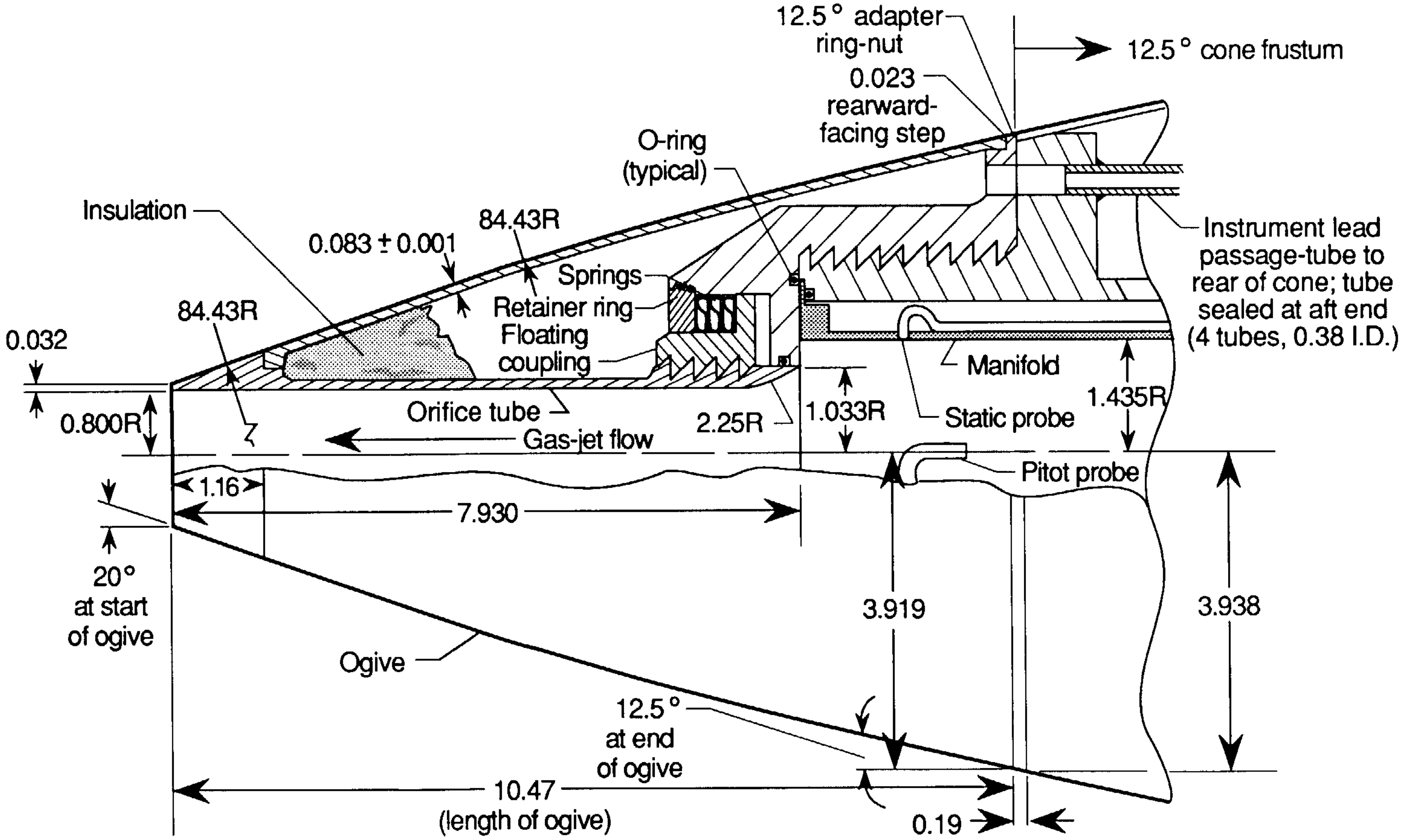

Figure 4. Schematic drawing of gas-jet nose. Linear dimensions are in inches.

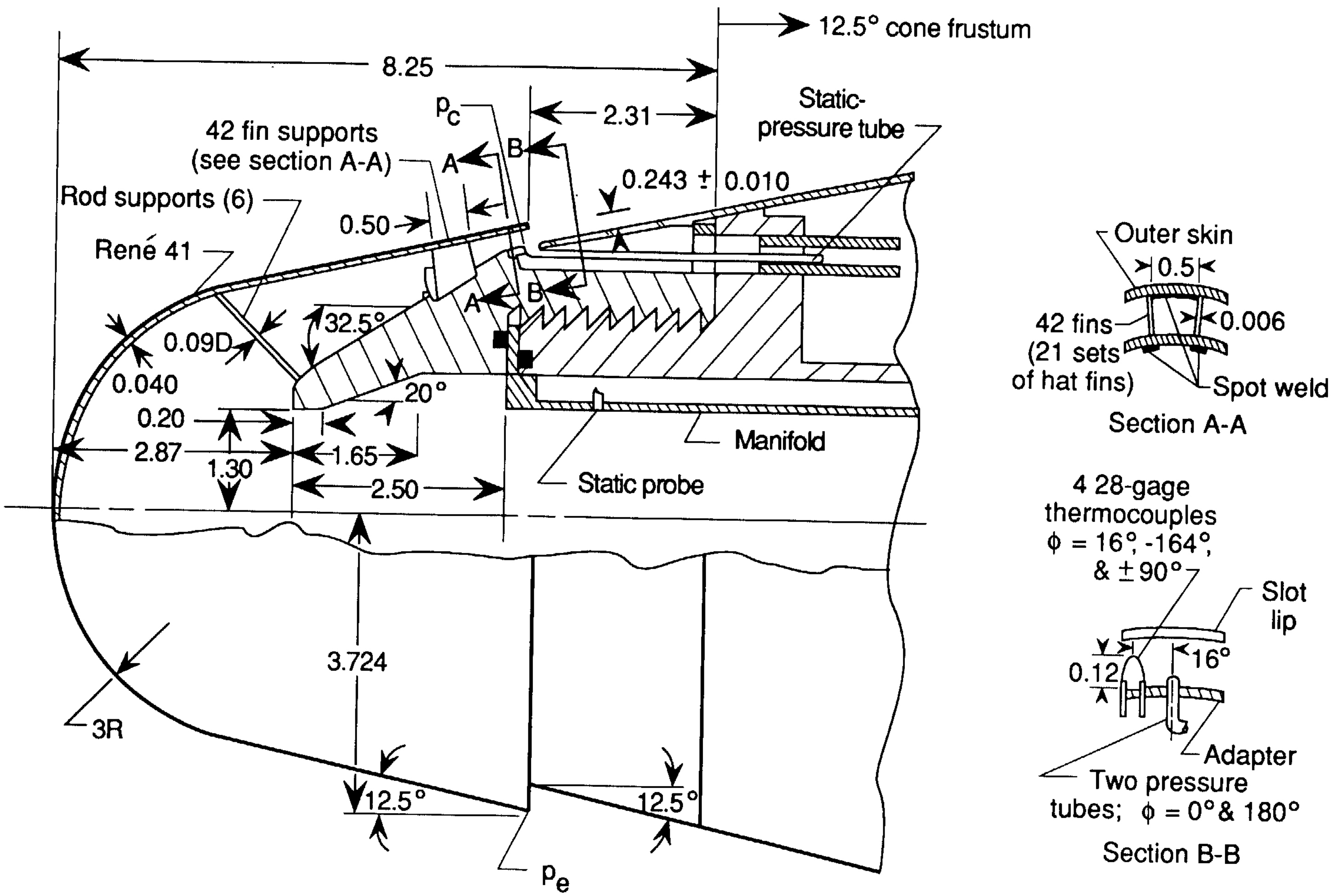

Figure 5. Schematic drawing of tangent-slot nose. Linear dimensions are in inches.

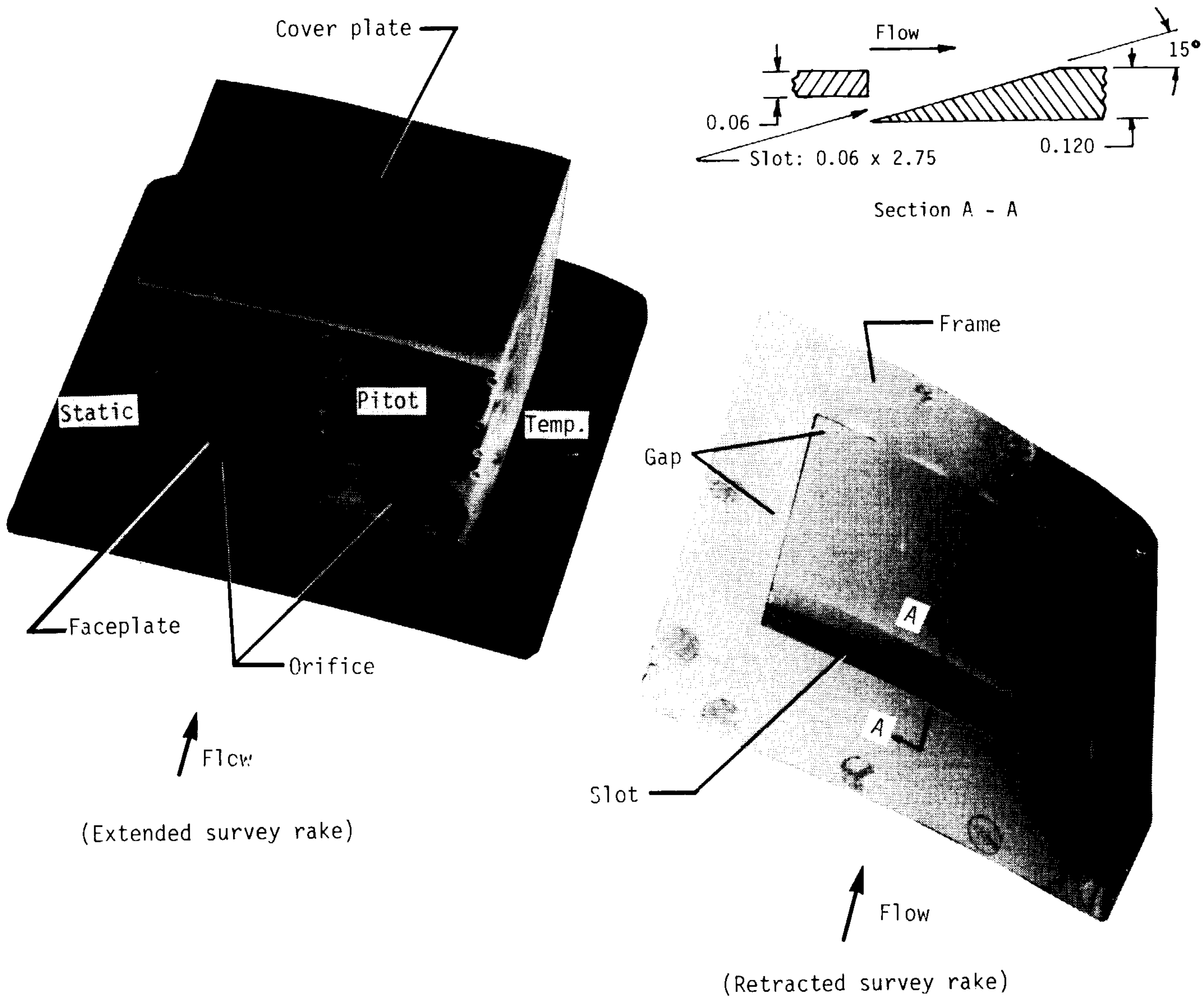

L-88-57

(a) Photographs of shock flow-field survey rake. Linear dimensions are in inches.

Figure 6. Flow-field survey rake.

Rake location		
No.	s_a/L	ϕ,deg
1	0.40	-45
2	0.68	+90
3	0.92	-135

(s_a/L measured to orifice reference line)

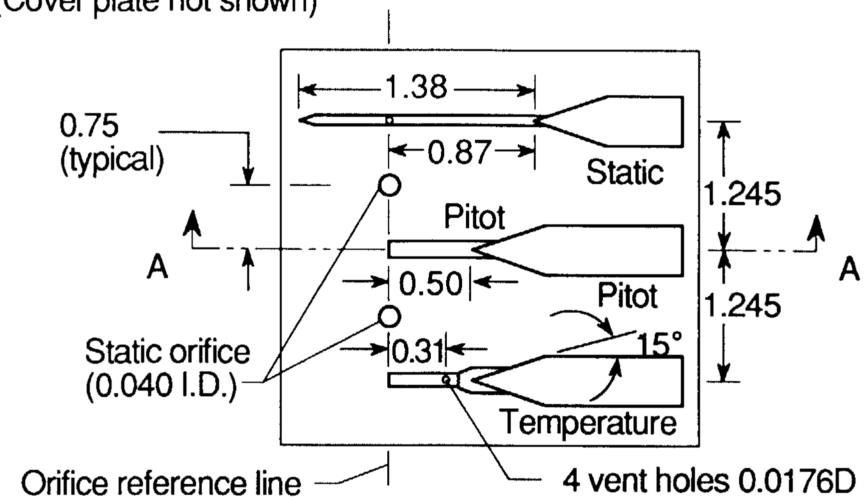

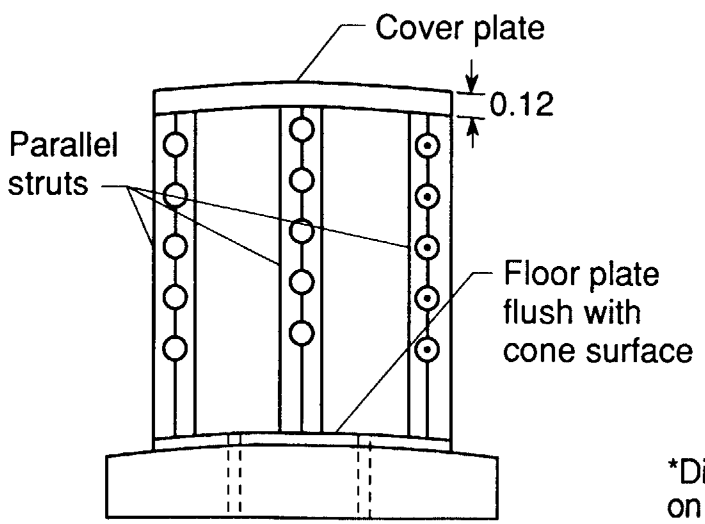

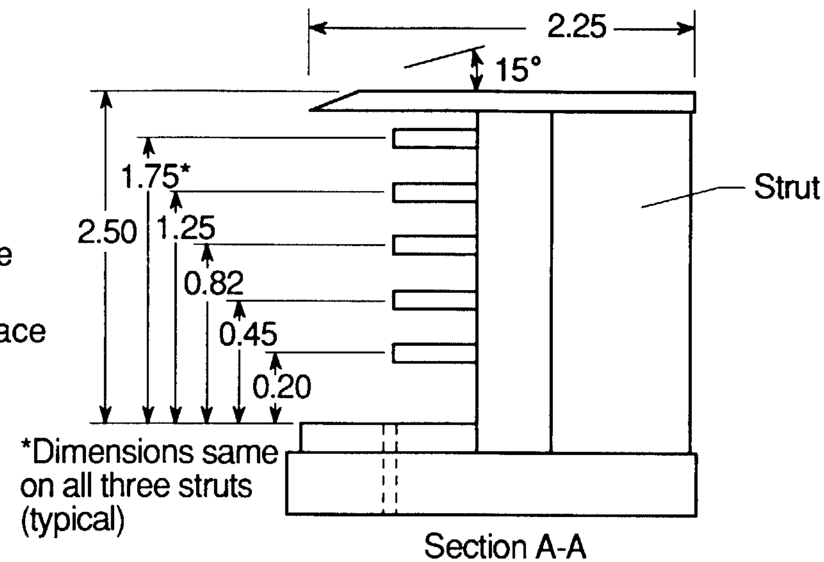

(b) Assembly of flow-field survey rake. Linear dimensions are in inches.

Figure 6. Concluded.

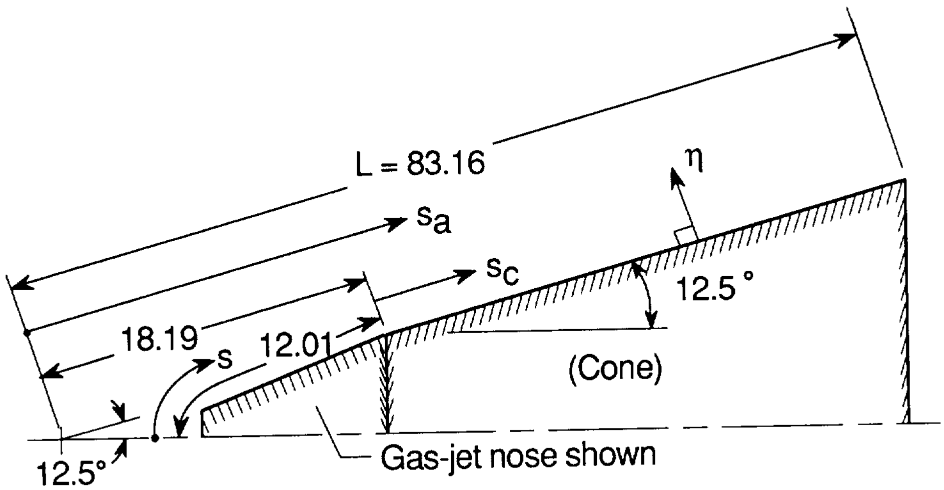

For gas-jet nose, surface distance to cone, including orifice end, is 12.01 in. Thus,

$s_a = 18.19 - 12.01 + s$

	s_a/L
12.5° cone-frustum split line	0.219
Nose R-3 stagnation point	0.114
Nose R-1 stagnation point	0.074
Tangent-slot stagnation point	0.097
Tangent-slot slot exit plane	0.190
Gas-jet orifice lip	0.084

Figure 7. Coordinate system for 12.5° cone with nose tips. Linear dimensions are in inches.

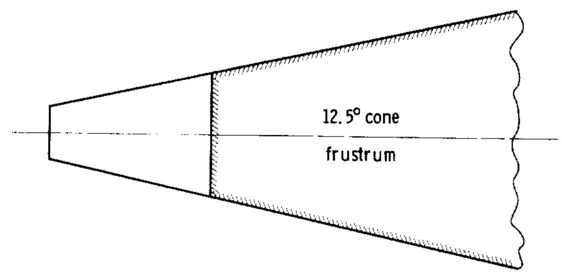

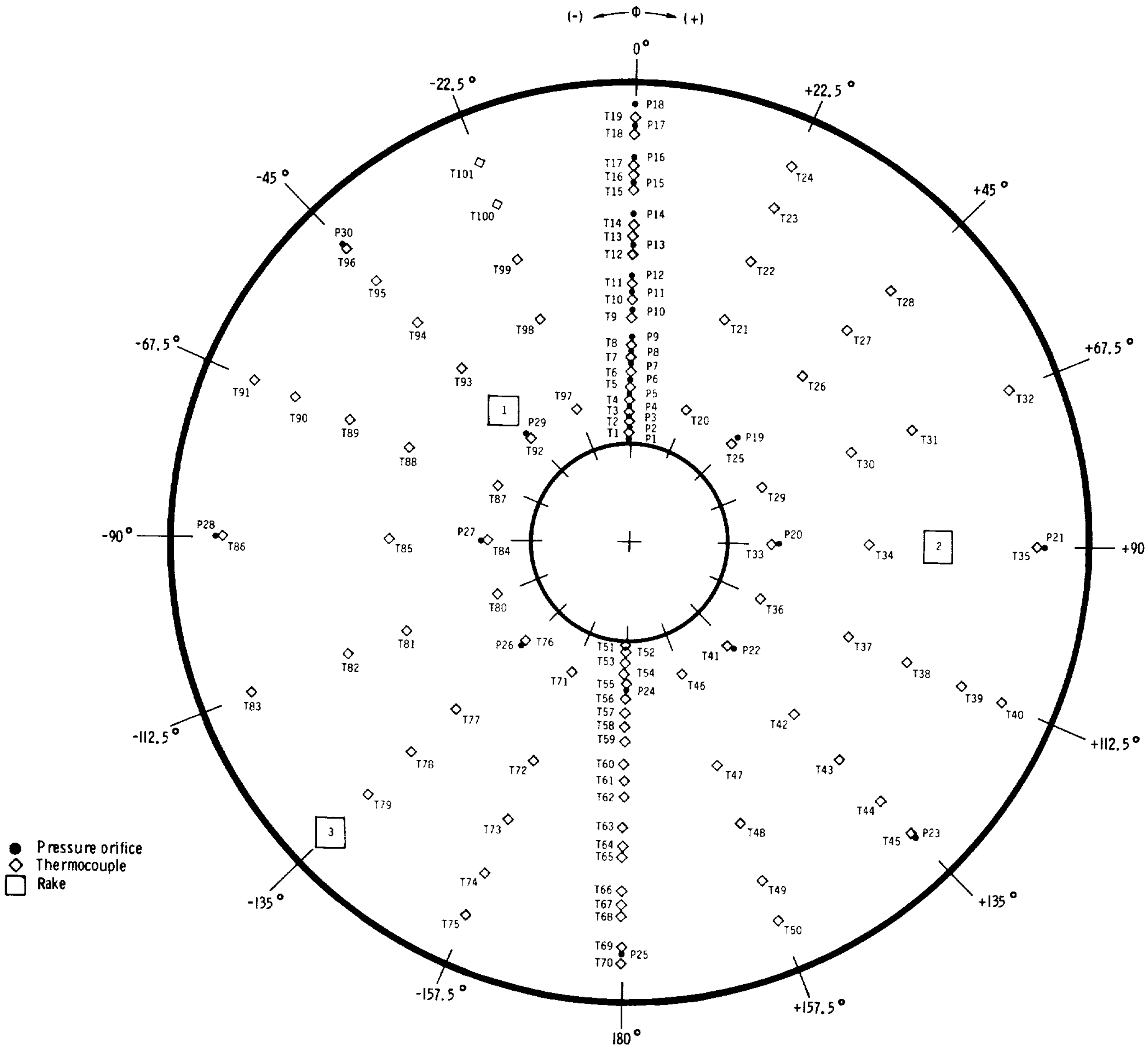

(a) Thermocouple, pressure-orifice, and rake locations on cone frustum; front view.

Figure 8. Instrumentation locations.

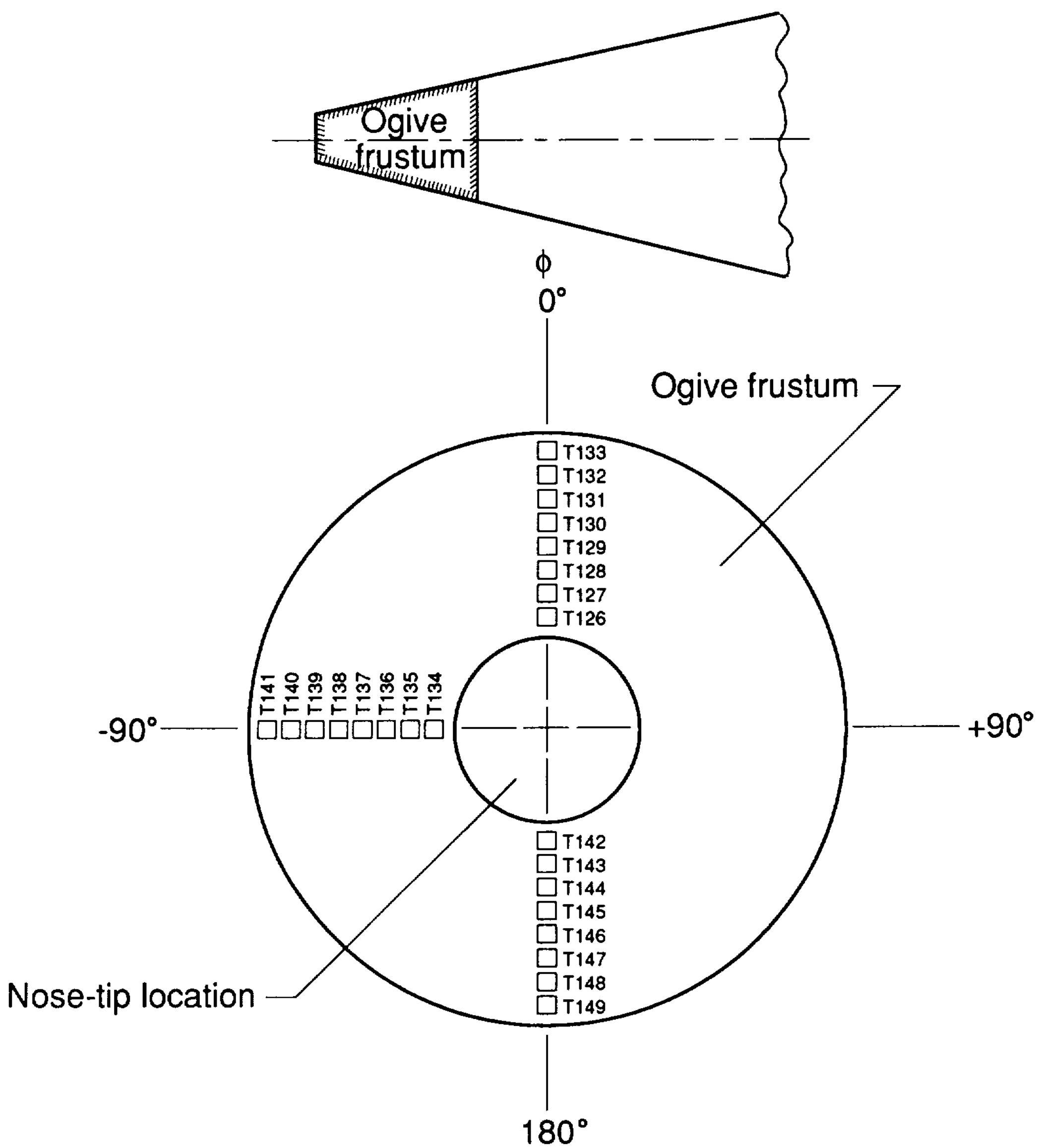

(b) Thermocouple locations on ogive frustum for R-1 and gas-jet noses.

Figure 8. Concluded.

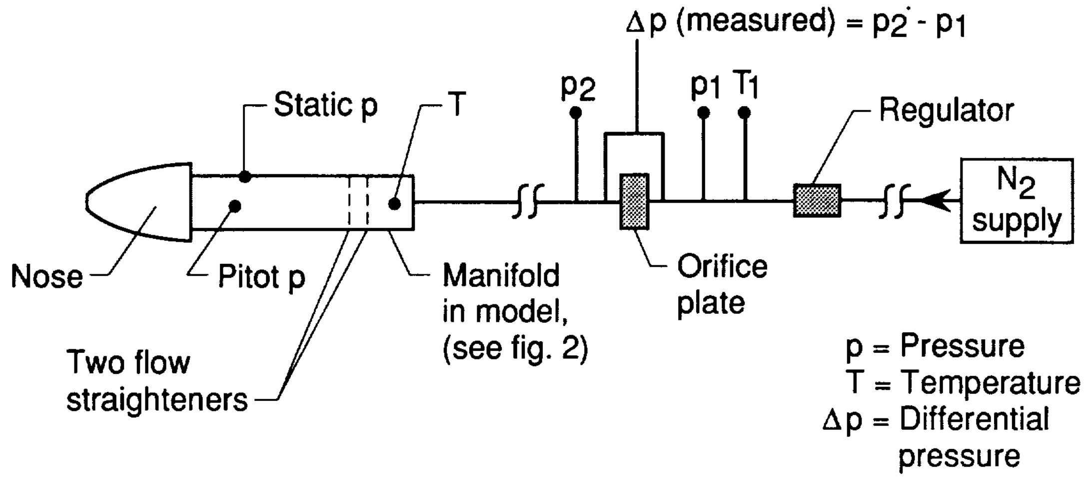

(a) Schematic drawing of flow.

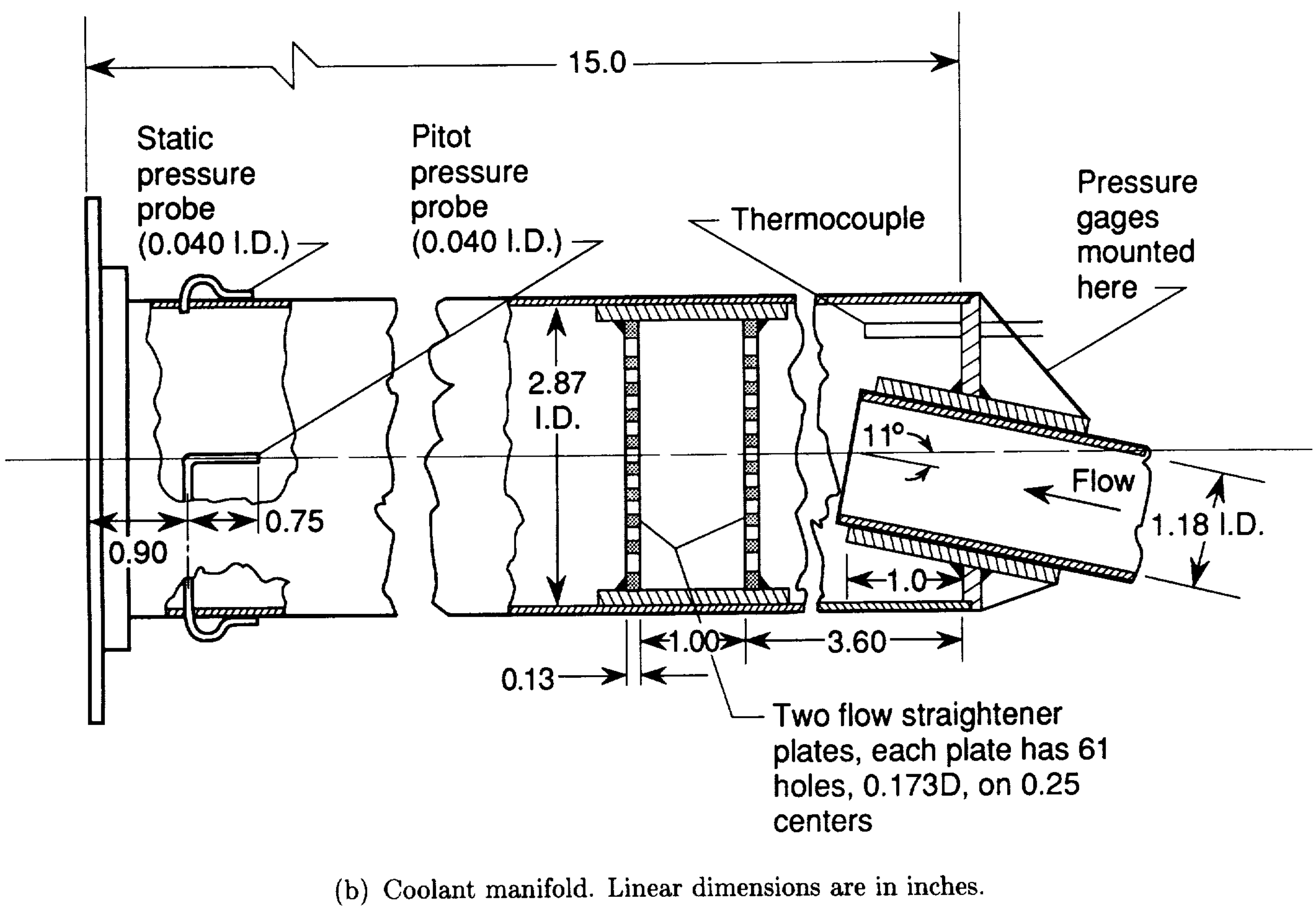

(b) Coolant manifold. Linear dimensions are in inches.

Figure 9. Nitrogen coolant system for gas-jet and tangent-slot noses.

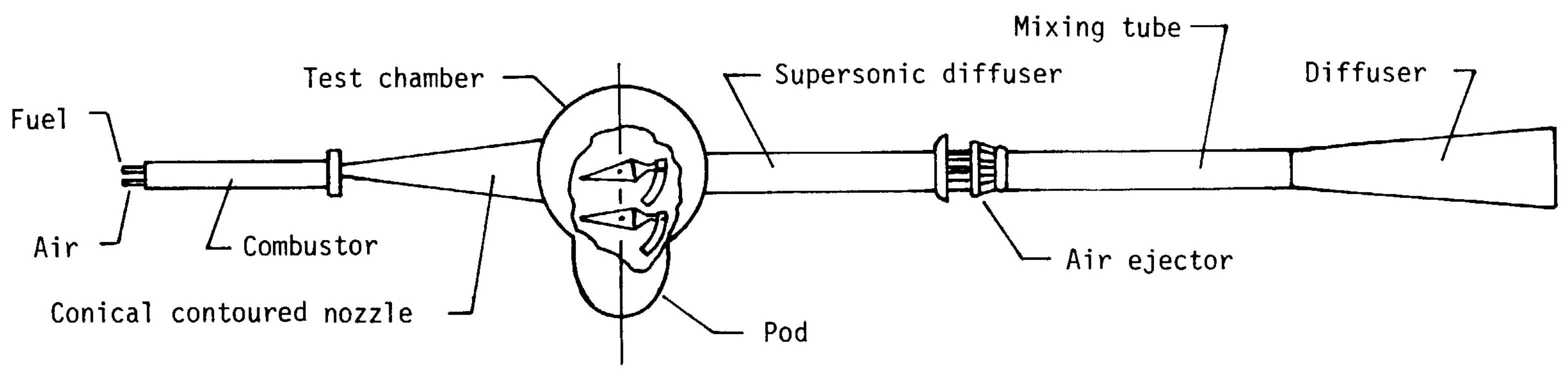

Figure 10. Schematic drawing of Langley 8-Foot High-Temperature Tunnel.

ORIGINAL PAGE
BLACK AND WHITE PHOTOGRAPH

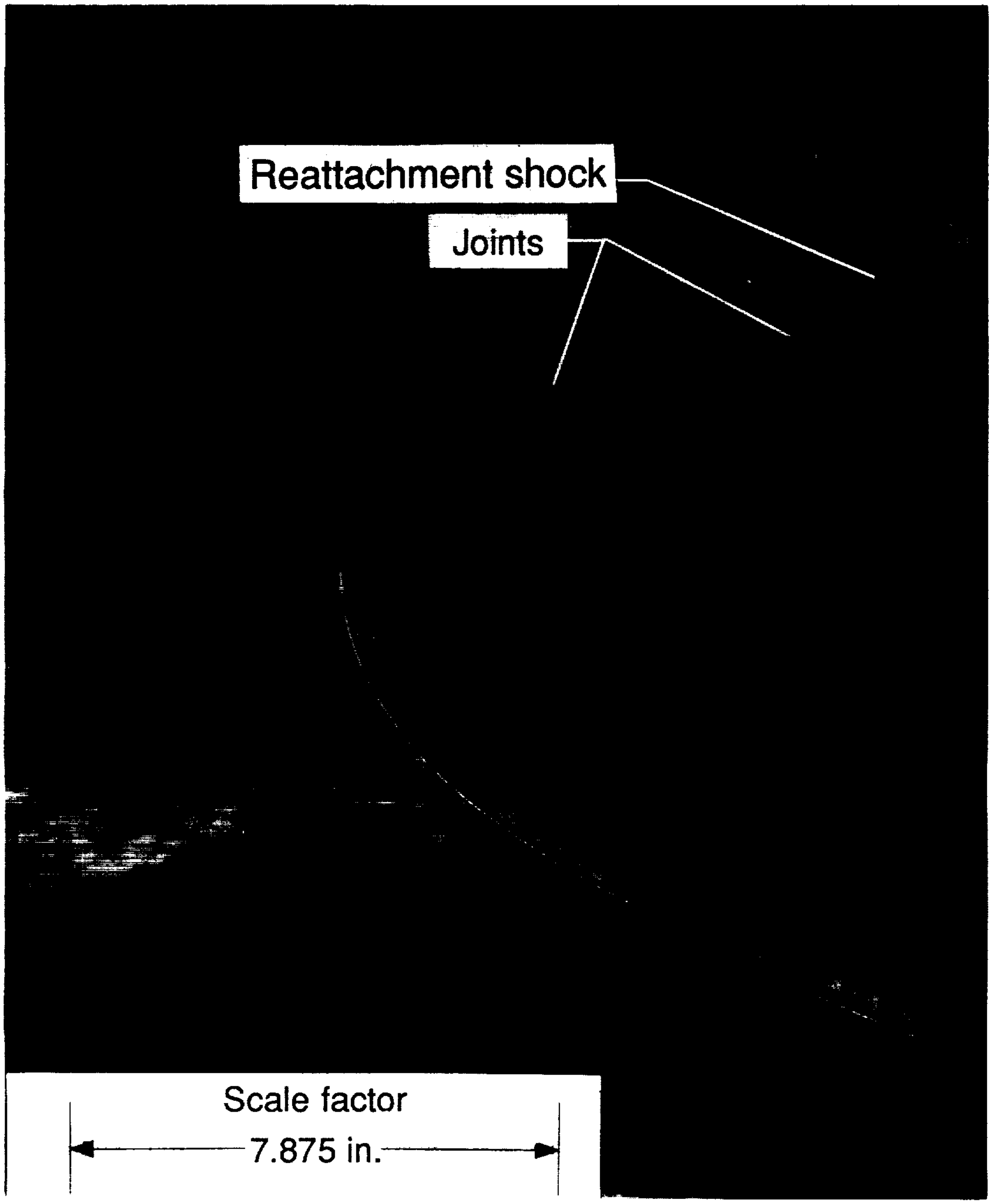

L-88-58

(a) Schlieren of nose R-3, solid uncooled nose with 3-in. radius. Test 98-8.

Figure 11. Representative photographs of shock layer over nose. $\alpha = 0°$.

ORIGINAL PAGE IS
OF POOR QUALITY

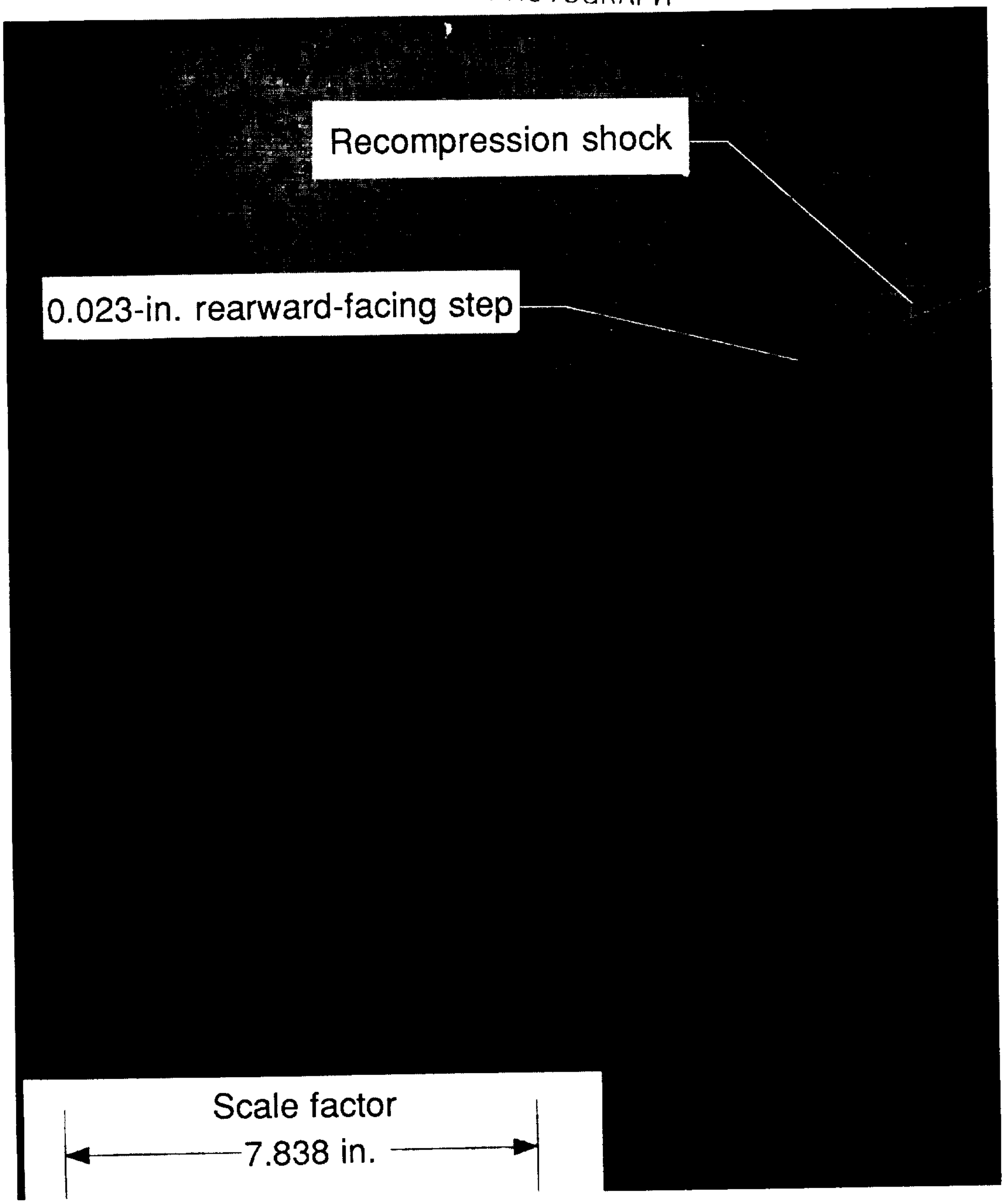

L-88-59

(b) Shadowgraph of nose R-1, solid uncooled nose with 1-in. radius. Test 98-17.

Figure 11. Concluded.

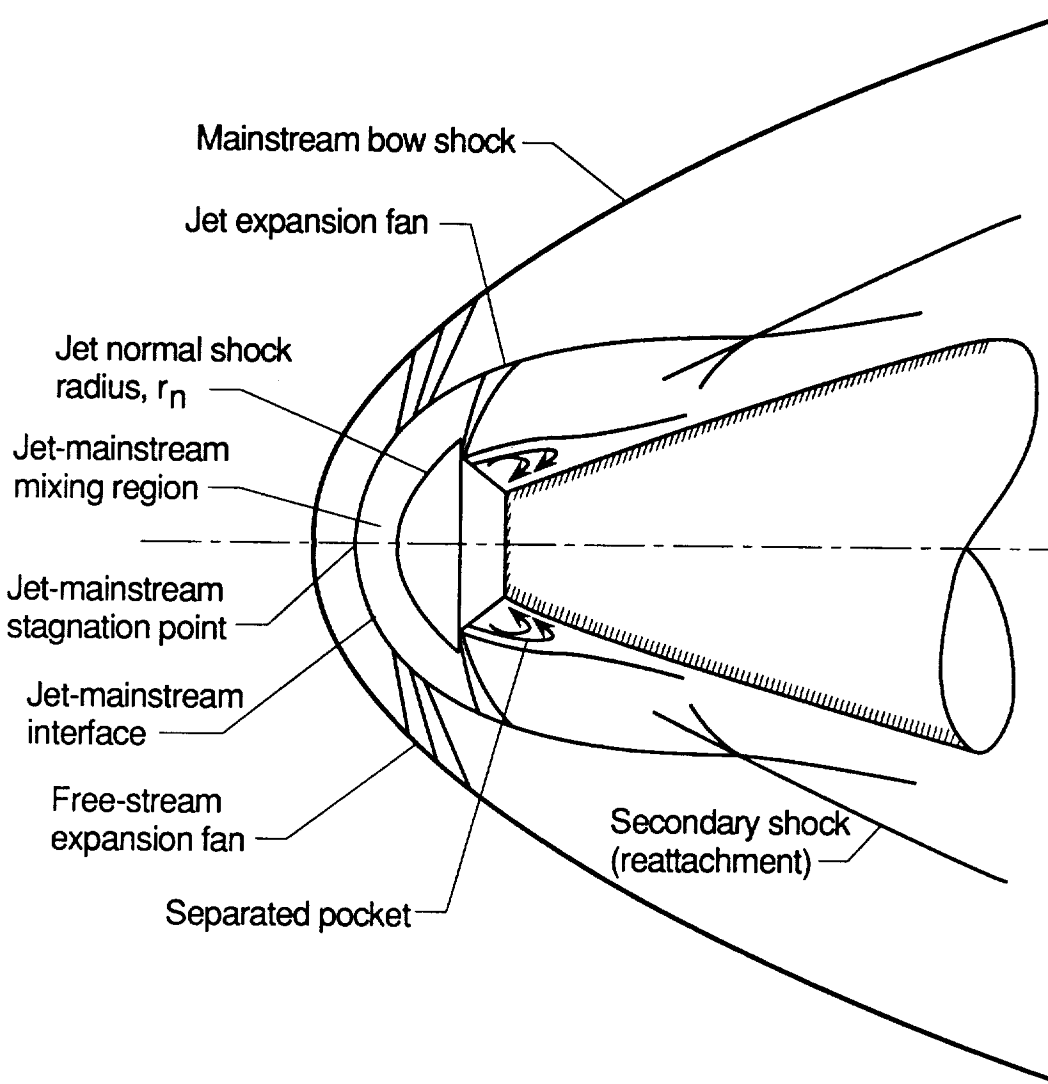

(a) Gas-jet shock schematic (adapted from ref. 17).

Figure 12. Representative shock shapes over nose with coolant.

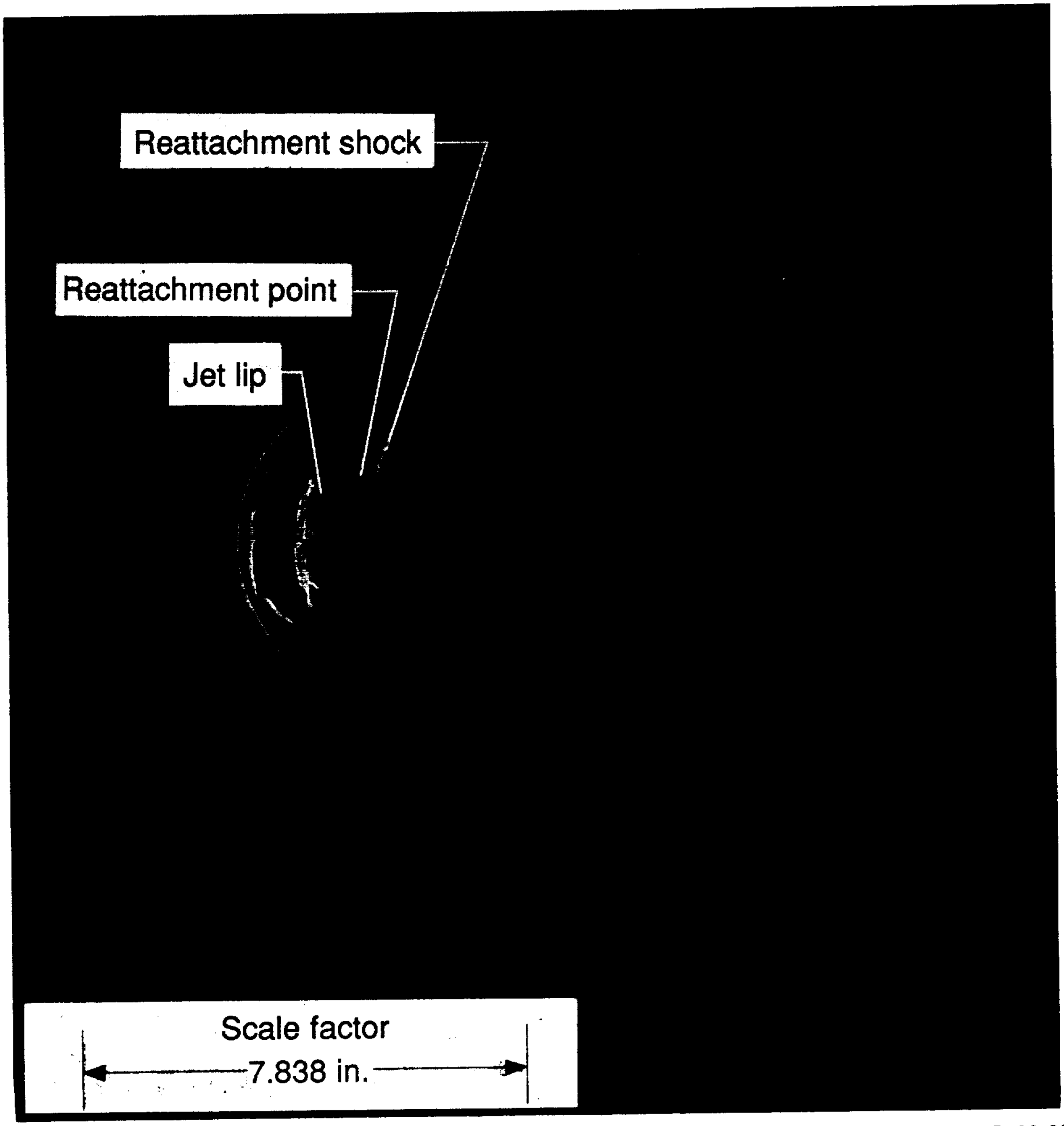

L-88-60

(b) Shadowgraph of supersonic gas-jet nose; $\alpha = 0°$; $\dot{m} = 0.8$ lbm/sec; $p_c/p_{tg} = 1.18$; test 98-43.

Figure 12. Continued.

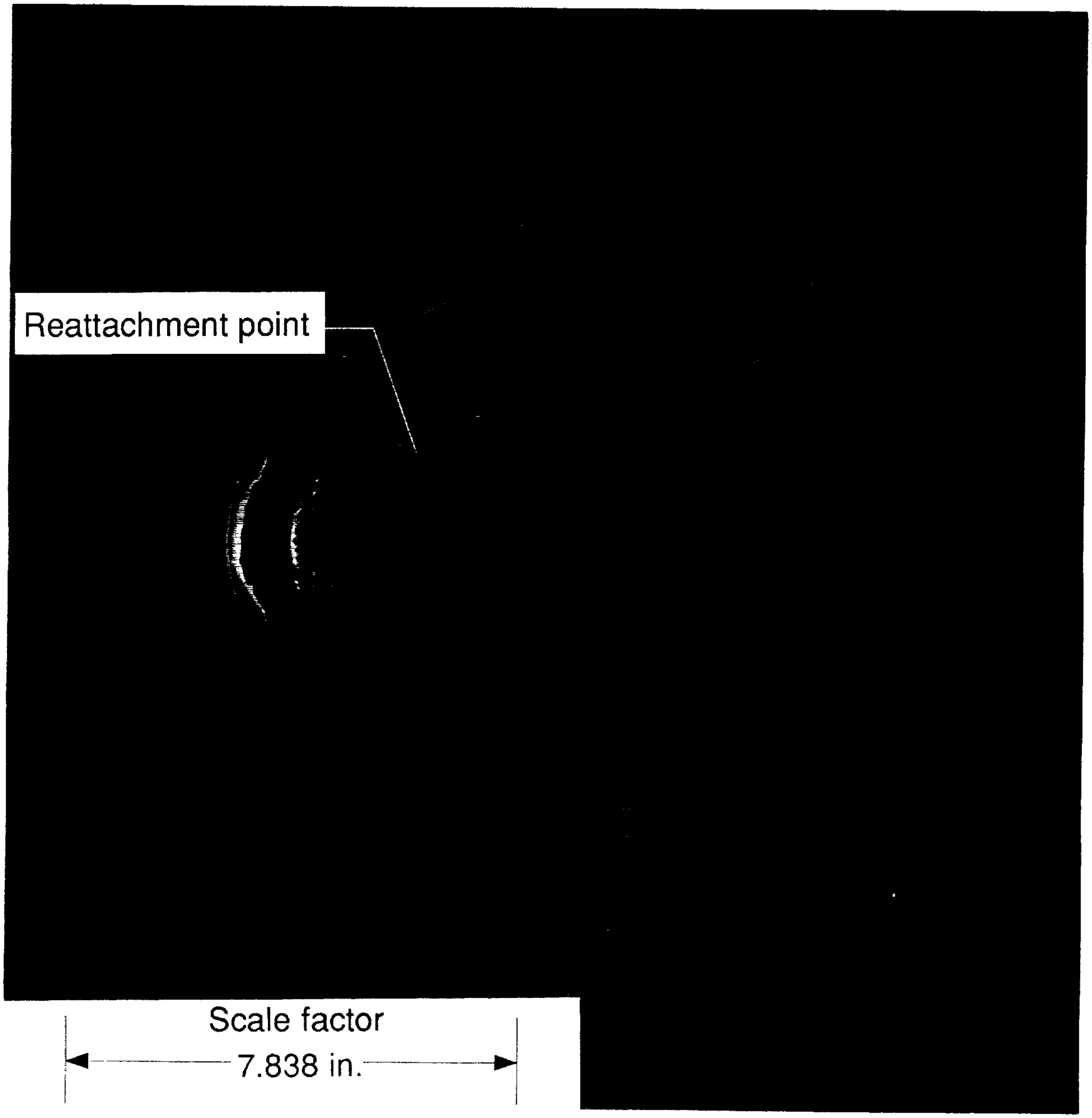

L-88-61

(c) Shadowgraph of supersonic gas-jet nose; $\alpha = 0°$; $\dot{m} = 1.2$ lbm/sec; $p_c/p_{tg} = 1.55$; test 98-33.

Figure 12. Continued.

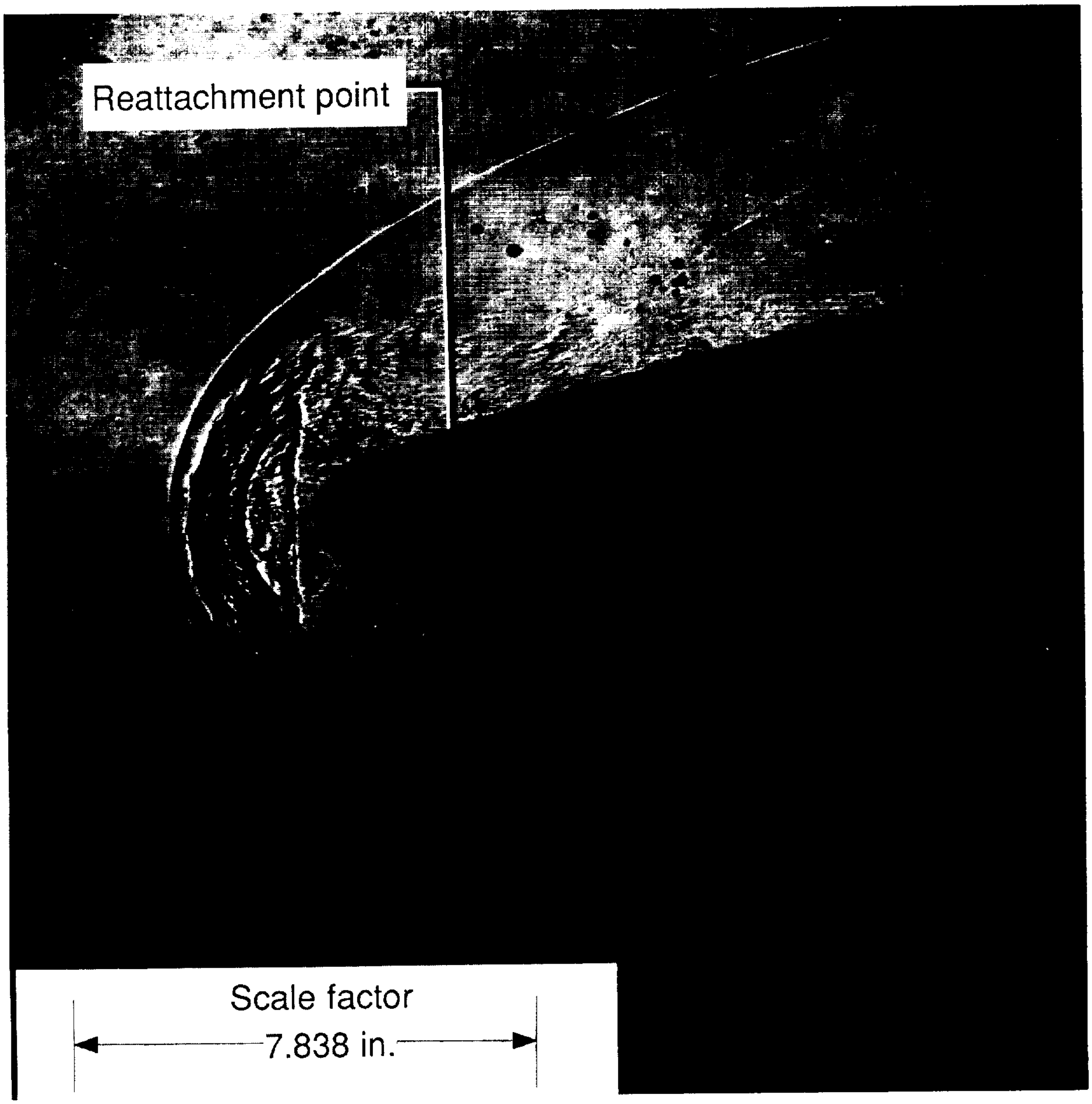

L-88-62

(d) Shadowgraph of supersonic gas-jet nose; $\alpha = 0^\circ$; $\dot{m} = 2.0$ lbm/sec; $p_c/p_{tg} = 2.46$; test 98-40.

Figure 12. Continued.

ORIGINAL PAGE
BLACK AND WHITE PHOTOGRAPH

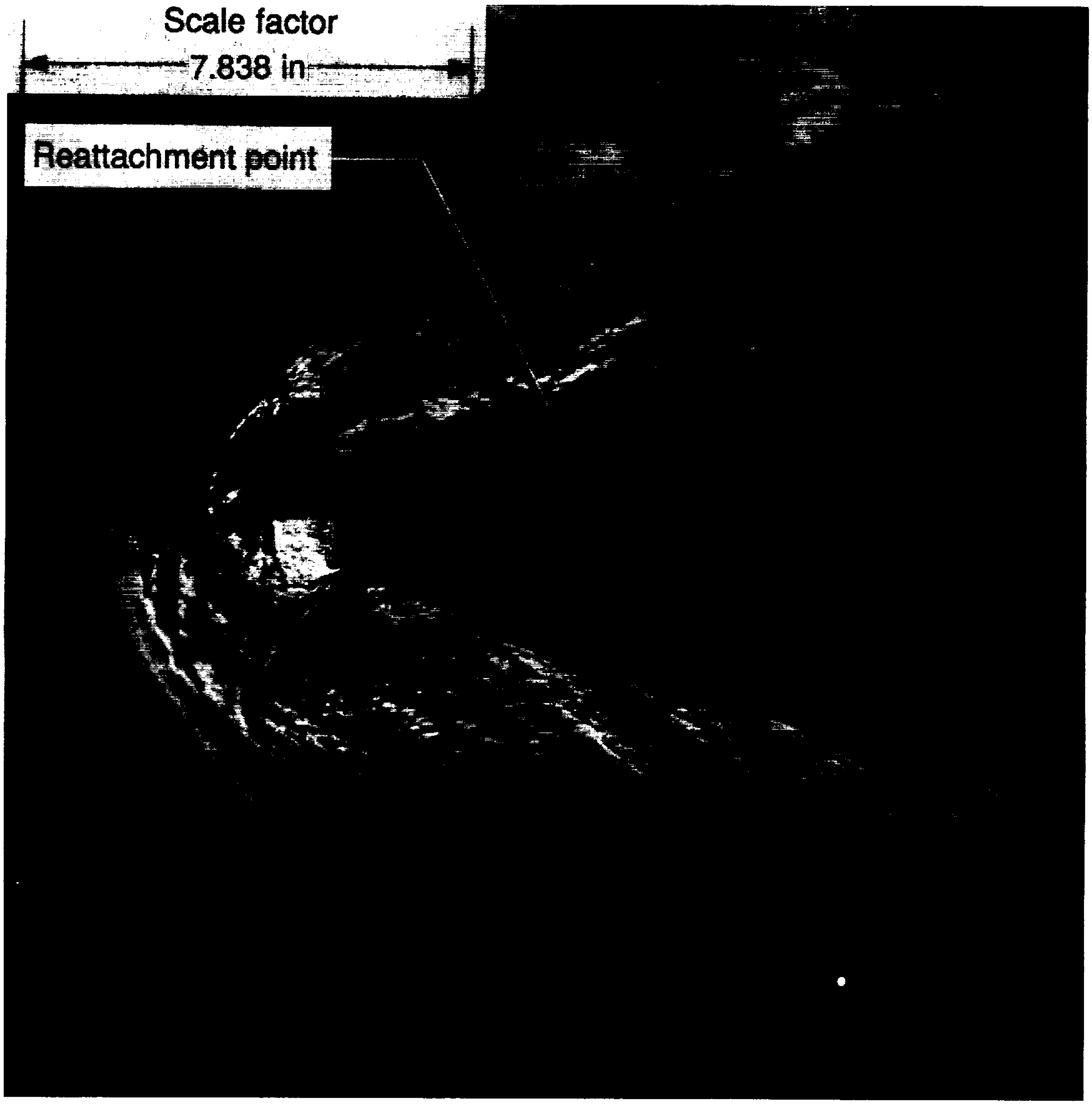

L-88-63

(e) Schlieren of supersonic gas-jet nose; $\alpha = 0°$; $\dot{m} = 4.6$ lbm/sec; $p_c/p_{tg} = 5.05$; test 98-29.

Figure 12. Continued.

ORIGINAL PAGE IS
OF POOR QUALITY

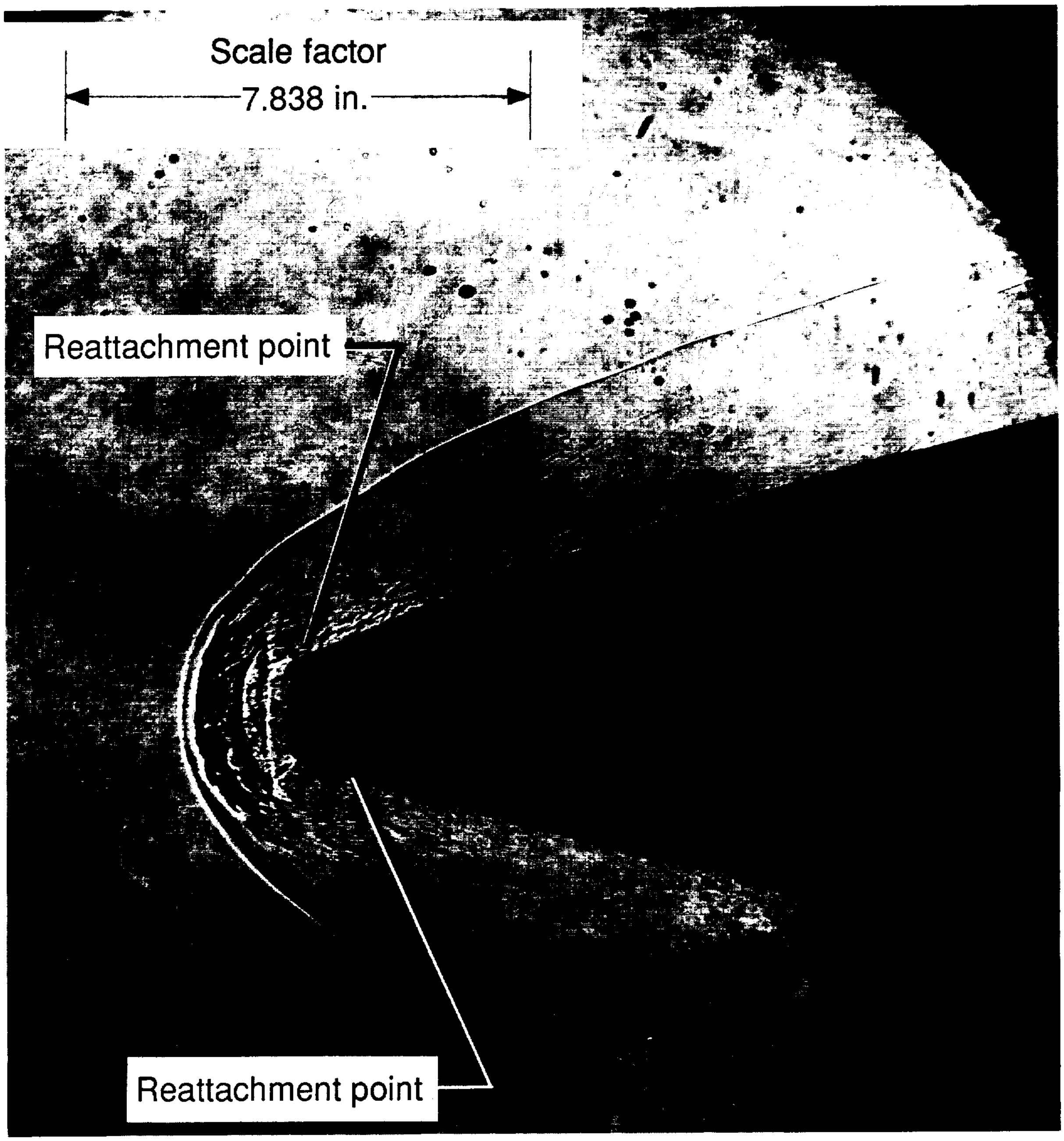

L-88-64

(f) Shadowgraph of supersonic gas-jet nose; $\alpha = 2.5°$; $\dot{m} = 1.2$ lbm/sec; $p_c/p_{tg} = 1.50$; test 98-36.

Figure 12. Continued.

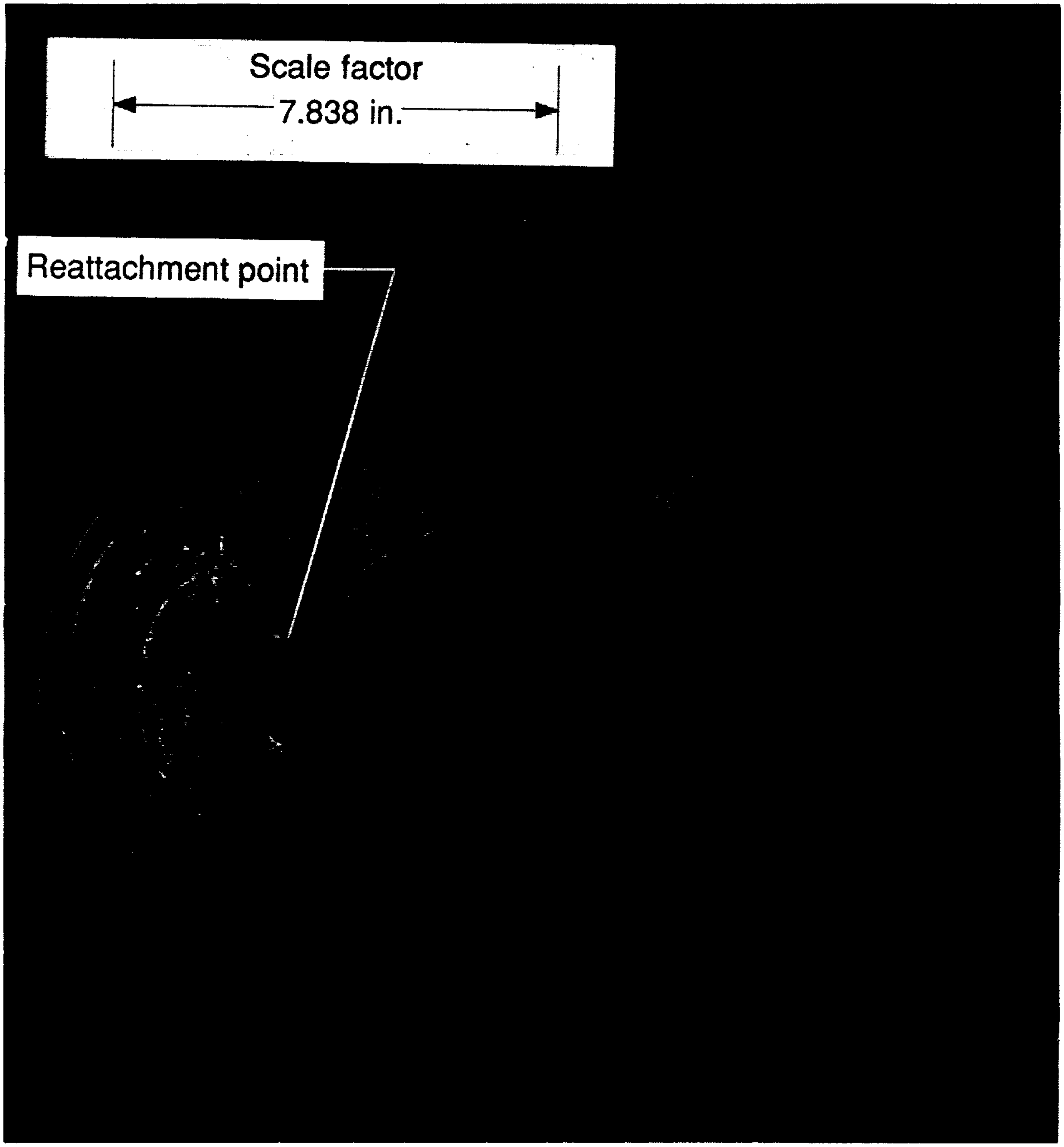

L-88-65

(g) Shadowgraph of supersonic gas-jet nose; $\alpha = 2.5°$; $\dot{m} = 4.4$ lbm/sec; $p_c/p_{tg} = 5.12$; test 98-28.

Figure 12. Continued.

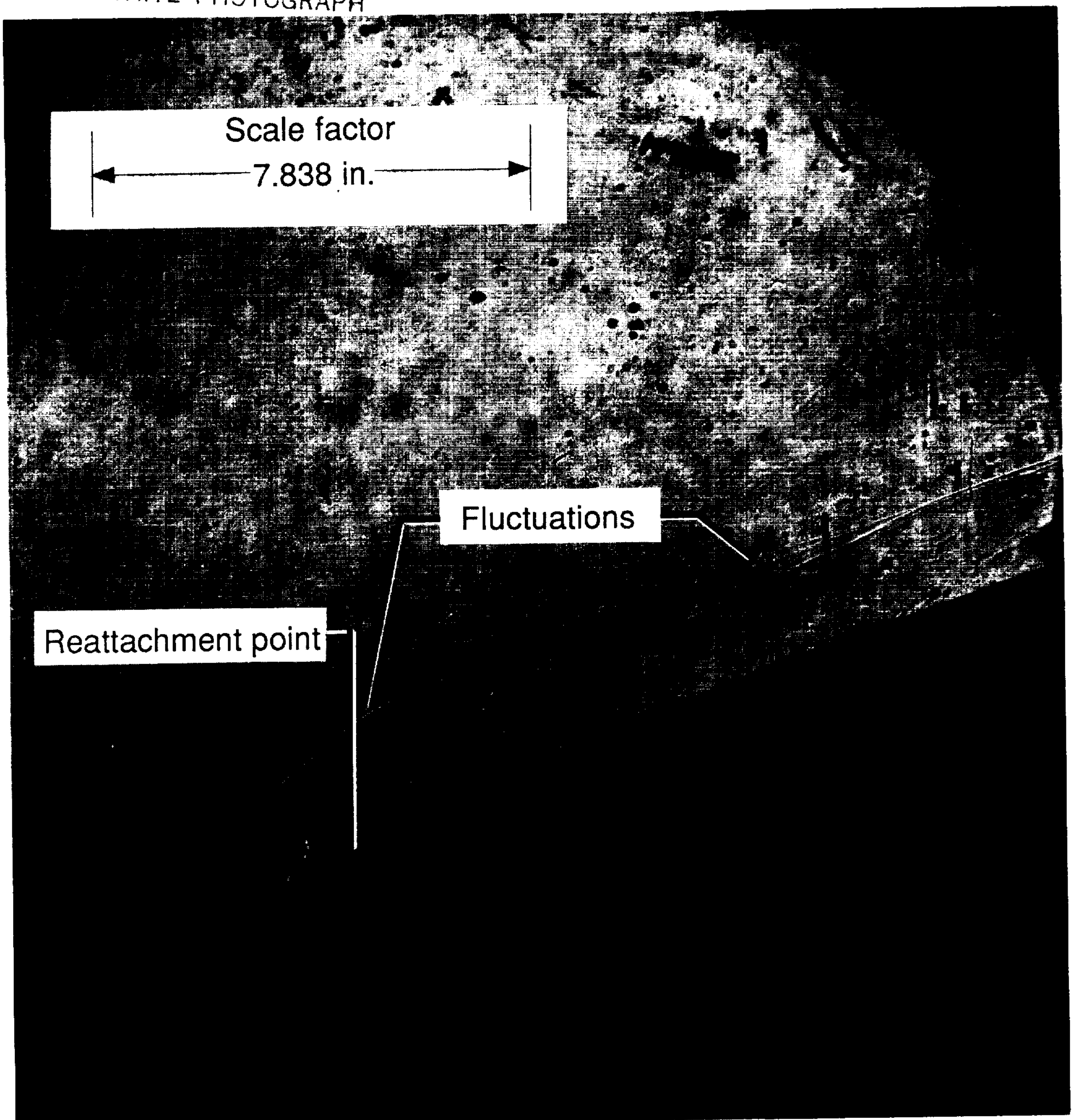

L-88-66

(h) Shadowgraph of supersonic gas-jet nose; $\alpha = 6.0°$; $\dot{m} = 1.2$ lbm/sec; $p_c/p_{tg} = 1.47$; test 98-46.

Figure 12. Continued.

ORIGINAL PAGE
BLACK AND WHITE PHOTOGRAPH

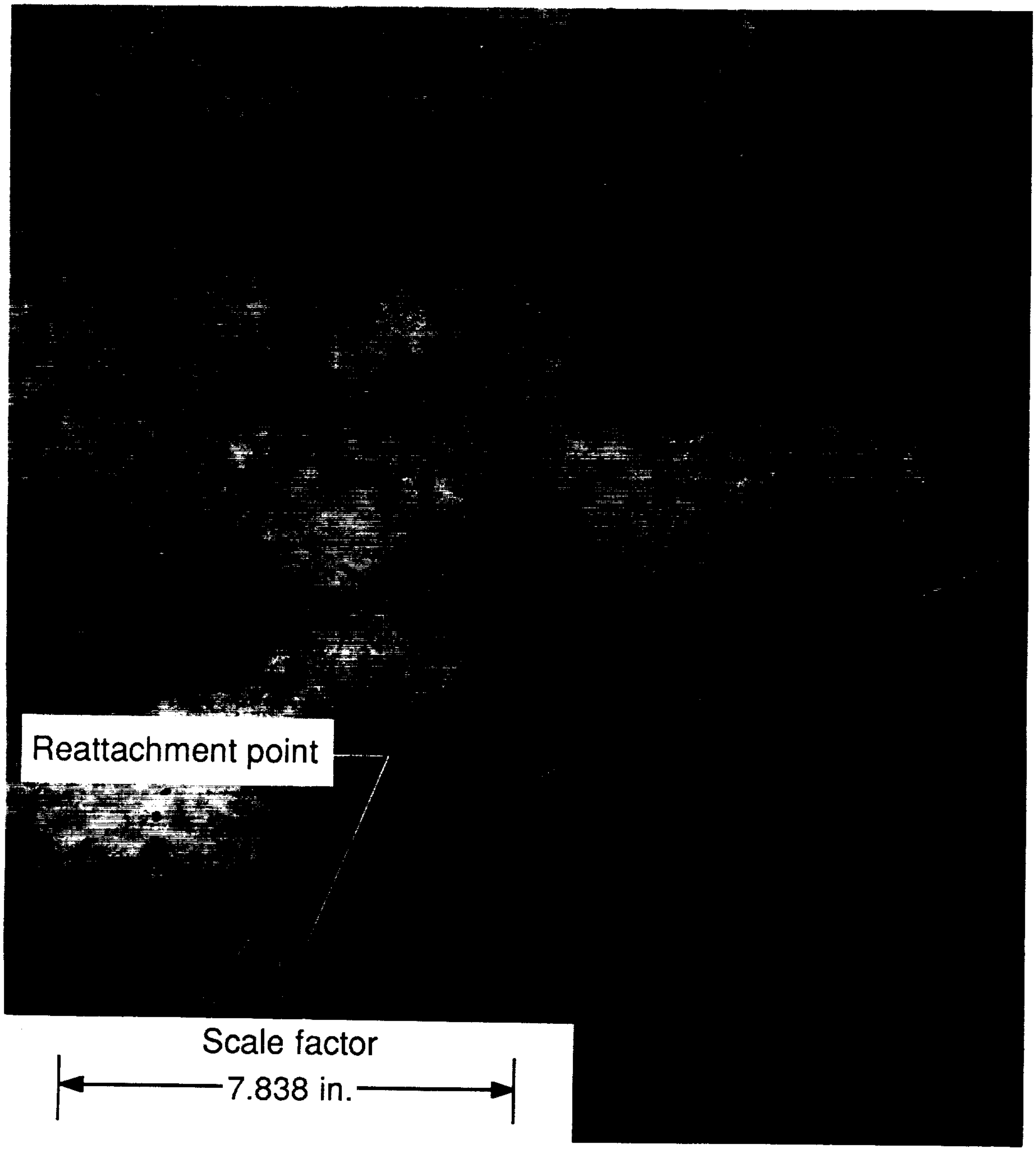

L-88-67

(i) Shadowgraph of supersonic gas-jet nose; $\alpha = 10.0°$; $\dot{m} = 1.2$ lbm/sec; $p_c/p_{tg} = 1.46$; test 98-37.

Figure 12. Continued.

ORIGINAL PAGE IS
OF POOR QUALITY

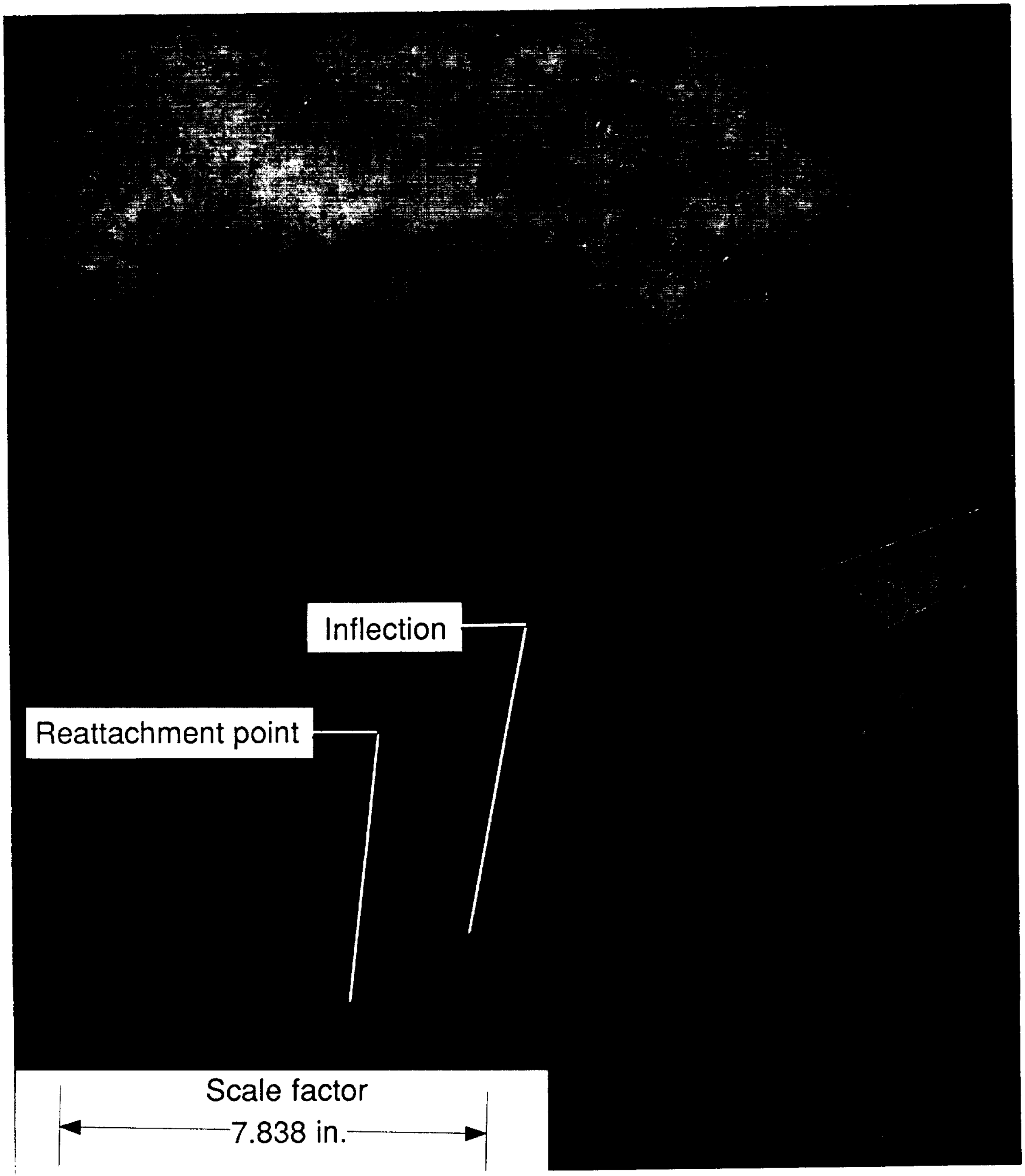

L-88-68

(j) Shadowgraph of supersonic gas-jet nose; $\alpha = 10.0°$; $\dot{m} = 3.8$ lbm/sec; $p_c/p_{tg} = 4.34$; test 98-31.

Figure 12. Continued.

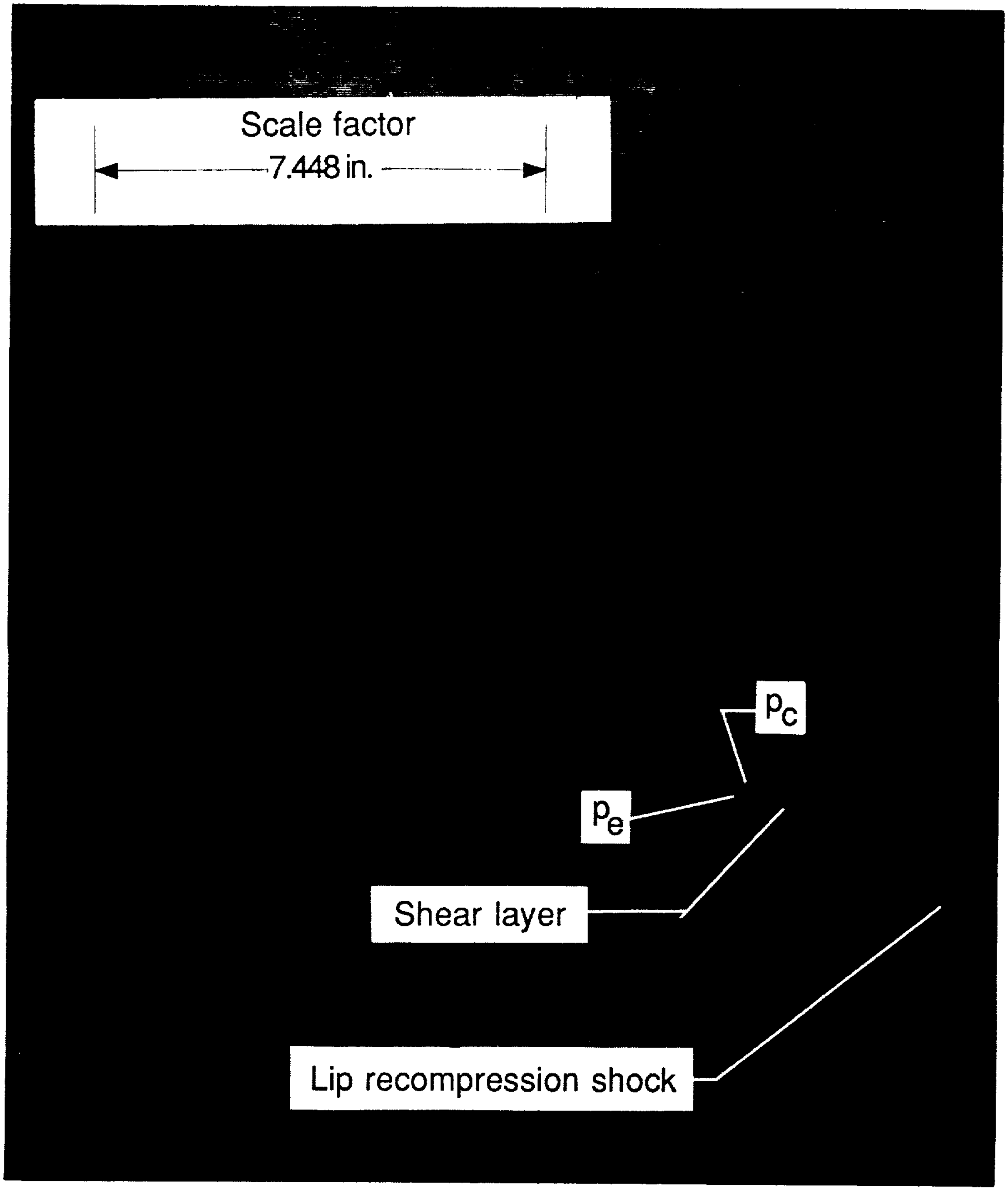

L-88-69

(k) Shadowgraph of tangent-slot nose; $\alpha = 0°$; $\dot{m} = 0.3$ lbm/sec; $p_c/p_e = 0.99$; test 98-55.

Figure 12. Continued.

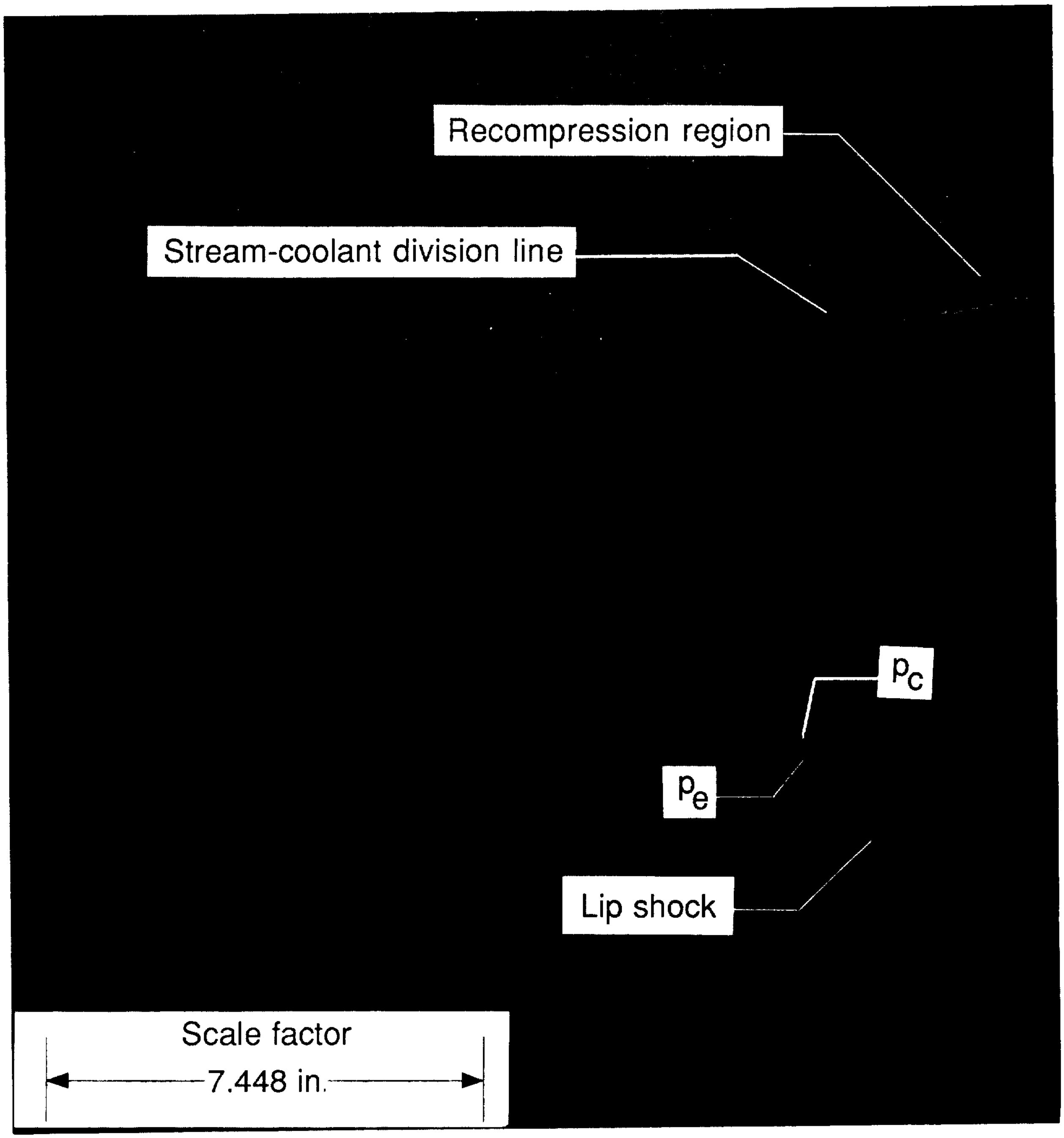

L-88-70

(l) Shadowgraph of tangent-slot nose; $\alpha = 0°$; $\dot{m} = 2.7$ lbm/sec; $p_c/p_e = 6.79$; test 98-57.

Figure 12. Concluded.

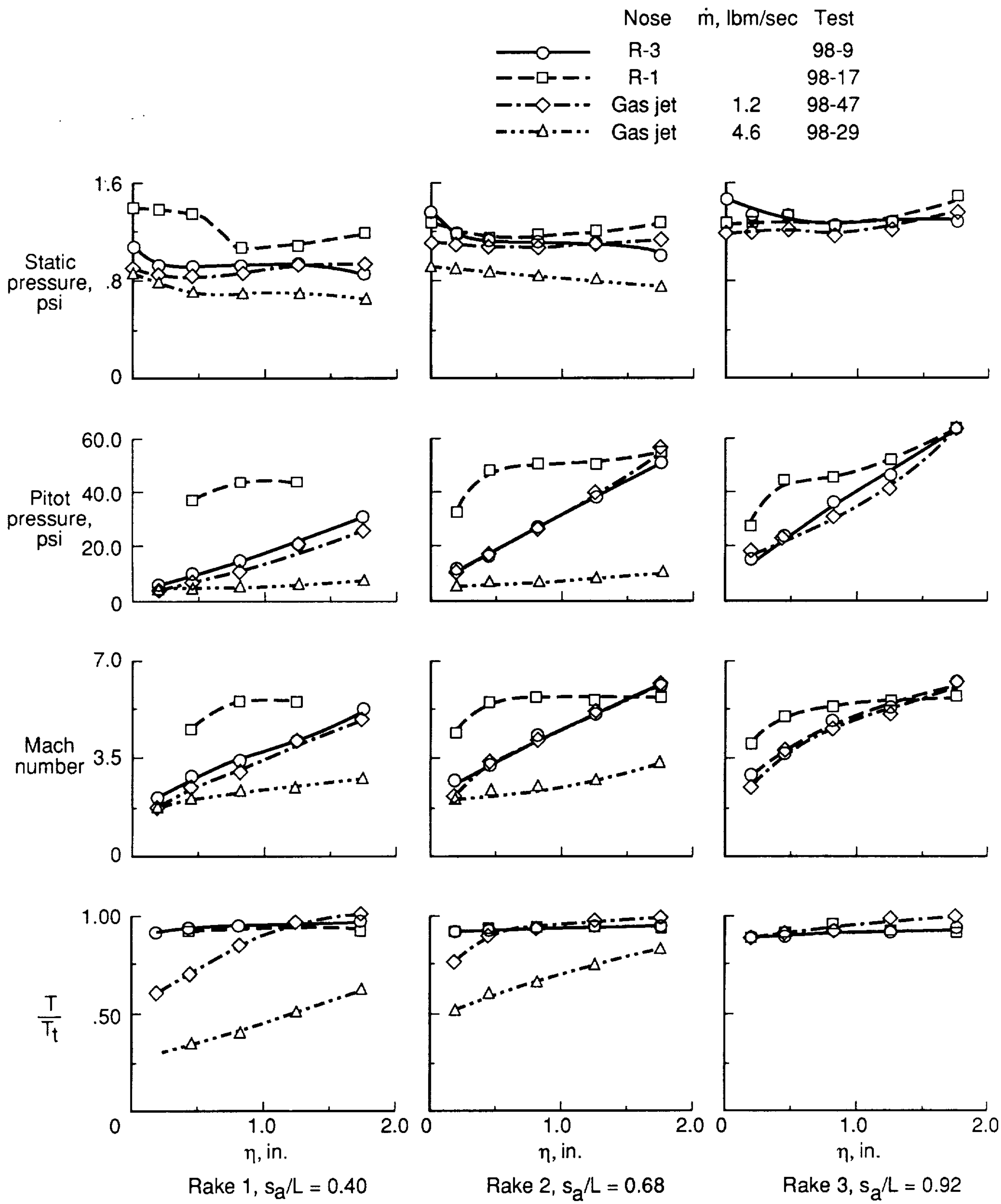

Figure 13. Shock-layer profiles for gas-jet, R-1, and R-3 nose models.

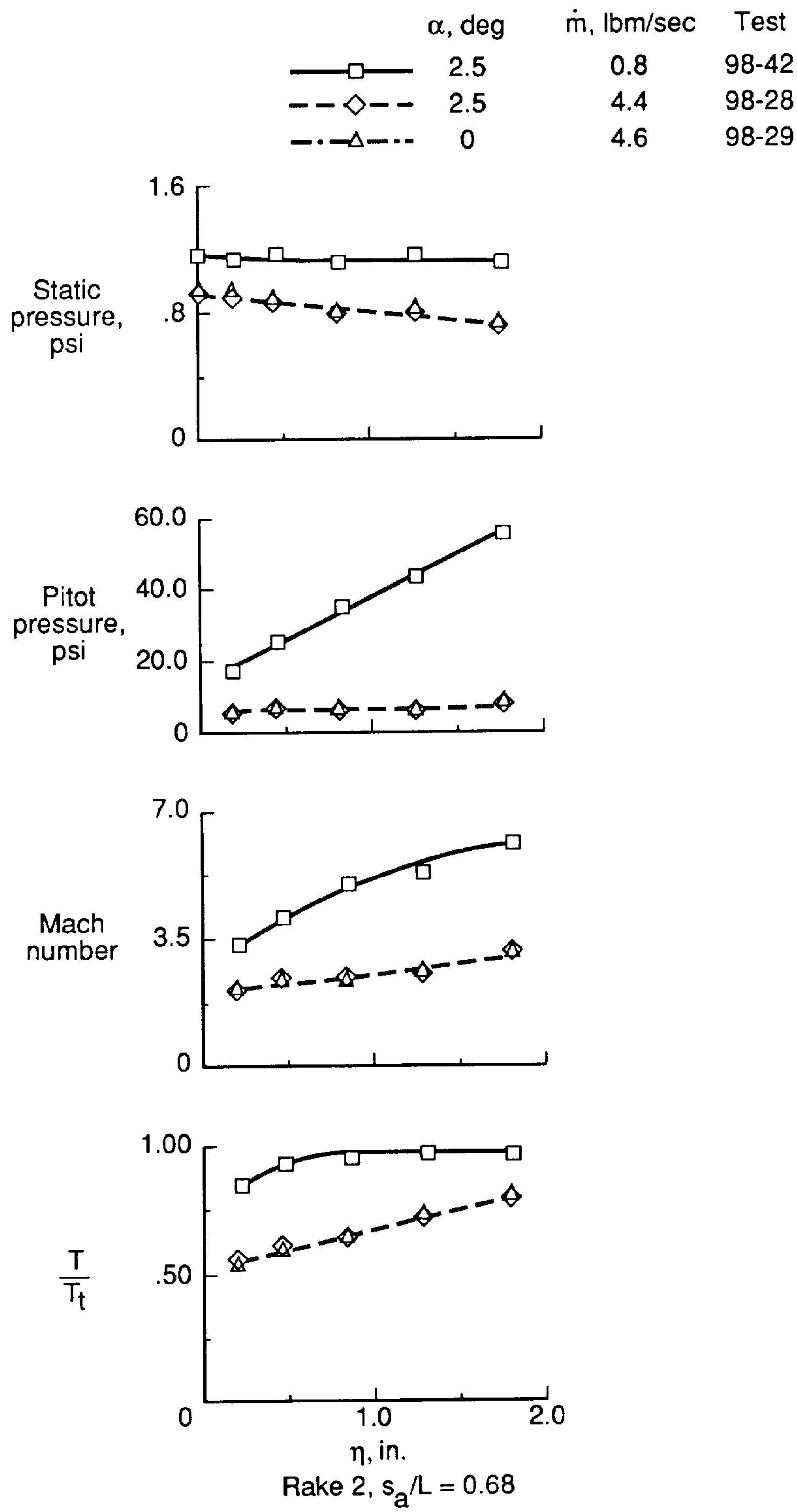

Figure 14. Shock-layer profiles for gas jet nose at $\alpha = 0°$ and $2.5°$. Rake 2; $s_a/L = 0.68$.

Nose	r_n, in.	$\dot{m}$, lbm/sec	Test	Rake 1 $s_a/L = 0.40$ Symbol	Rake 1 x/r_n	Rake 2 $s_a/L = 0.68$ Symbol	Rake 2 x/r_n	Rake 3 $s_a/L = 0.92$ Symbol	Rake 3 x/r_n
R-1	1.00		98-17	○	25.45	○	48.39	○	68.21
R-3	3.00		98-9	□	7.12	□	14.76	□	21.37
Gas jet	4.10	4.6	98-29	◇	7.10	◇	12.69		
Gas jet	2.30	1.2	98-47	△	11.78	△	21.76	△	30.37

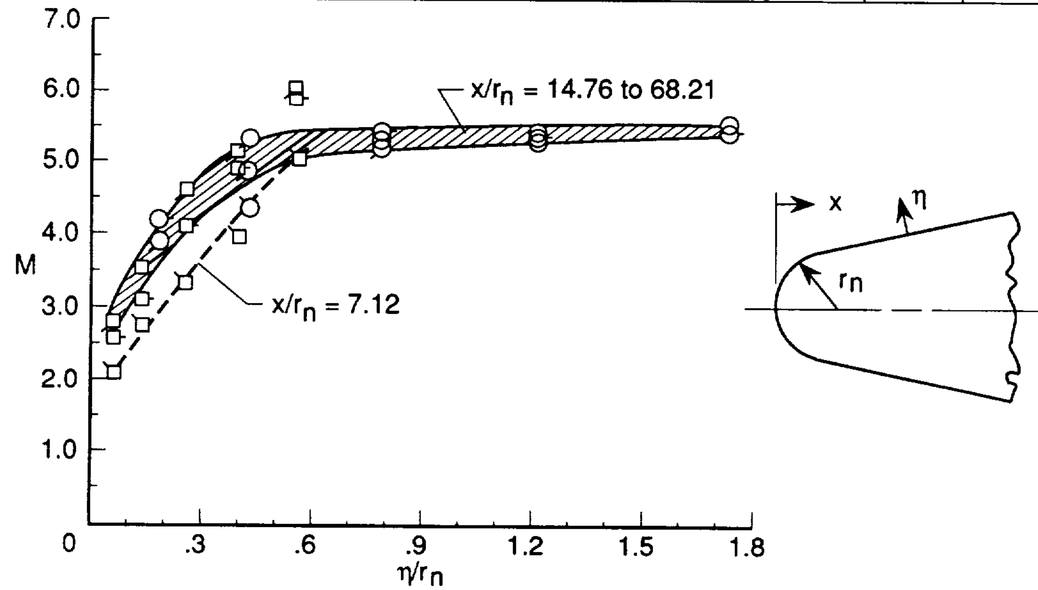

(a) Baseline (no cooling); noses R-1 and R-3.

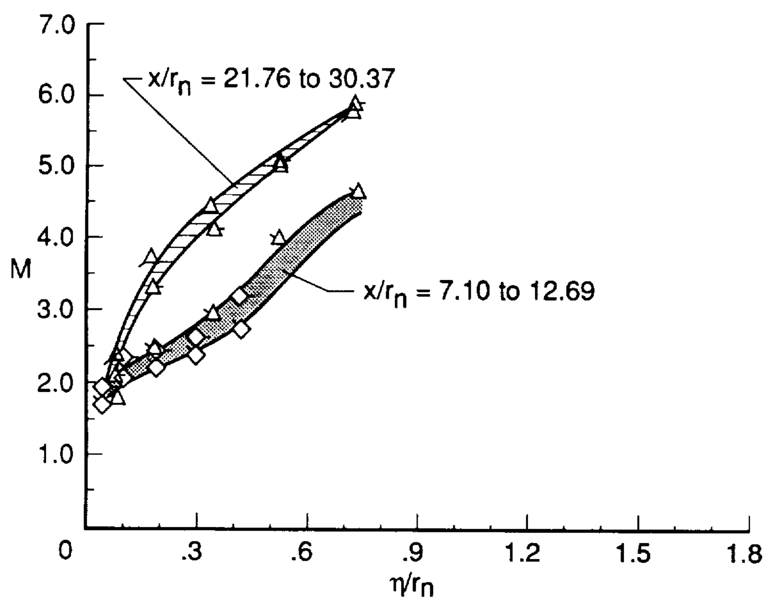

(b) Gas jet cooling; $\dot{m}$ = 1.2 and 4.6 lbm/sec.

Figure 15. Mach number versus normalized shock-layer distance.

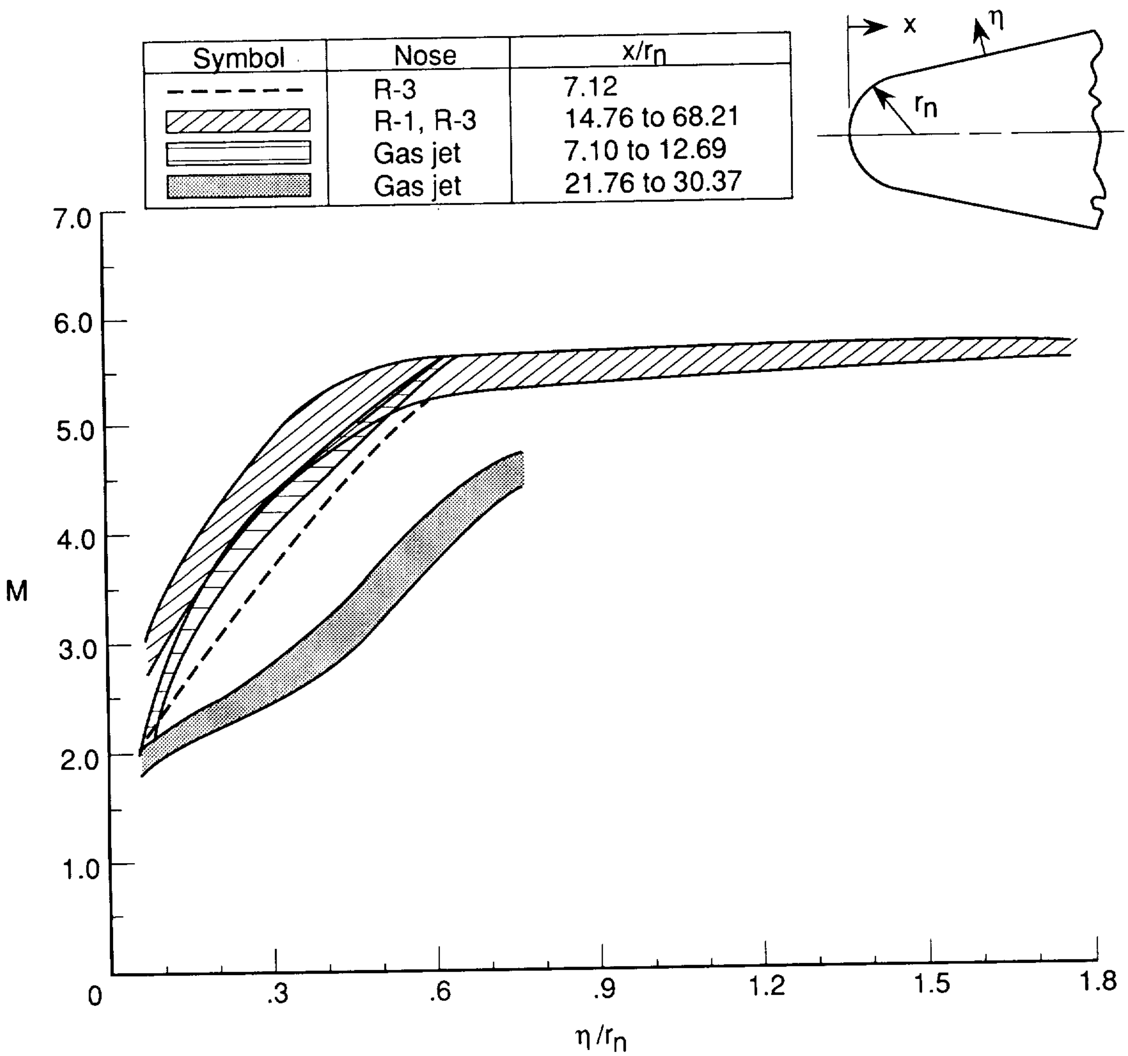

(c) Baseline and gas jet noses; $\dot{m}$ = 1.2 and 4.6 lbm/sec.

Figure 15. Concluded.

Nose	r_n, in.	$\dot{m}$, lbm/sec	Test	Rake 1 $s_a/L = 0.40$ Symbol	Rake 1 x/r_n	Rake 2 $s_a/L = 0.68$ Symbol	Rake 2 x/r_n	Rake 3 $s_a/L = 0.92$ Symbol	Rake 3 x/r_n
R-1	1.00		98-17	○	25.45	○	48.39	○	68.21
R-3	3.00		98-9	□	7.12	□	14.76	□	21.37
Gas jet	4.10	4.6	98-29	◇	7.10	◇	12.69		
Gas jet	2.30	1.2	98-47	△	11.78	△	21.76	△	30.37

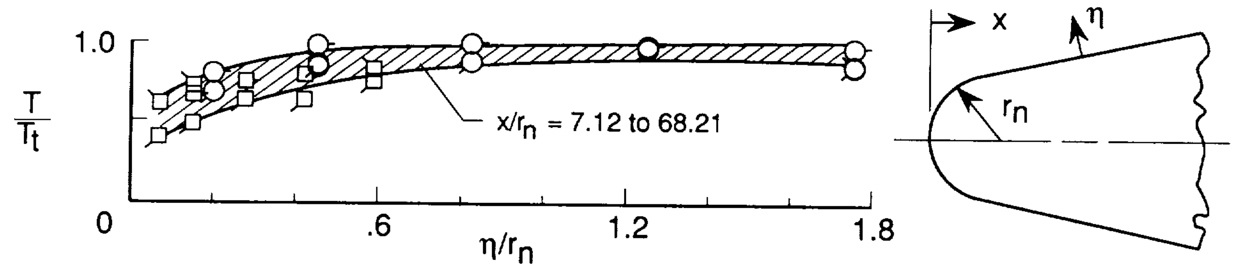

(a) Baseline (no cooling); noses R-1 and R-3.

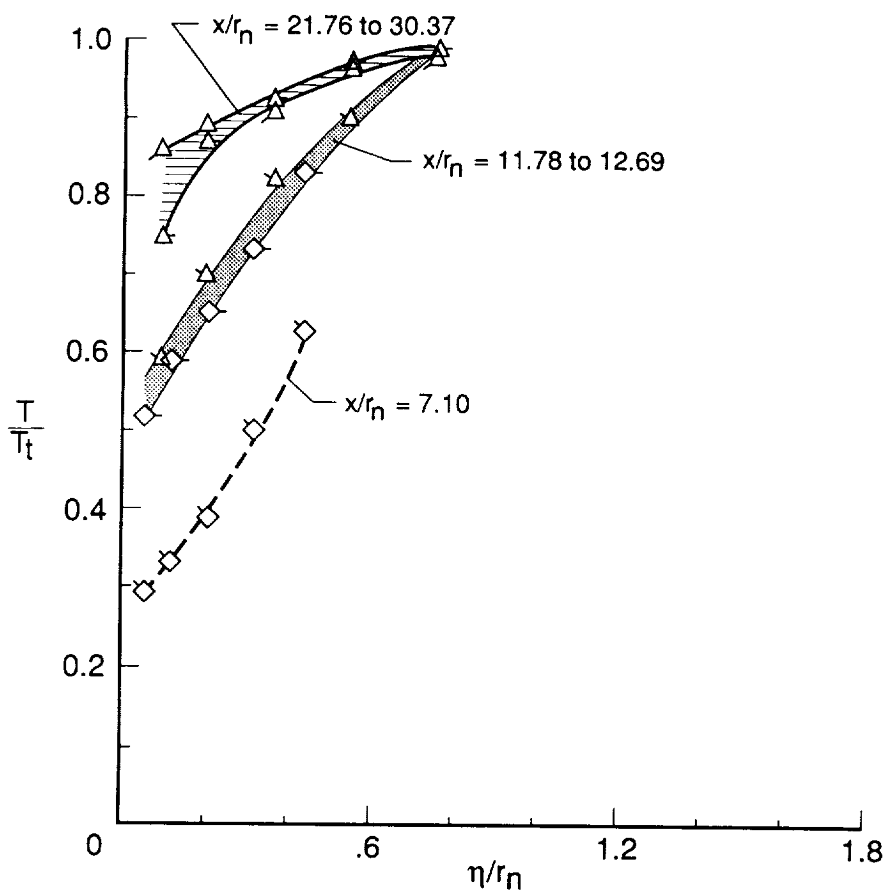

(b) Gas-jet cooling; $\dot{m}$ = 1.2 and 4.6 lbm/sec; $\frac{T_c}{T_t}$ = 0.16.

Figure 16. Total temperatures versus normalized shock-layer distance.

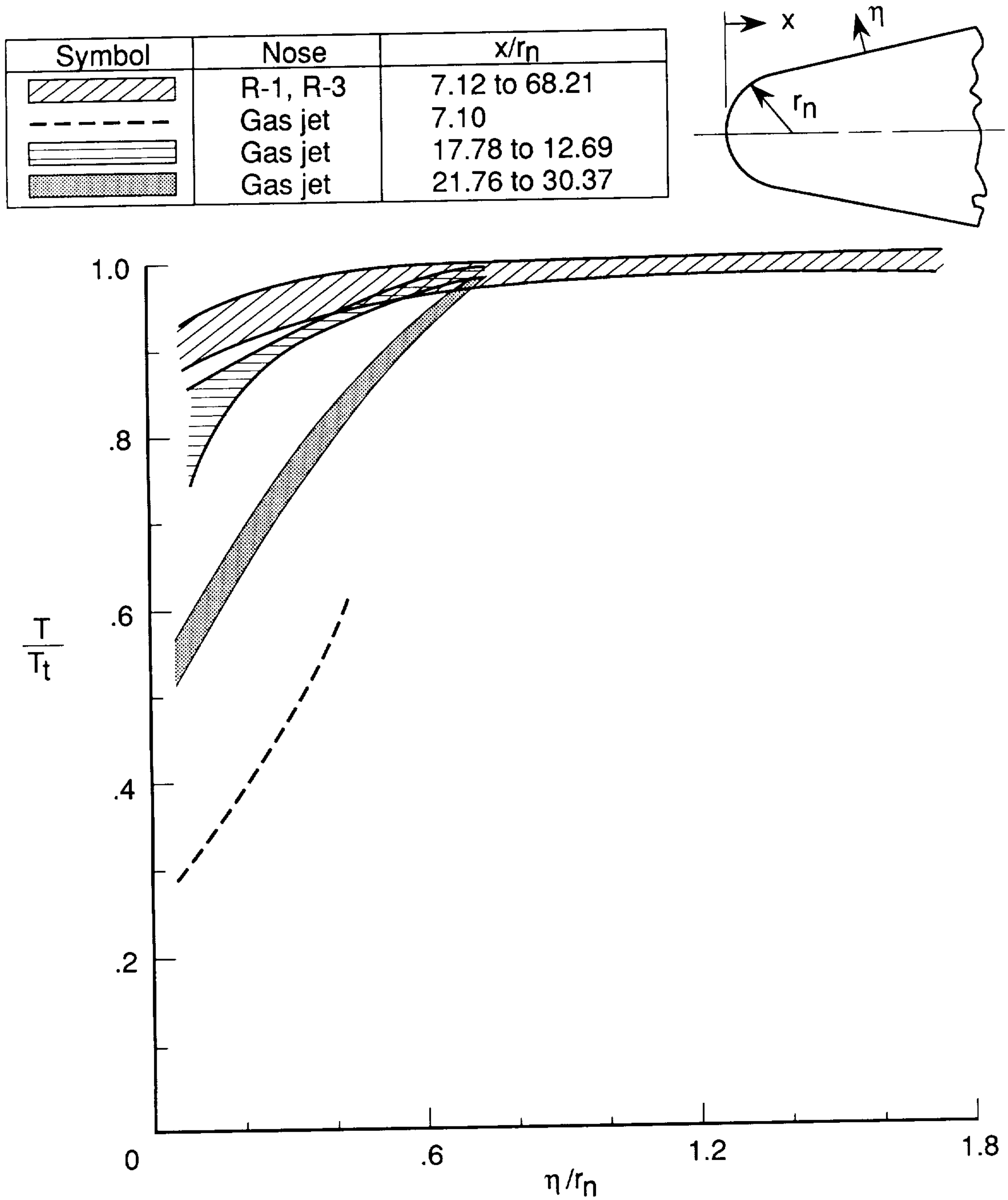

(c) Baseline and gas jet noses; $\dot{m} = 2.3$ and 4.6 lbm/sec.

Figure 16. Concluded.

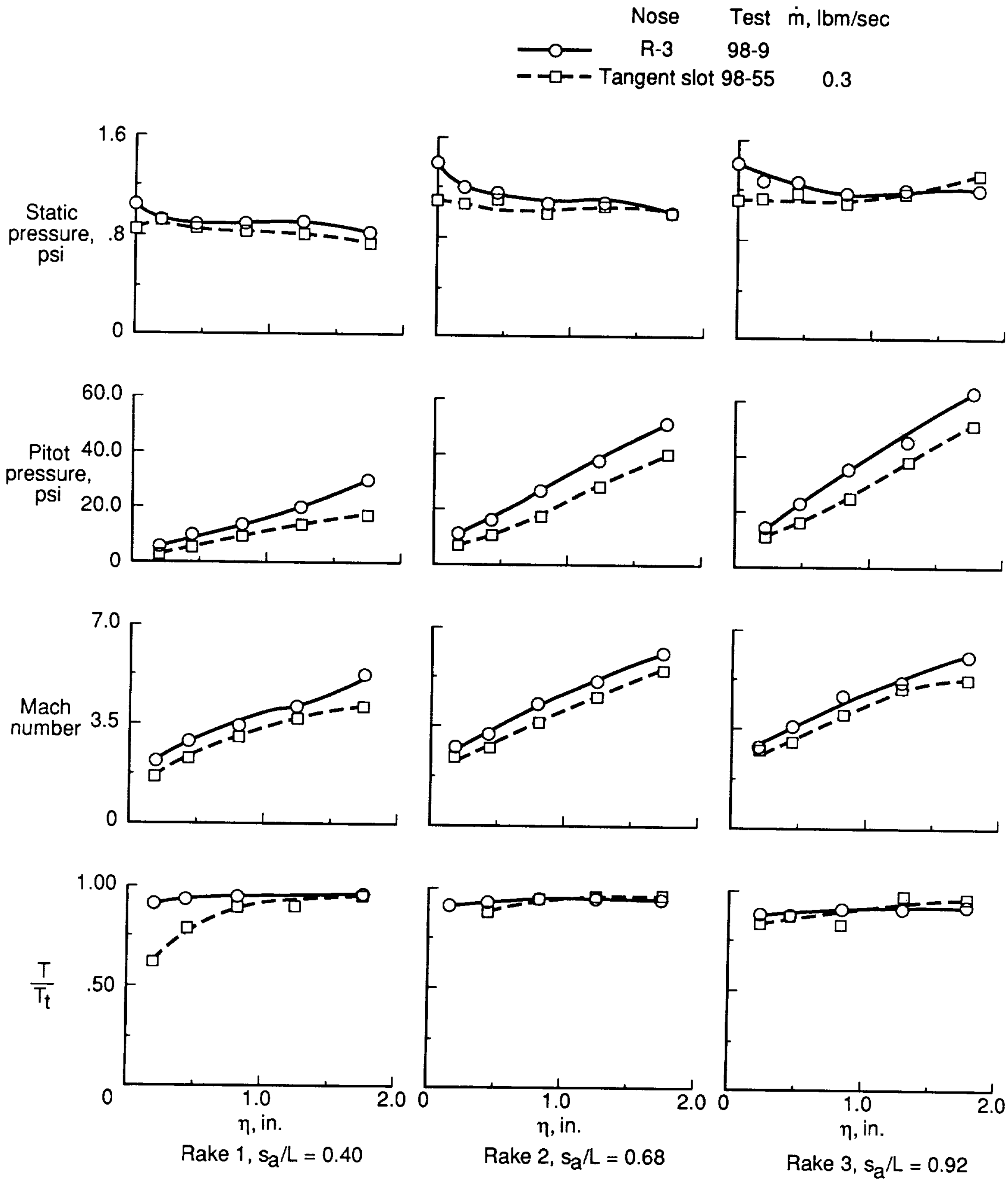

(a) $\dot{m} = 0.3$ lbm/sec.

Figure 17. Shock-layer profiles for tangent-slot and R-3 nose models, $\alpha = 0°$.

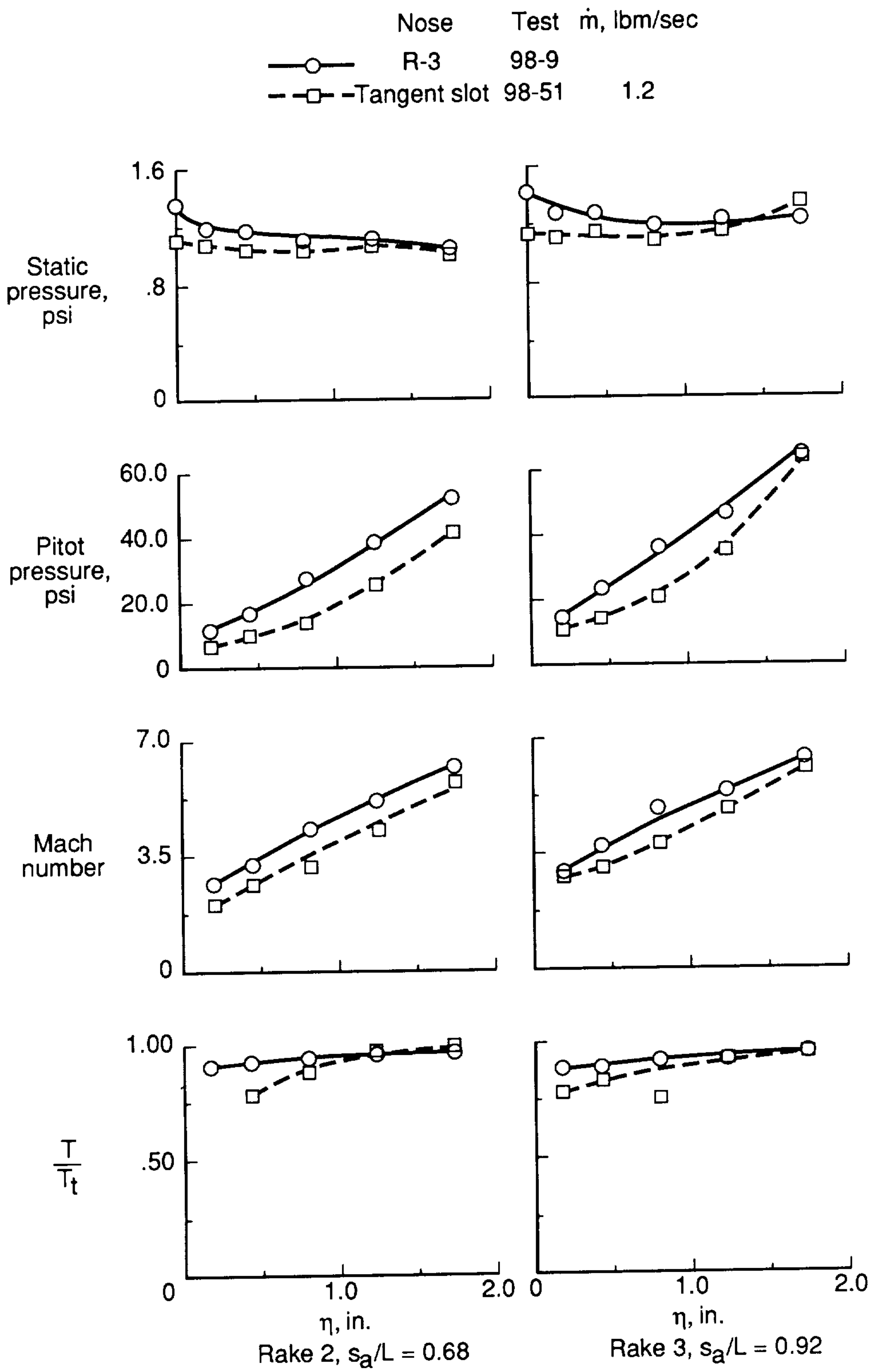

(b) $\dot{m}$ = 1.2 lbm/sec.

Figure 17. Continued.

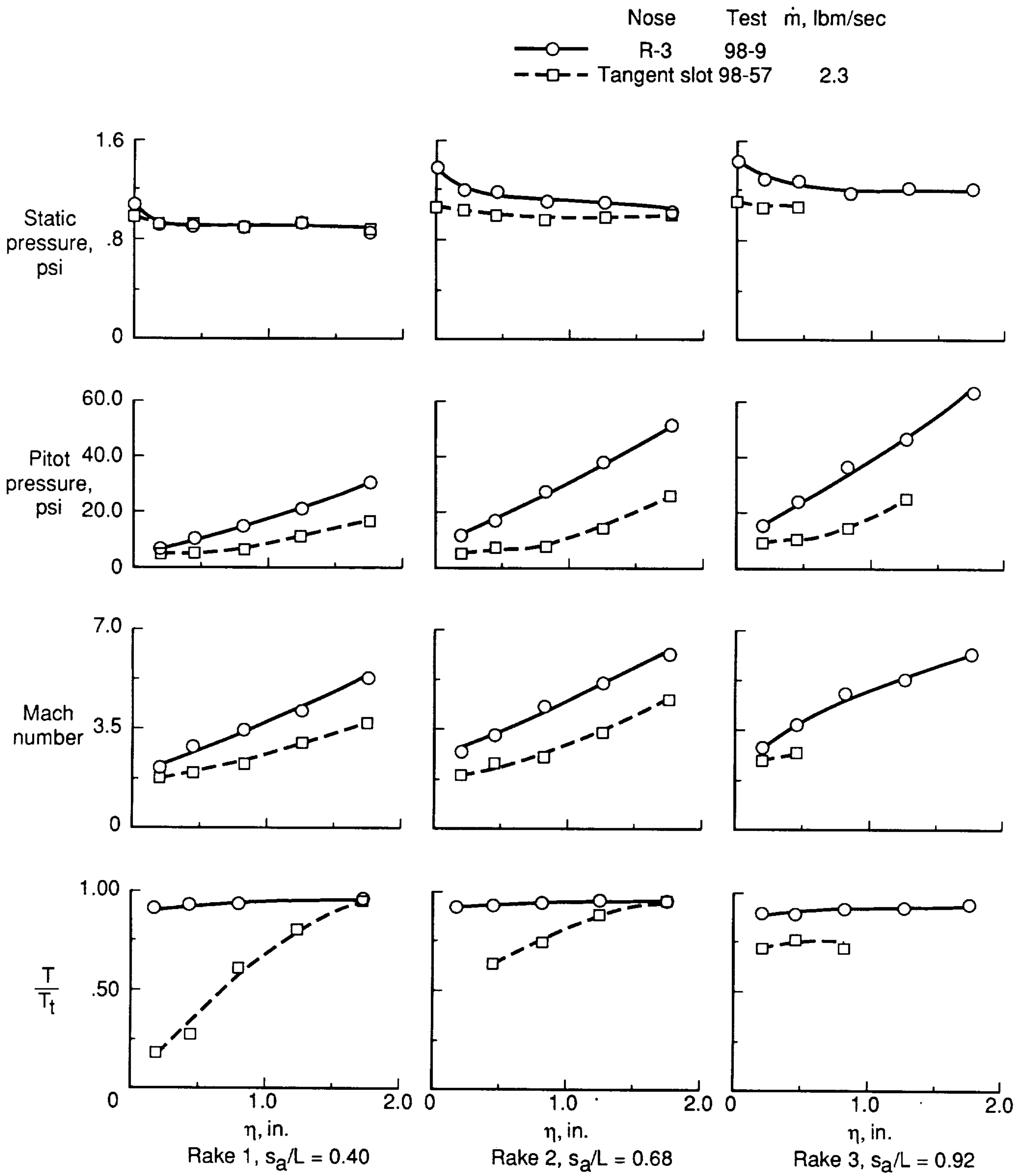

(c) $\dot{m}$ = 2.3 lbm/sec.

Figure 17. Concluded.

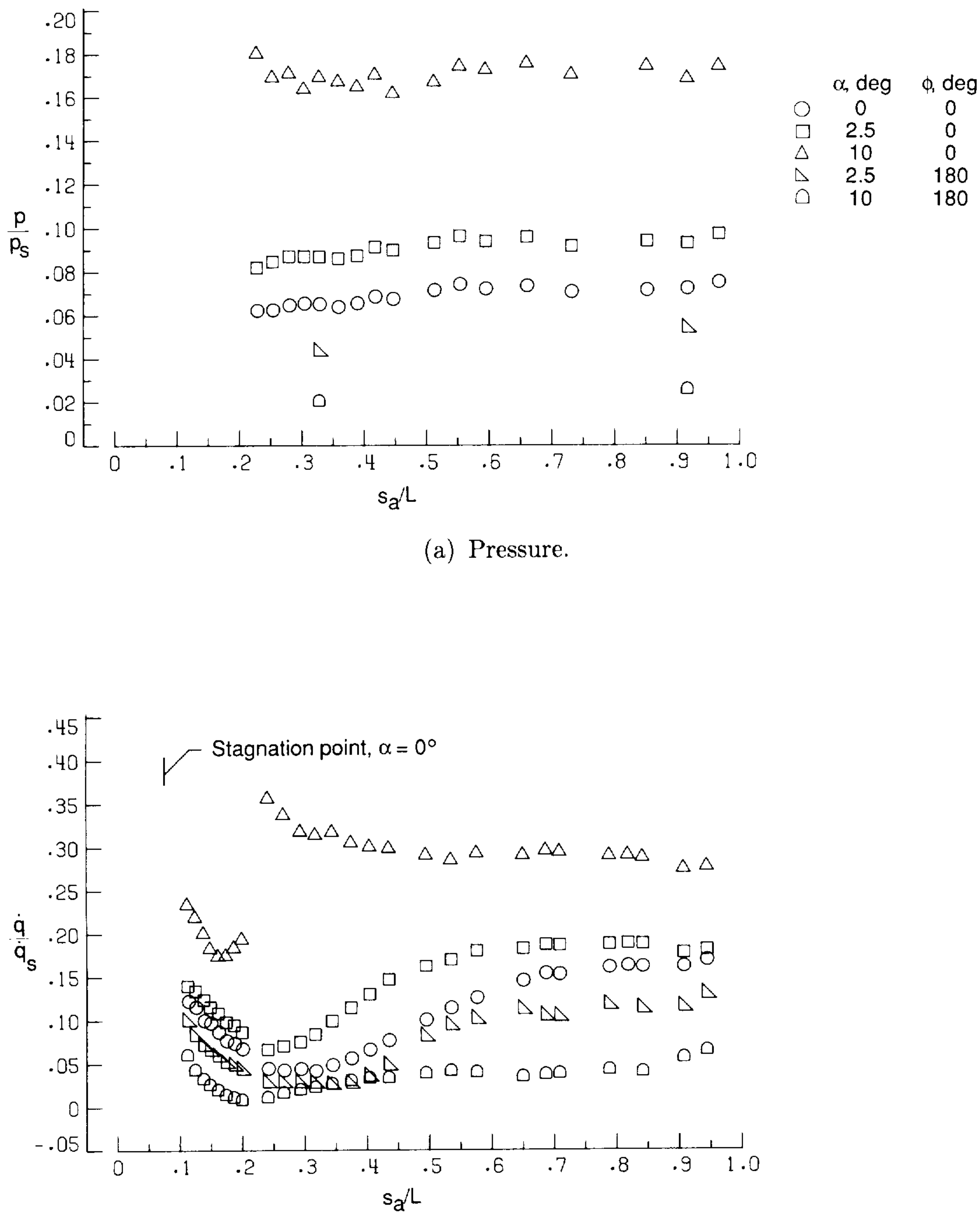

(a) Pressure.

(b) Heat flux.

Figure 18. Baseline longitudinal pressure and heat-flux distributions for R-1 nose (no cooling).

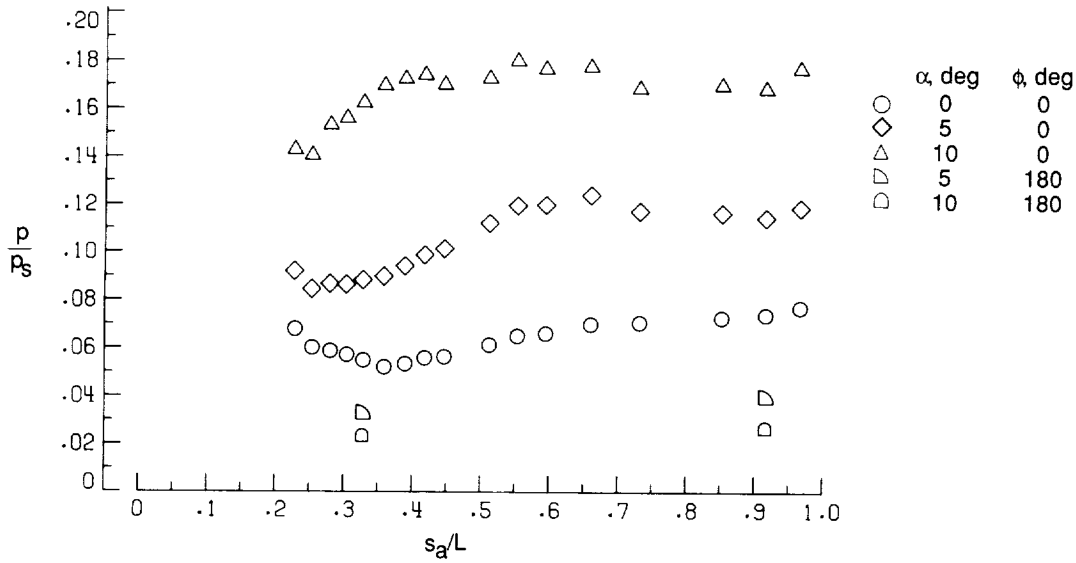

(a) Pressure.

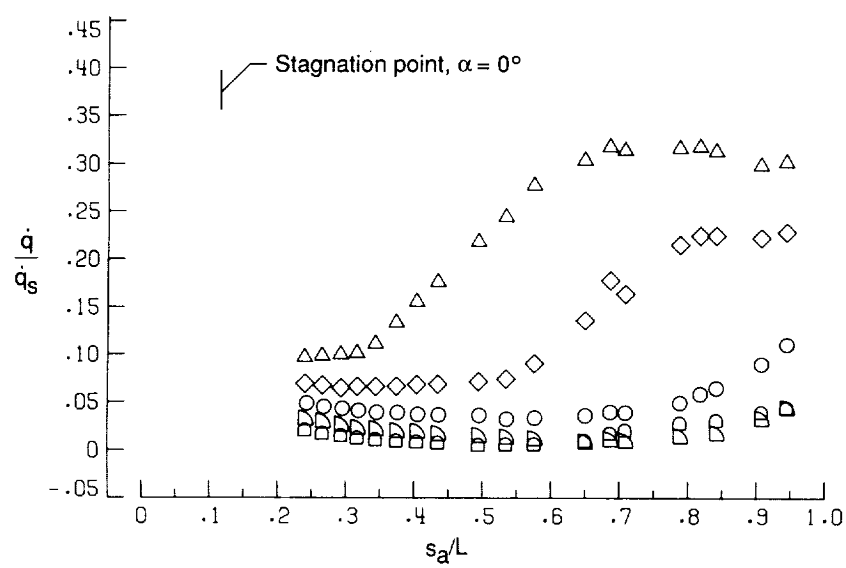

(b) Heat flux.

Figure 19. Baseline longitudinal pressure and heat-flux distributions for R-3 nose (no cooling).

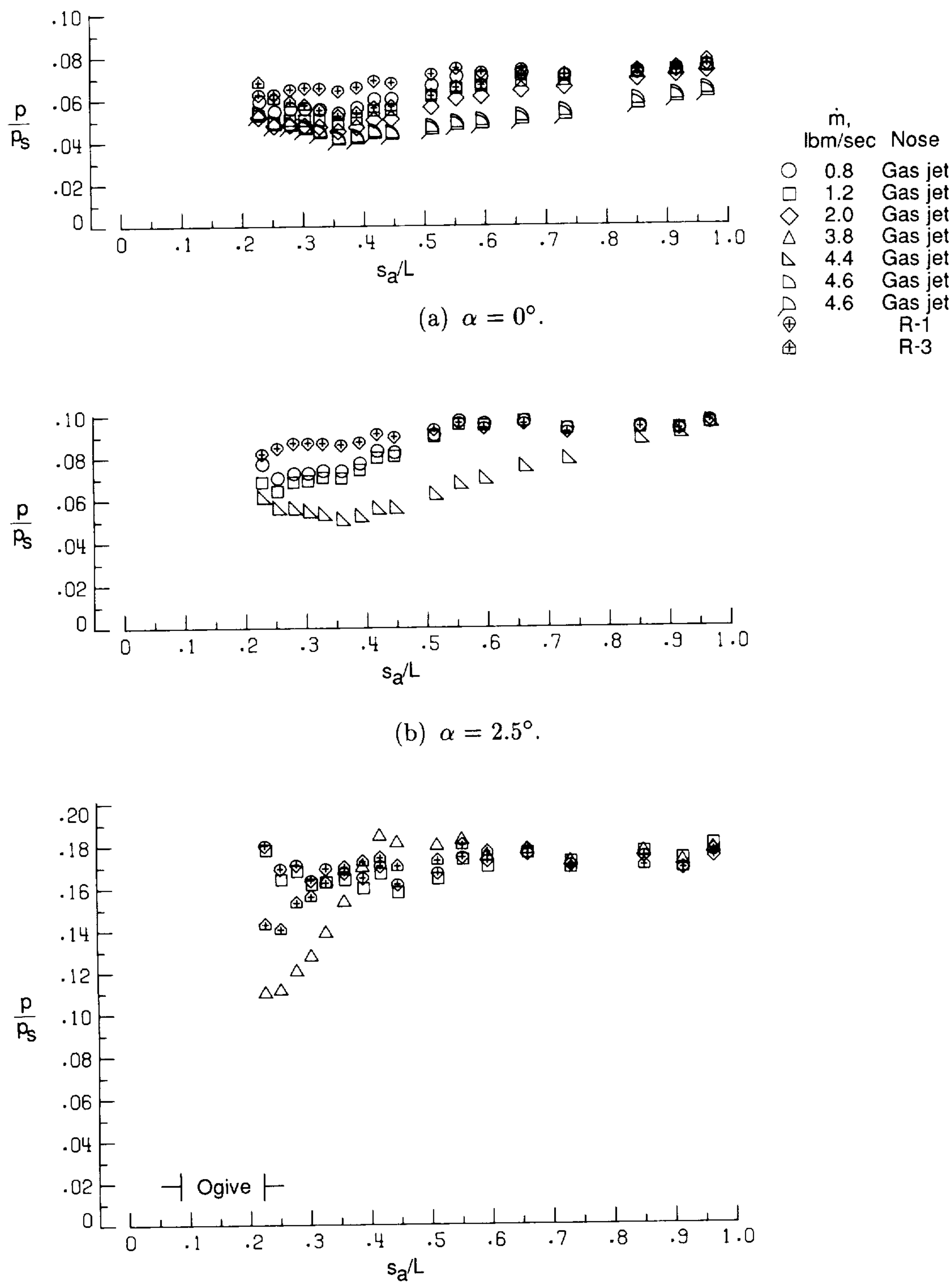

(a) $\alpha = 0°$.

(b) $\alpha = 2.5°$.

(c) $\alpha = 10°$.

Figure 20. Windward longitudinal pressure distributions for gas-jet, R-1, and R-3 noses at $\phi = 0°$.

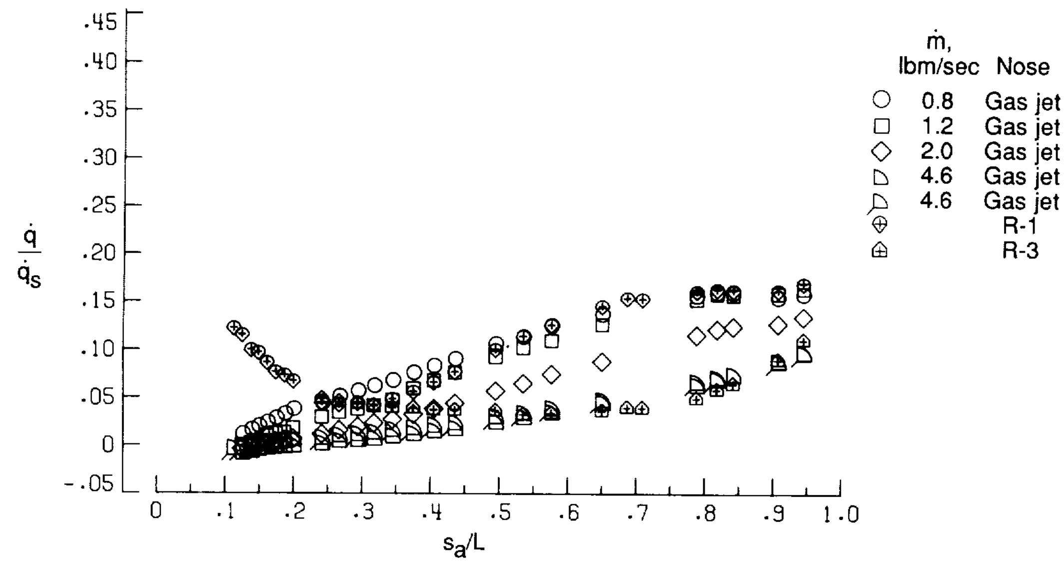

(a) $\phi = 0°$.

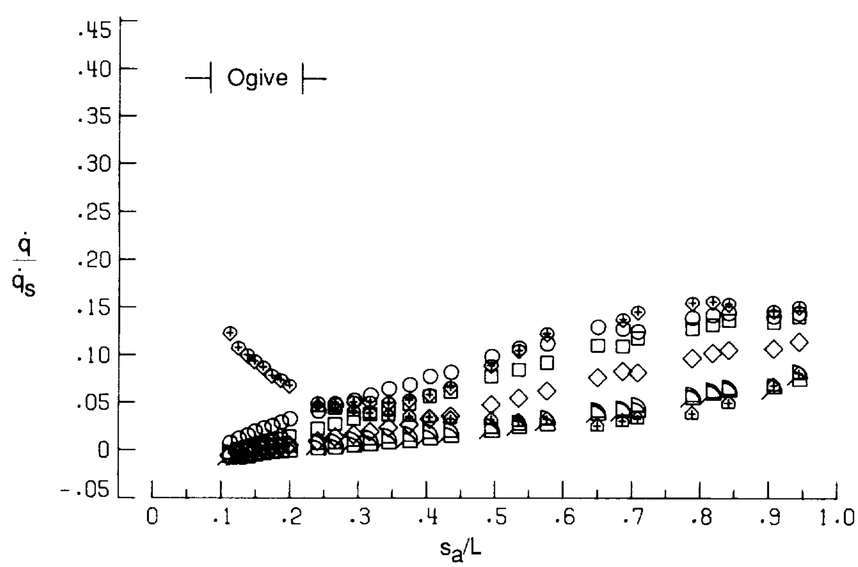

(b) $\phi = 180°$.

Figure 21. Longitudinal heat-flux distributions for gas-jet, R-1, and R-3 noses at $\alpha = 0°$.

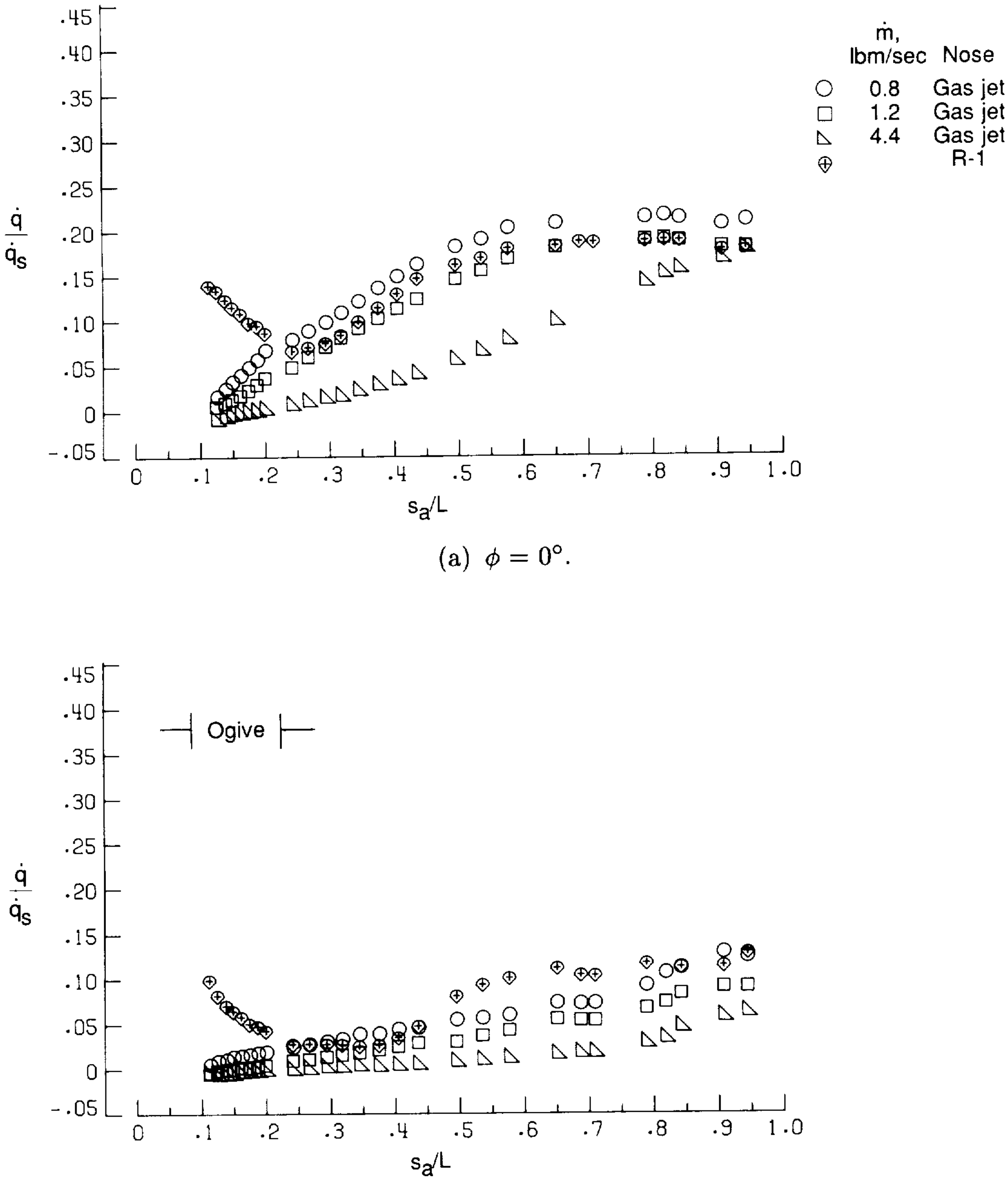

(a) $\phi = 0°$.

(b) $\phi = 180°$.

Figure 22. Longitudinal heat-flux distributions for gas-jet and R-1 noses at $\alpha = 2.5°$.

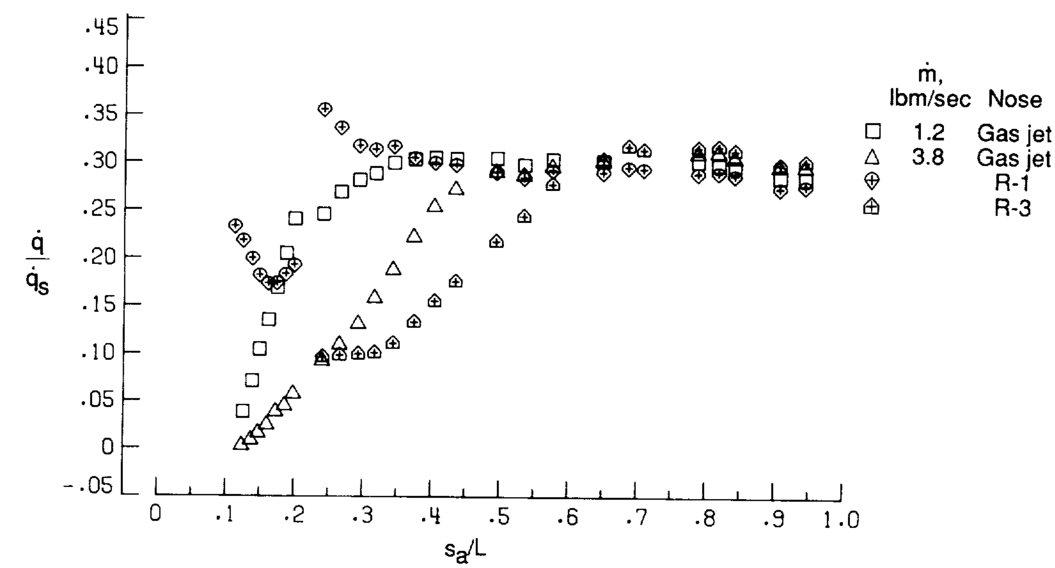

(a) $\phi = 0°$.

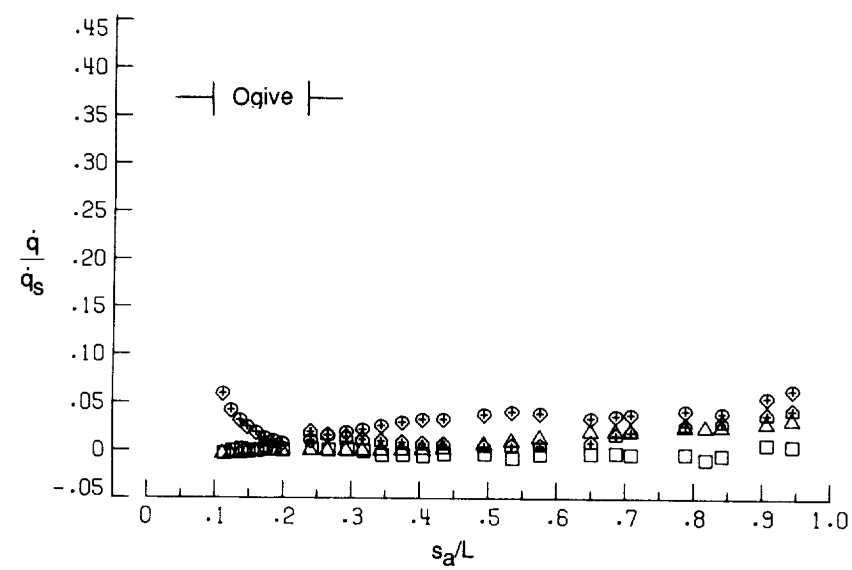

(b) $\phi = 180°$.

Figure 23. Longitudinal heat-flux distributions for gas-jet, R-1, and R-3 noses at $\alpha = 10°$.

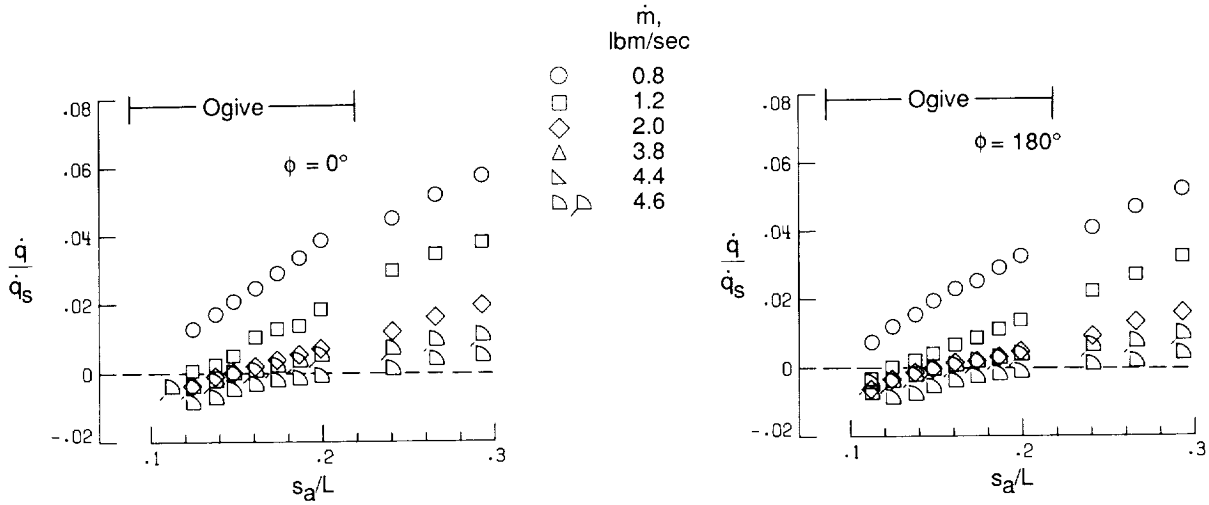

(a) $\alpha = 0°$.

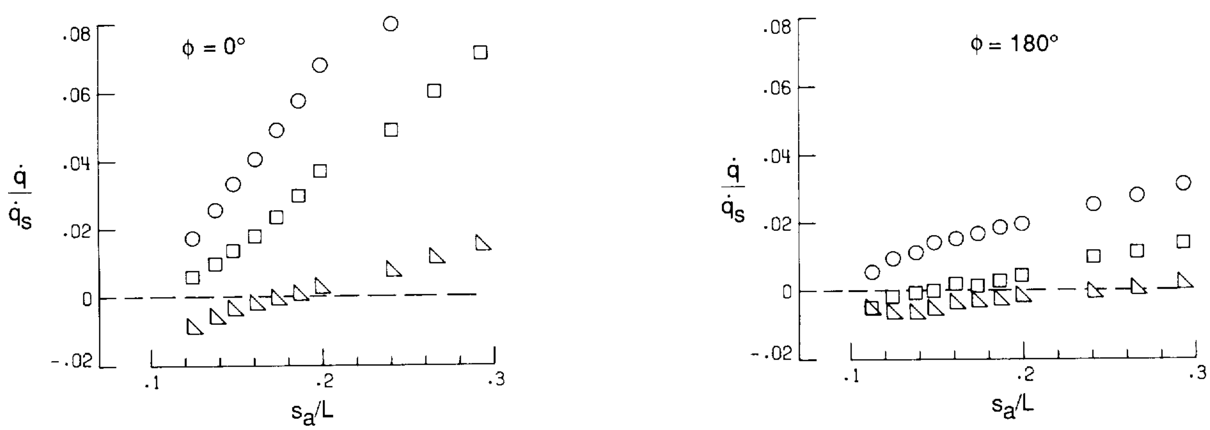

(b) $\alpha = 2.5°$.

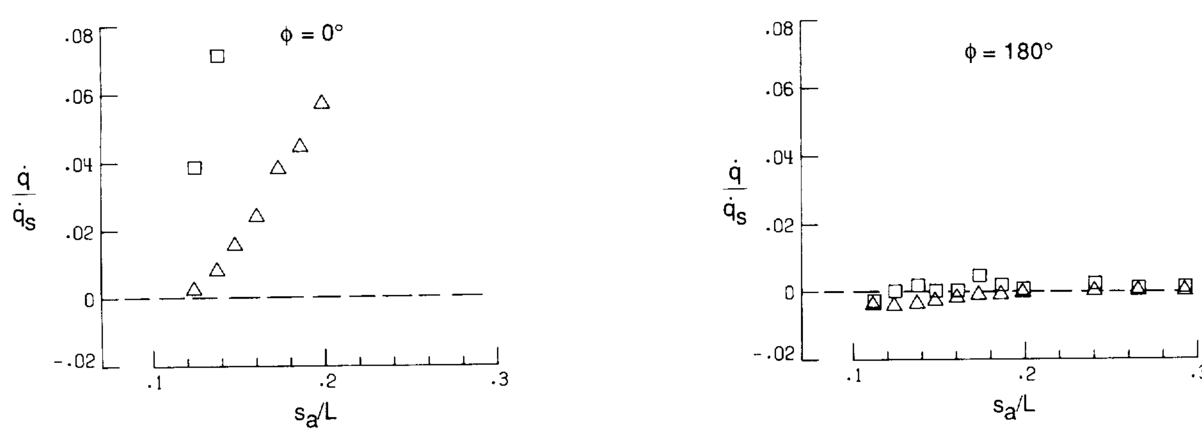

(c) $\alpha = 10°$.

Figure 24. Enlargement of figures 21 through 23 showing longitudinal heating distributions for various coolant flow rates and angles of attack.

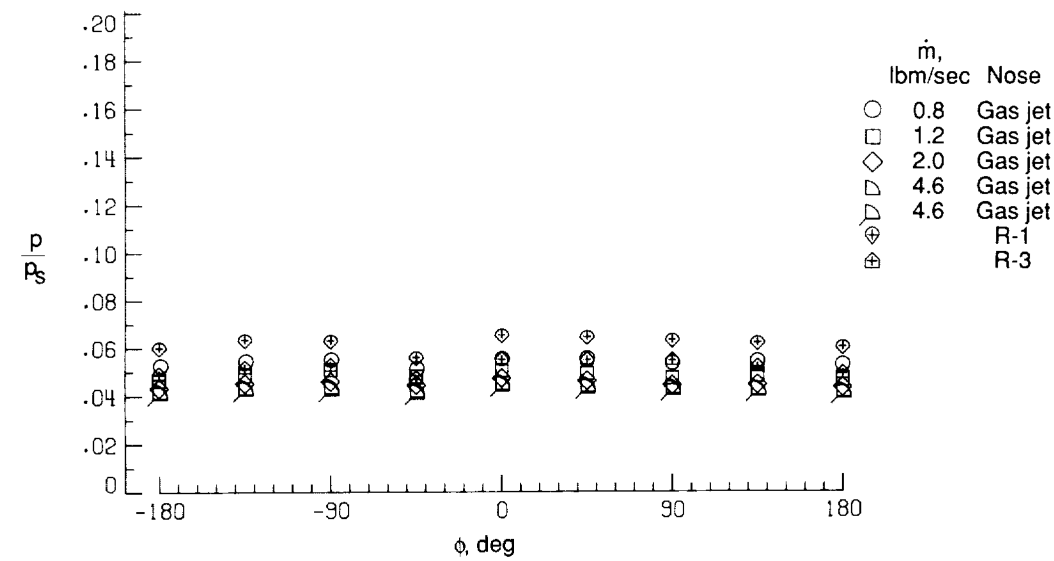

(a) $s_a/L = 0.33$.

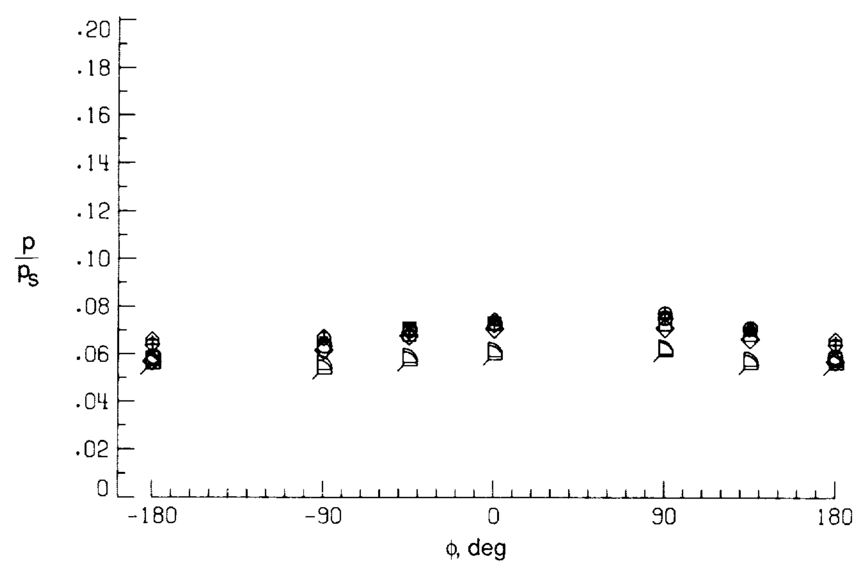

(b) $s_a/L = 0.92$.

Figure 25. Circumferential pressure distributions for gas-jet, R-1, and R-3 noses at $\alpha = 0°$.

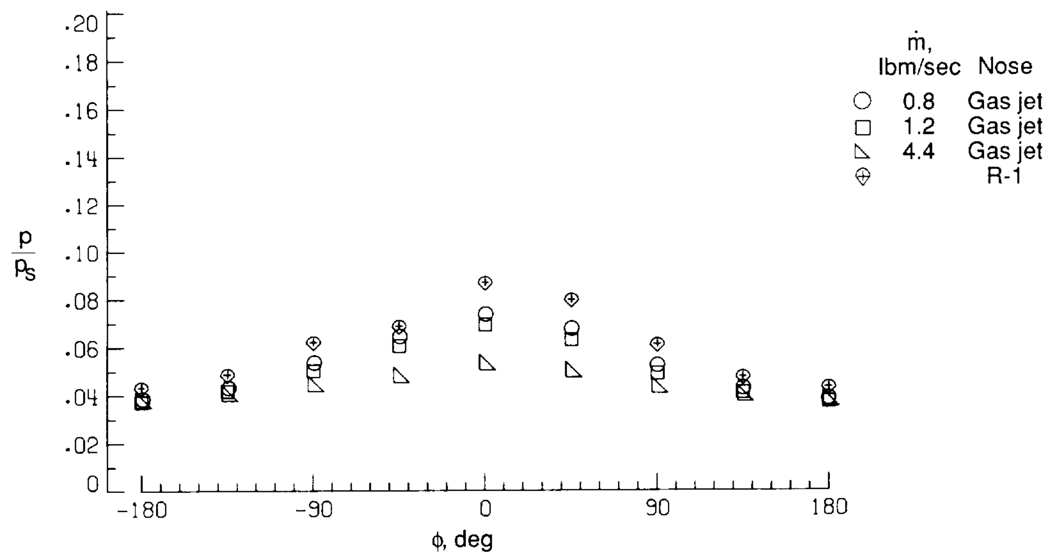

(a) $s_a/L = 0.33$.

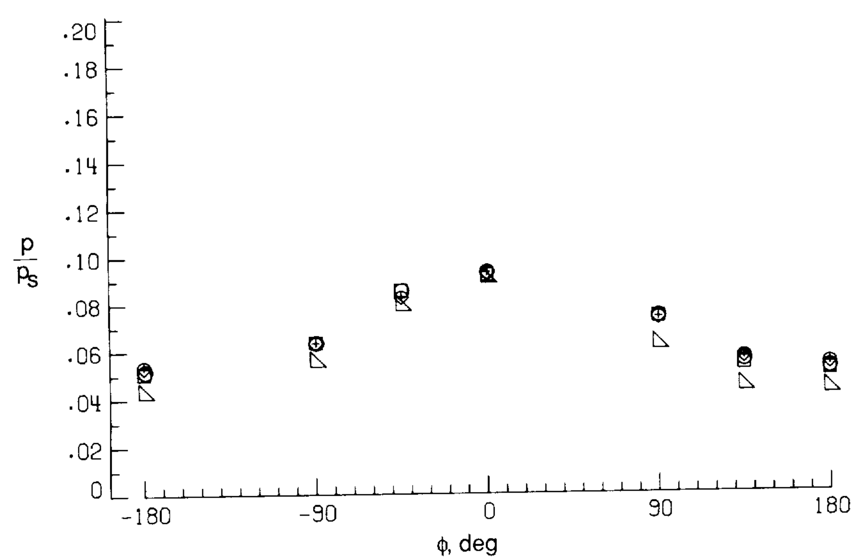

(b) $s_a/L = 0.92$.

Figure 26. Circumferential pressure distributions for gas-jet and R-1 noses at $\alpha = 2.5°$.

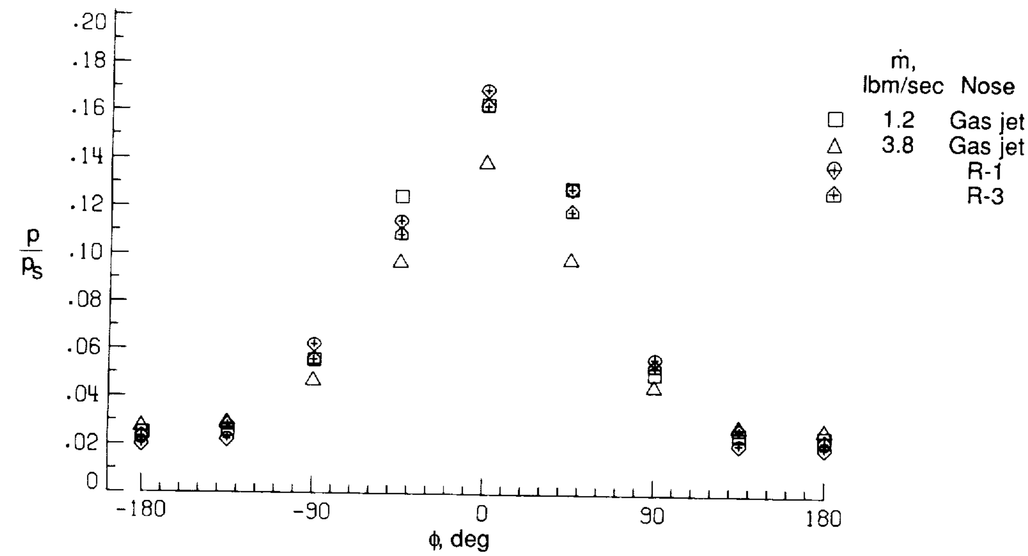

(a) $s_a/L = 0.33$.

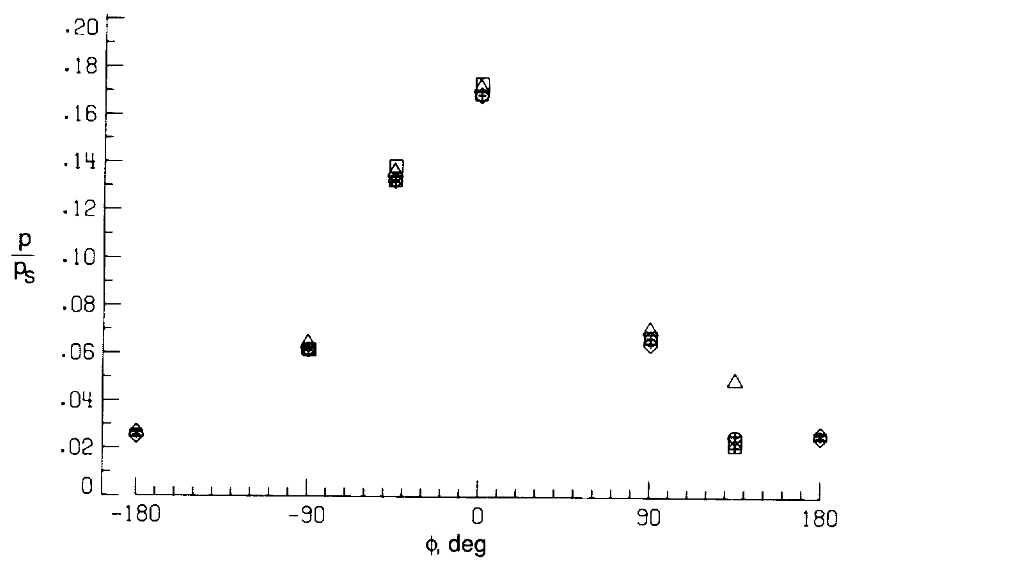

(b) $s_a/L = 0.92$.

Figure 27. Circumferential pressure distributions for gas-jet, R-1, and R-3 noses at $\alpha = 10°$.

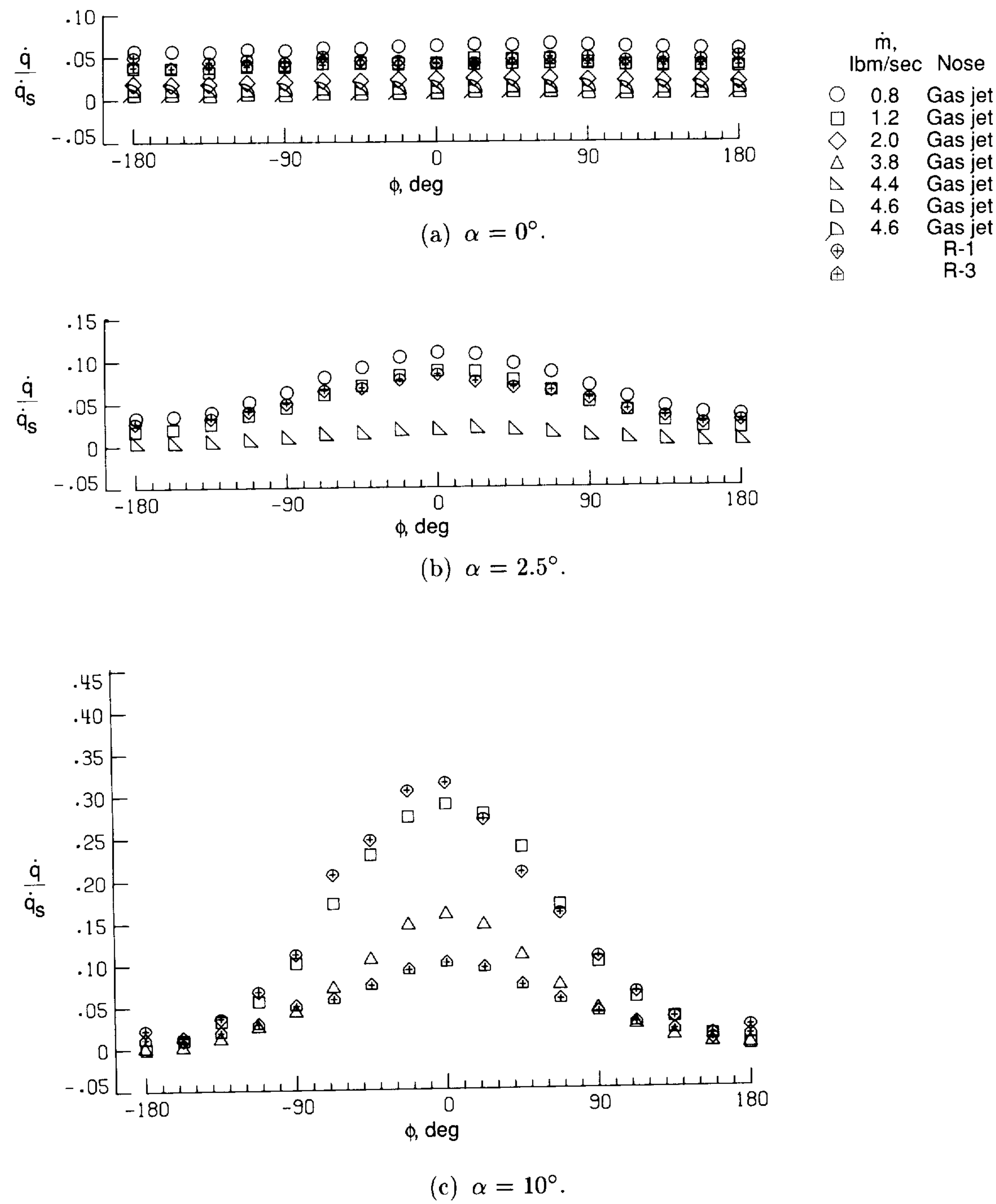

Figure 28. Circumferential heat-flux distributions for gas-jet, R-1, and R-3 noses at $s_a/L = 0.32$.

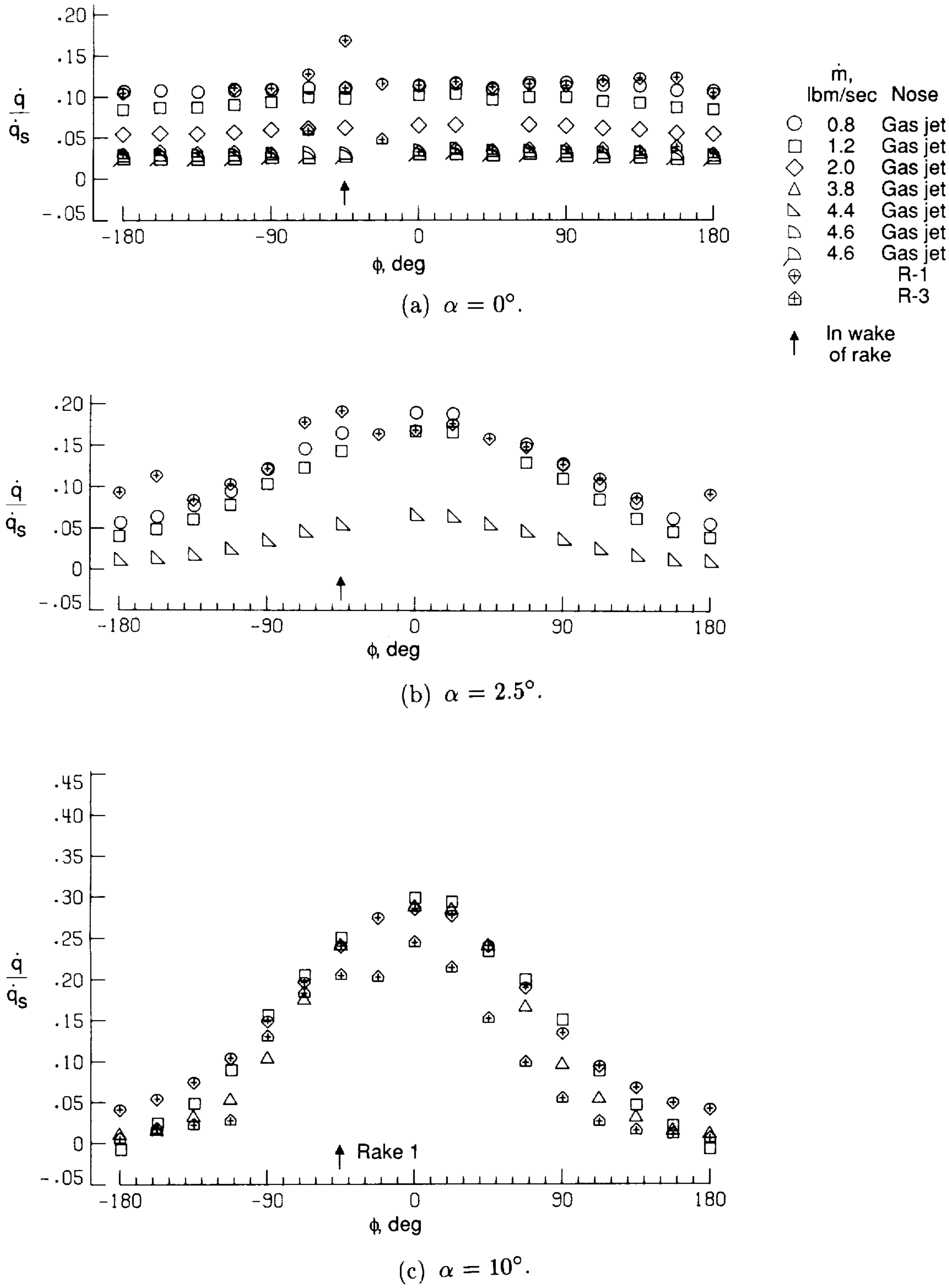

Figure 29. Circumferential heat-flux distributions for gas-jet, R-1, and R-3 noses at $s_a/L = 0.53$.

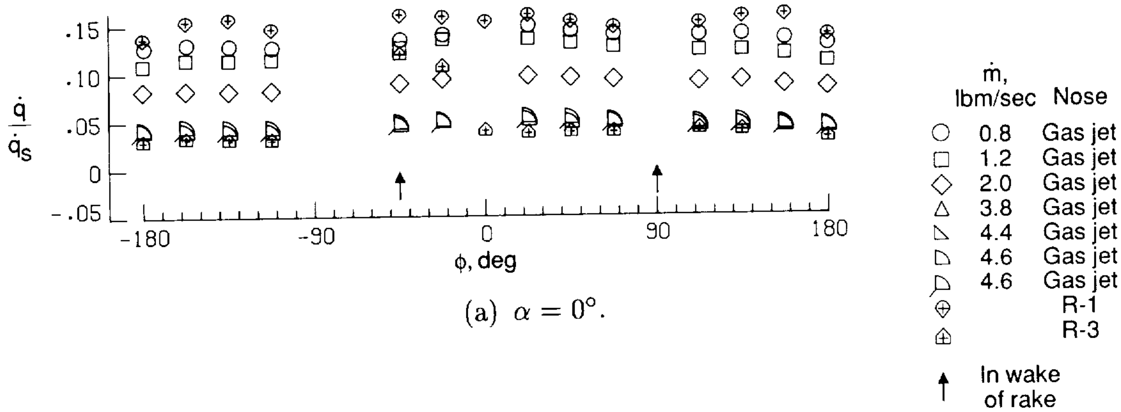

(a) $\alpha = 0°$.

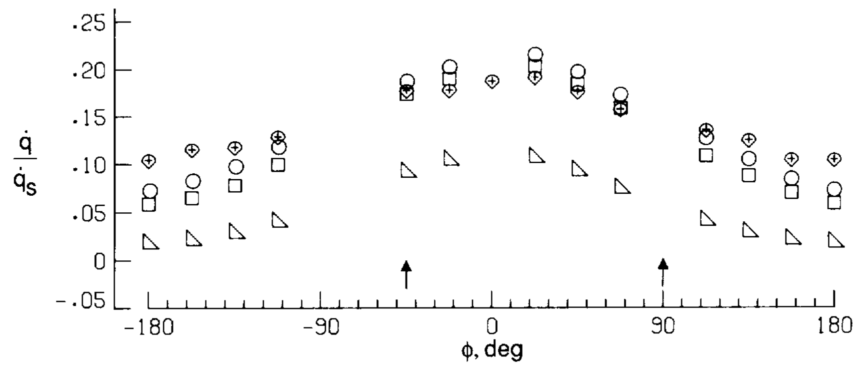

(b) $\alpha = 2.5°$.

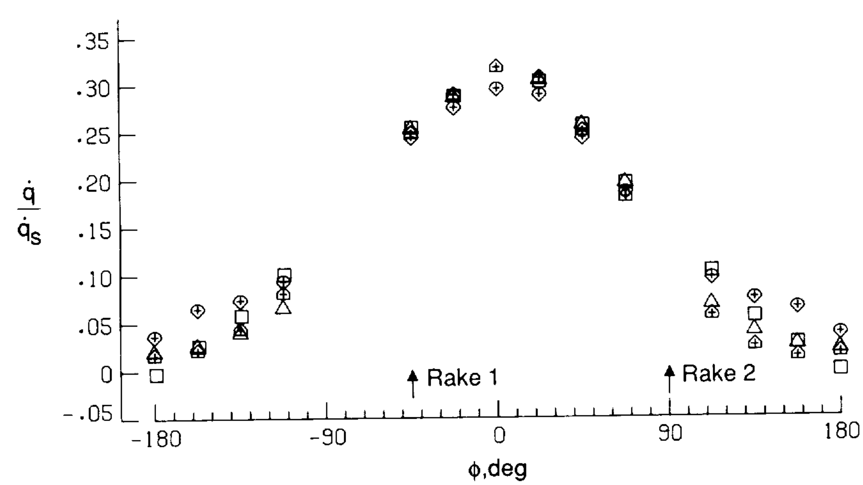

(c) $\alpha = 10°$.

Figure 30. Circumferential heat-flux distributions for gas-jet, R-1, and R-3 noses at $s_a/L = 0.69$.

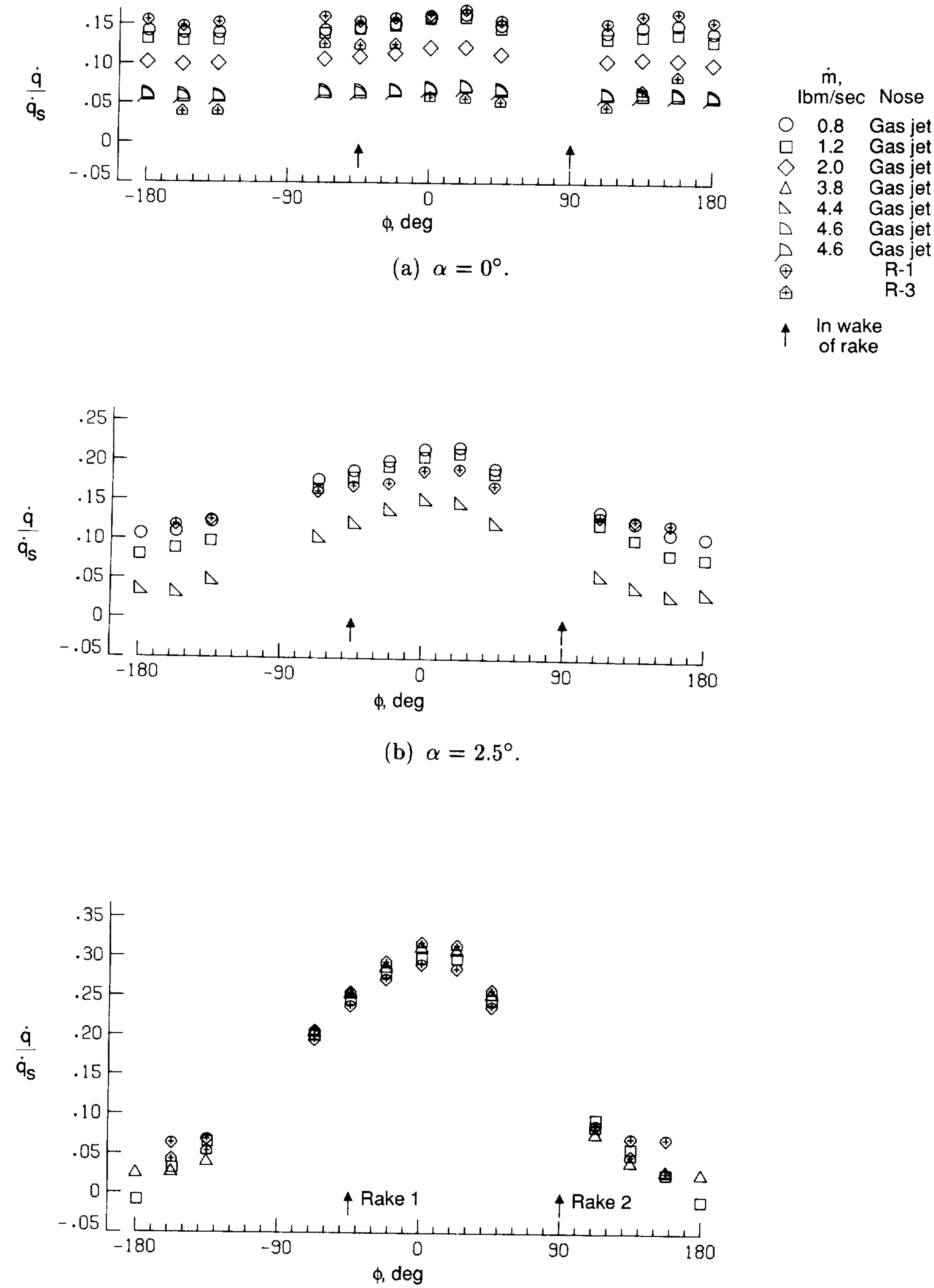

(a) $\alpha = 0°$.

(b) $\alpha = 2.5°$.

(c) $\alpha = 10°$.

Figure 31. Circumferential heat-flux distributions for gas-jet, R-1, and R-3 noses at $s_a/L = 0.82$.

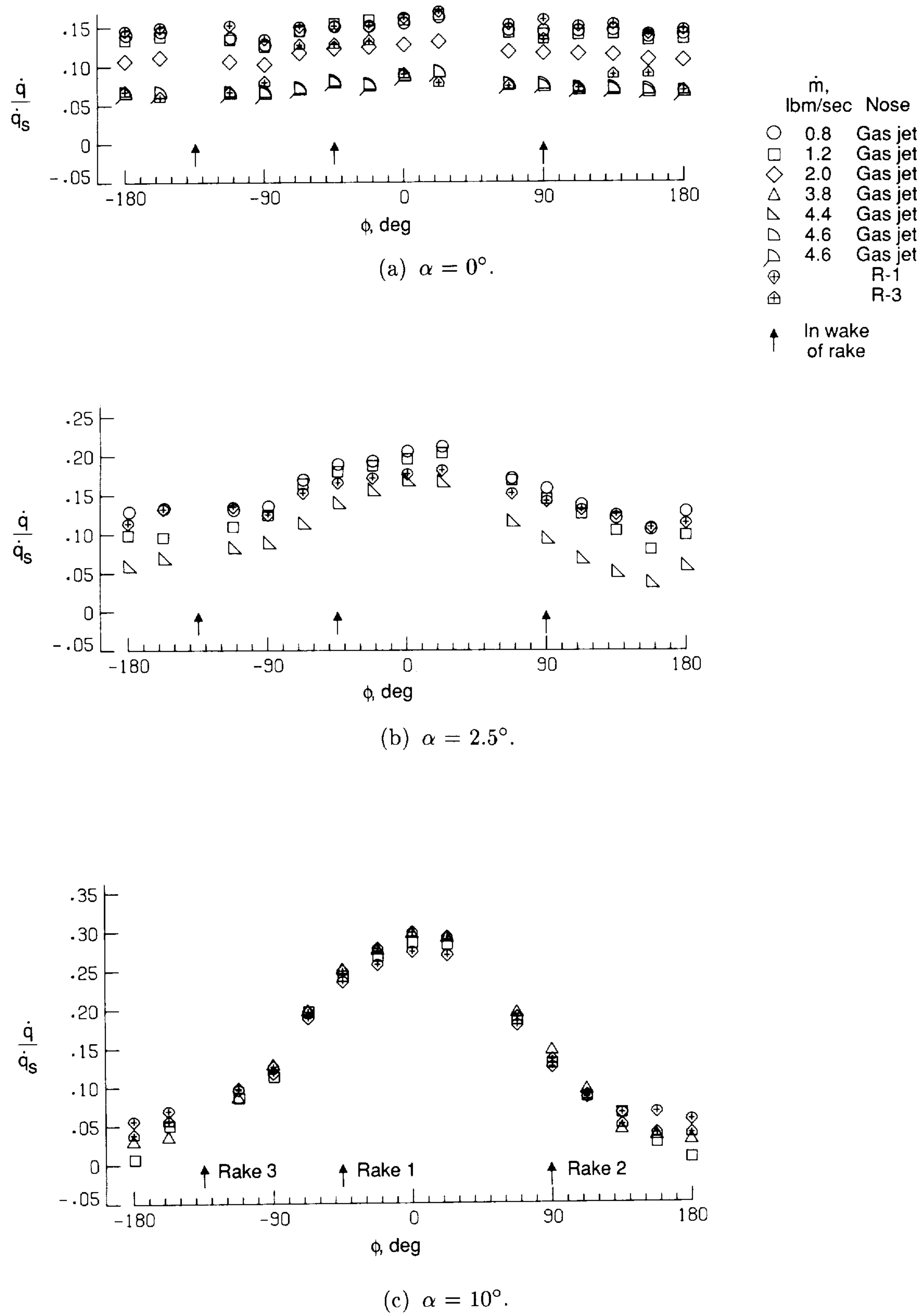

Figure 32. Circumferential heat-flux distributions for gas-jet, R-1, and R-3 noses at $s_a/L = 0.91$.

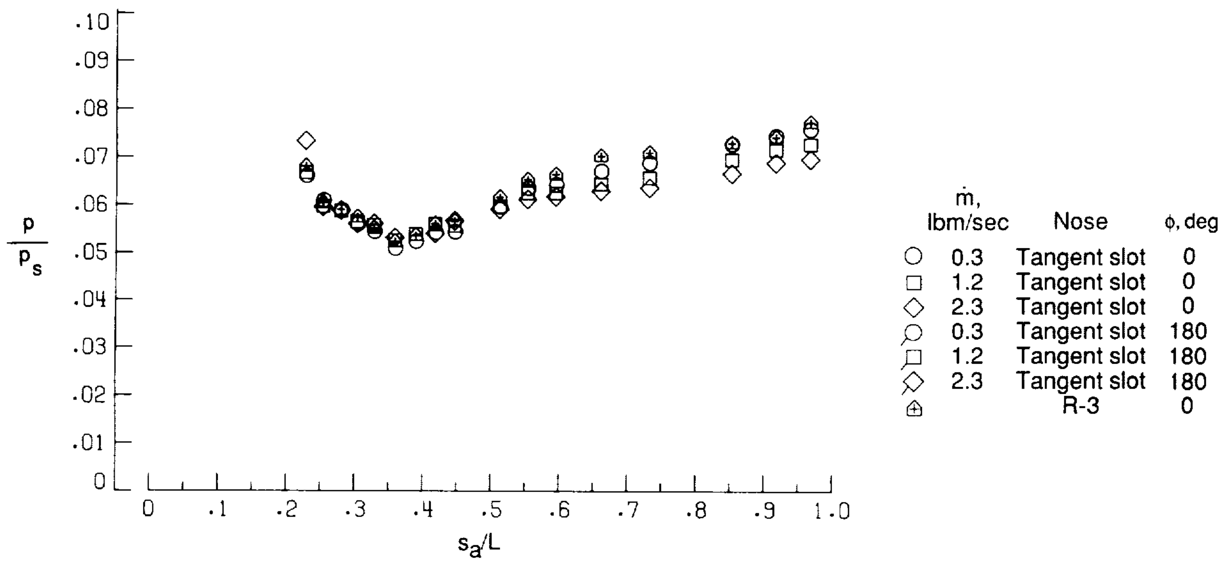

(a) Pressure.

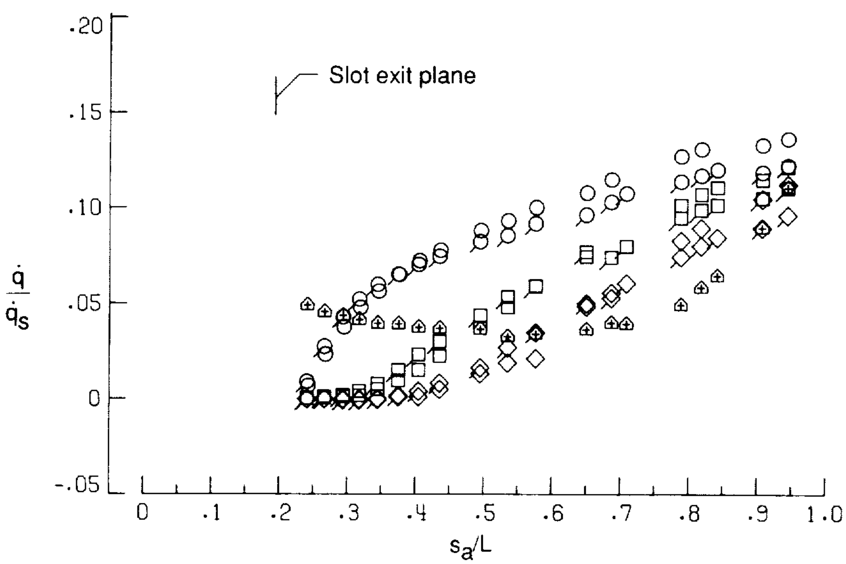

(b) Heat flux.

Figure 33. Longitudinal pressure and heat-flux distributions for tangent-slot and baseline R-3 noses.

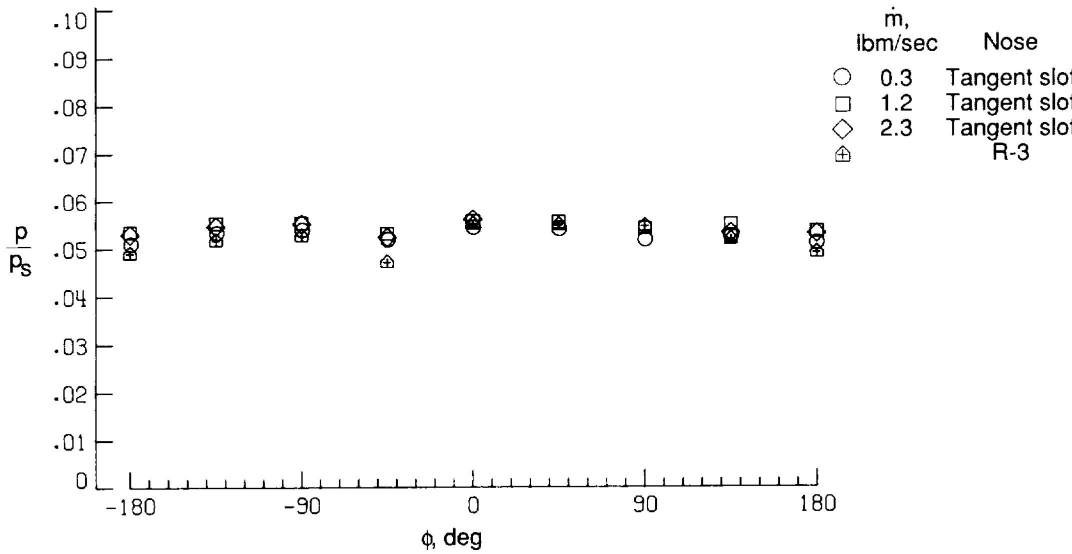

(a) $s_a/L = 0.33$.

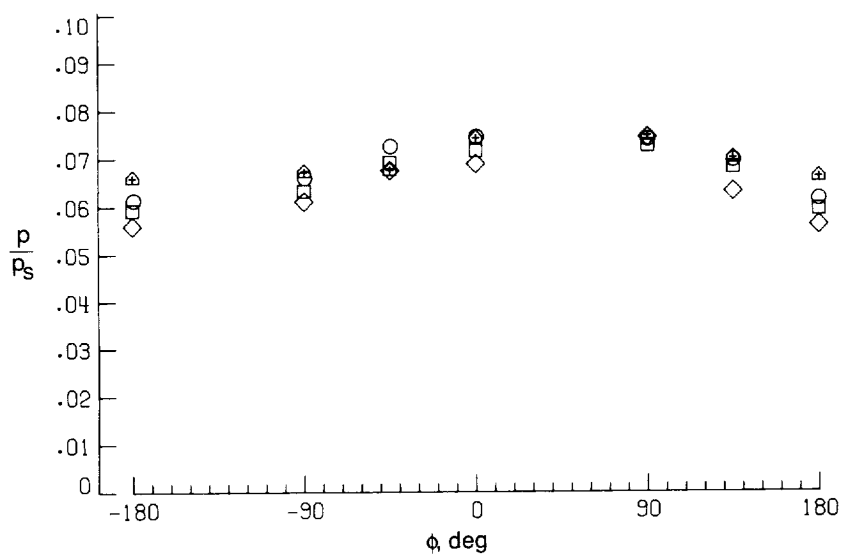

(b) $s_a/L = 0.92$.

Figure 34. Circumferential pressure distributions for tangent-slot and baseline R-3 noses.

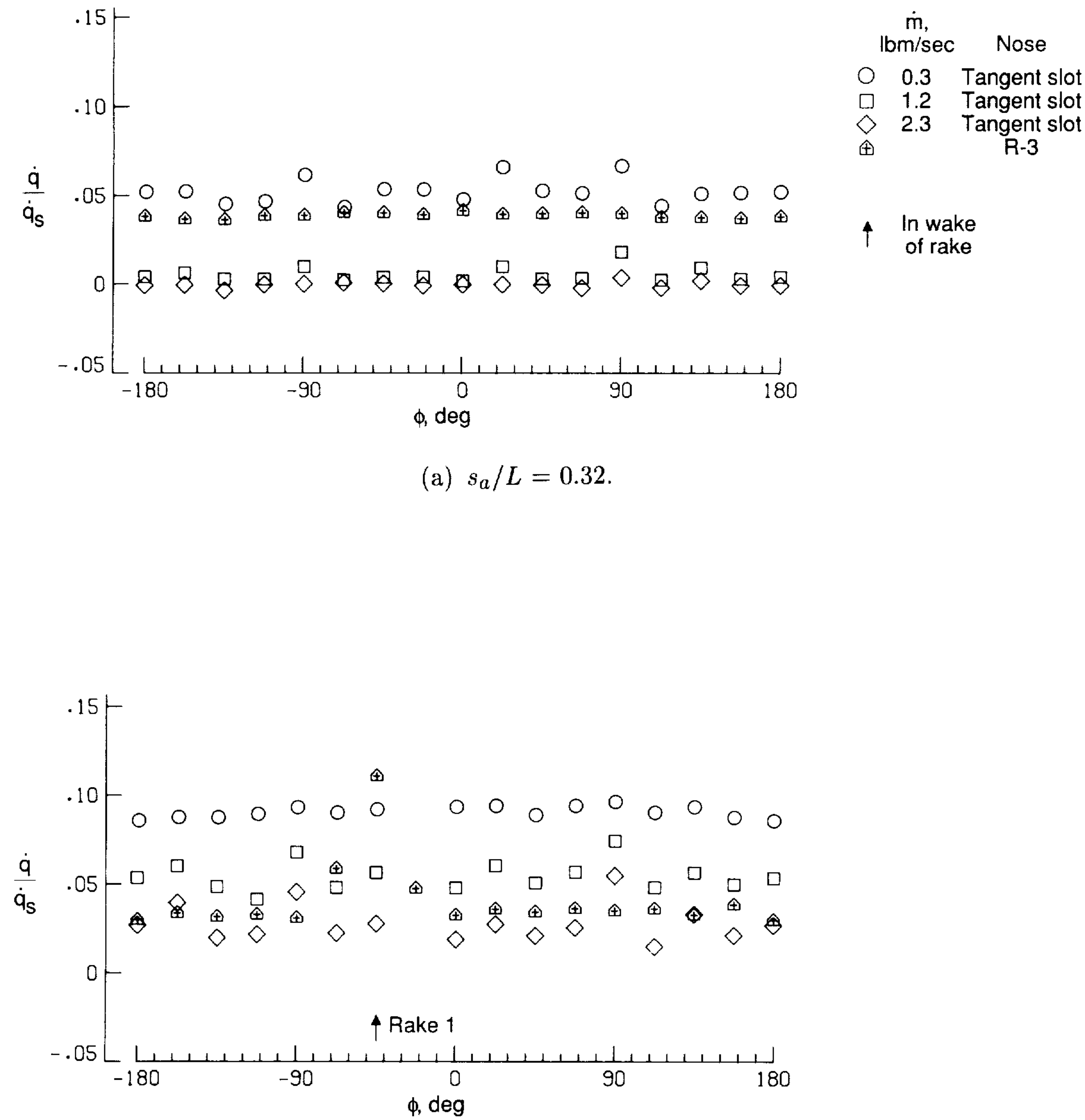

(a) $s_a/L = 0.32$.

(b) $s_a/L = 0.53$.

Figure 35. Circumferential heat-flux distributions for tangent-slot and baseline R-3 noses.

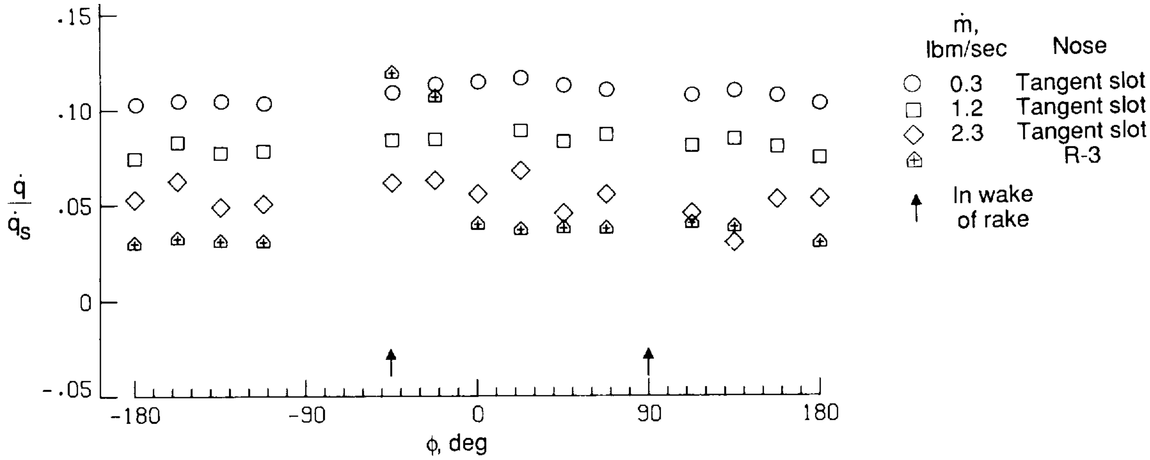

(c) $s_a/L = 0.69$.

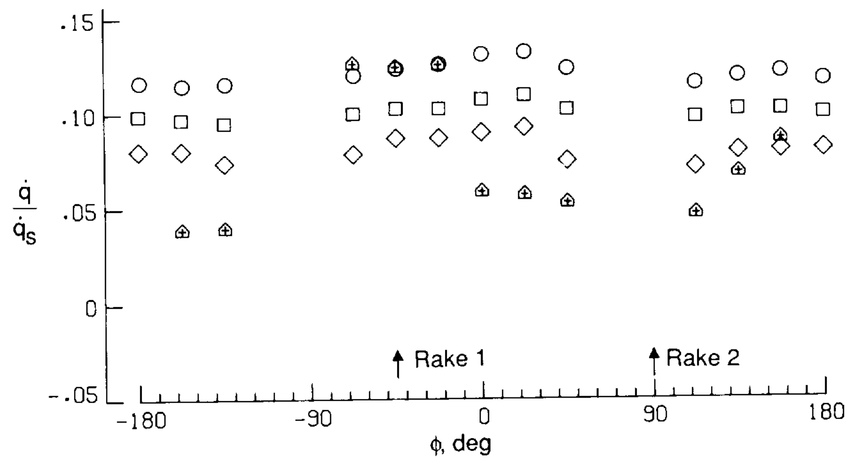

(d) $s_a/L = 0.82$.

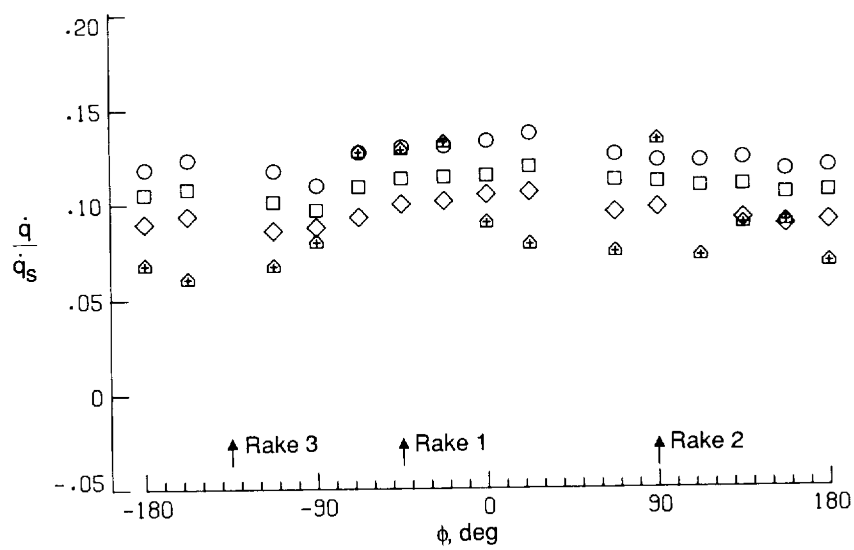

(e) $s_a/L = 0.92$.

Figure 35. Concluded.

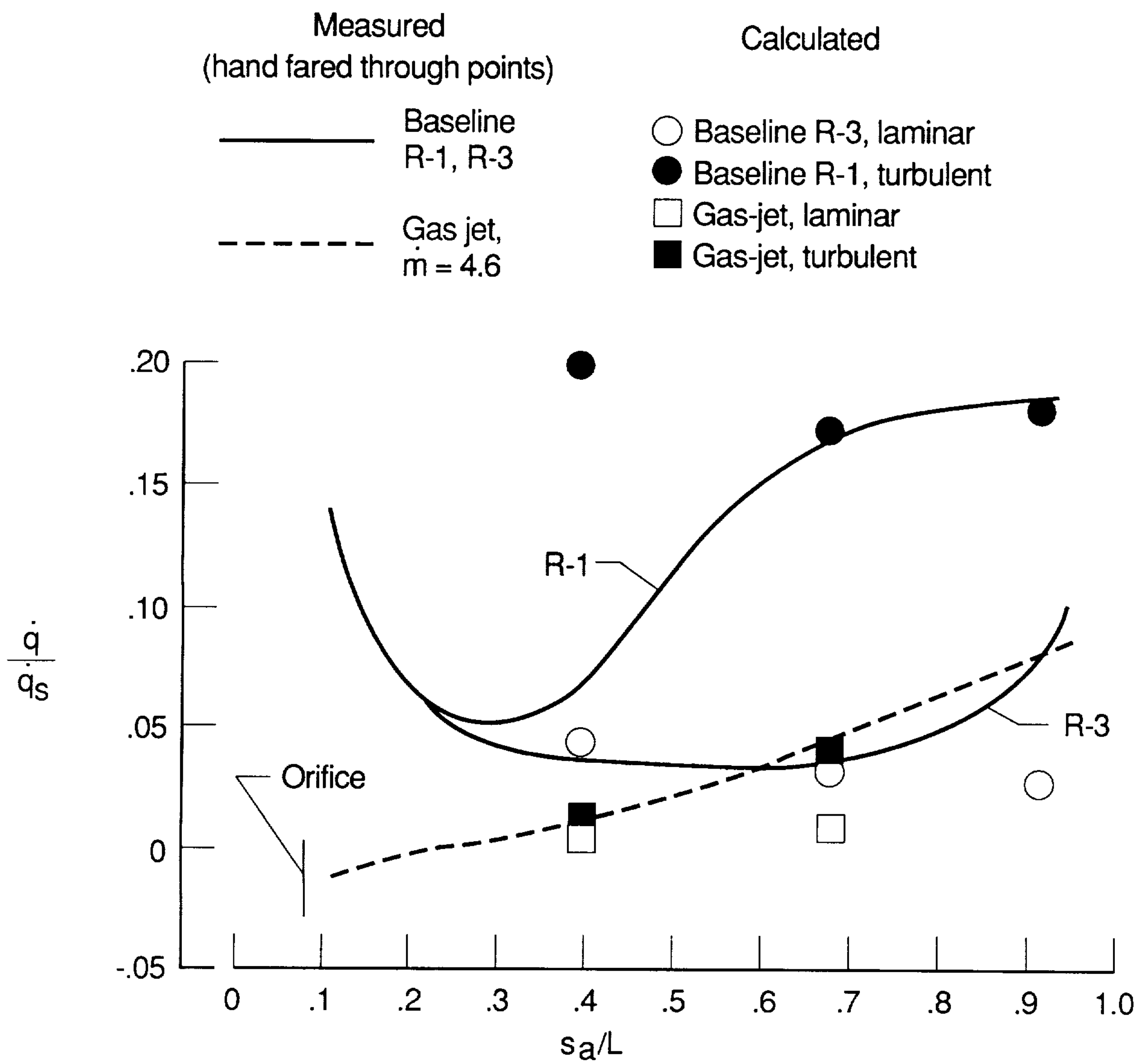

Figure 36. Measured and calculated heat flux for gas-jet, R-3, and R-1 noses.

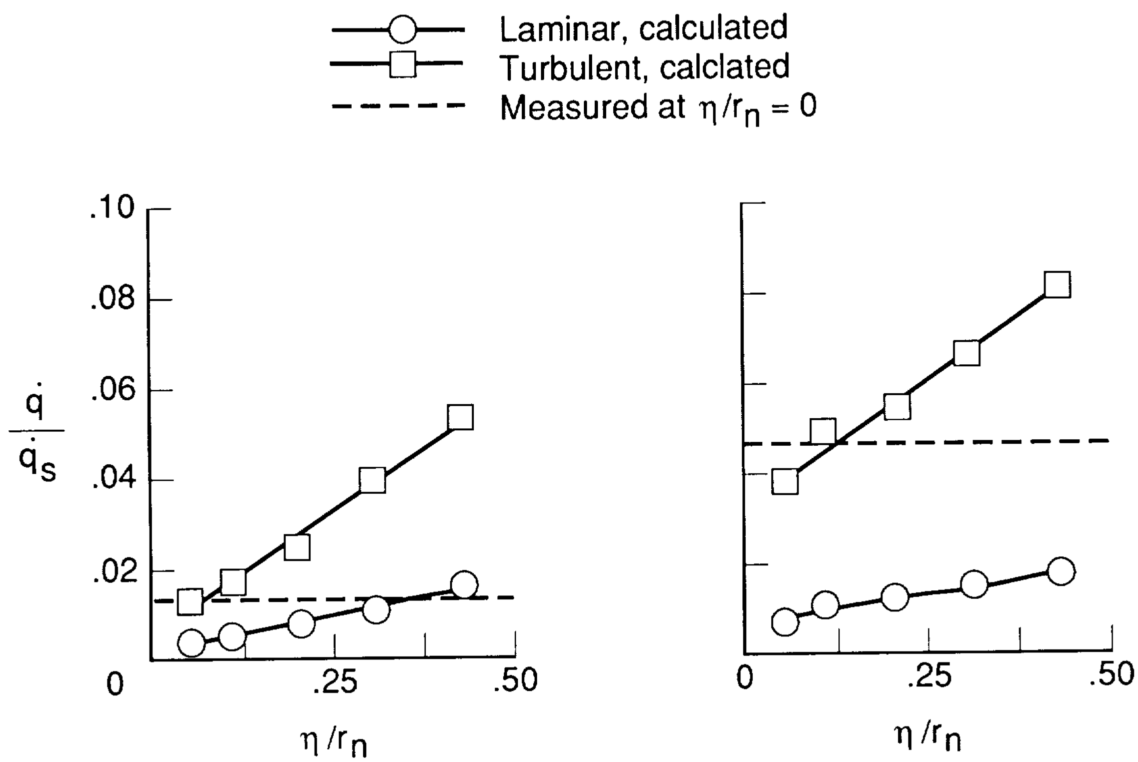

(a) $x/r_n = 7.1$.

(b) $x/r_n = 12.6$.

Figure 37. Measured gas-jet heat flux and heat flux calculated using shock-layer properties. $\dot{m} = 4.6$ lbm/sec; $r_n = 4.1$ in.

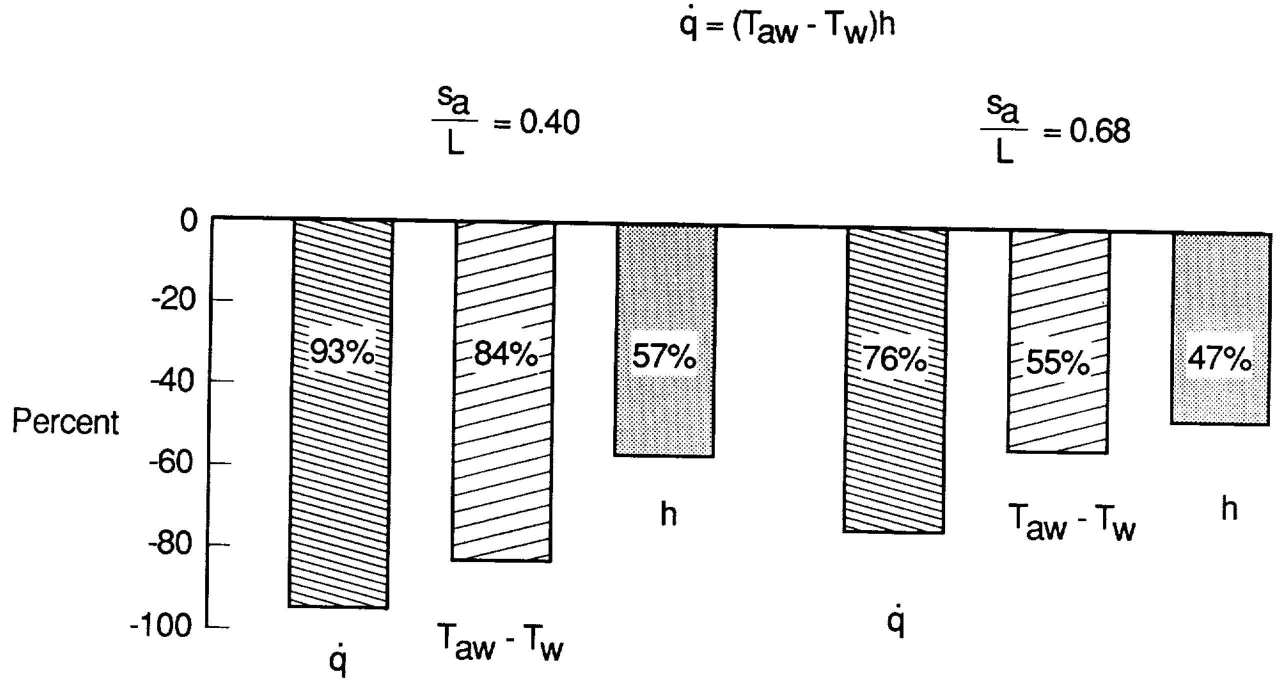

(a) Reduction in $\dot{q}$, $T_{aw} - T_w$, and h.

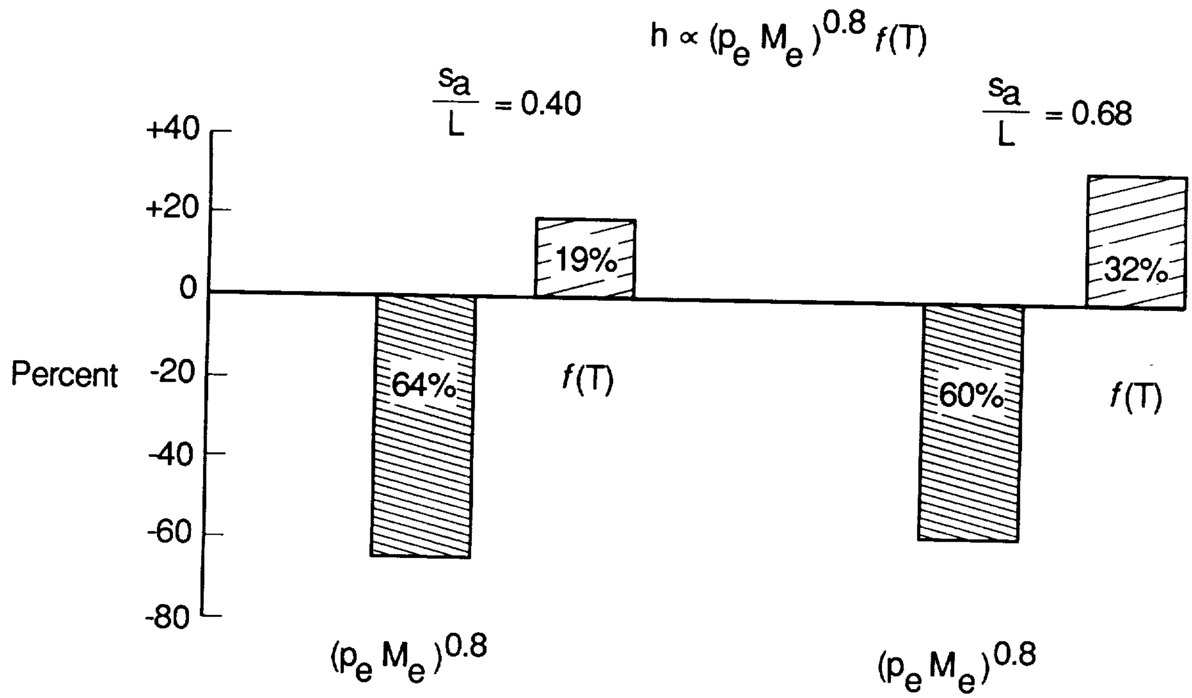

(b) Change in components of h.

Figure 38. Breakdown of heat-flux drivers with gas jet nose for $\dot{m} = 4.6$ lbm/sec.

NASA
National Aeronautics and Space Administration

Report Documentation Page

1. Report No. NASA TP-2786	2. Government Accession No.	3. Recipient's Catalog No.
4. Title and Subtitle Gas-Jet and Tangent-Slot Film Cooling Tests of a 12.5° Cone at Mach Number of 6.7		5. Report Date May 1988
		6. Performing Organization Code
7. Author(s) Robert J. Nowak		8. Performing Organization Report No. L-16148
9. Performing Organization Name and Address NASA Langley Research Center Hampton, VA 23665-5225		10. Work Unit No. 506-40-21-01
		11. Contract or Grant No.
12. Sponsoring Agency Name and Address National Aeronautics and Space Administration Washington, DC 20546-0001		13. Type of Report and Period Covered Technical Paper
		14. Sponsoring Agency Code

15. Supplementary Notes

16. Abstract

Tests were conducted in the Langley 8-Foot High-Temperature Tunnel to determine the aerothermal effects of gaseous nitrogen-coolant ejection on a 3-ft base-diameter, 12.5° half-angle cone. Free-stream Mach number, total temperature, and unit Reynolds number per foot were 6.7, 3300°R, and 1.4×10^6, respectively. Two coolant ejection noses were tested – an ogive frustum with a forward-facing 0.8-in-radius gas-jet tip, and a 3-in-radius hemisphere with a 0.243-in-high rearward-facing tangent slot. Data include surface pressures and heating rates, shock shapes, and shock-layer profiles; results are compared with no-cooling data obtained with 1-in-radius and 3-in-radius solid noses. Surface pressures were reduced with gas-jet ejection but were affected little by tangent-slot ejection. For both gas-jet and tangent-slot ejection, high coolant flow rates reduced heating even far downstream from the region of ejection; however, low coolant flow rates caused transition to turbulence and increased heating. Shock-layer profiles of pitot pressure, Mach number, and total temperature were reduced for both gas-jet and tangent-slot ejection. Insight into the gas-jet heat-flux mechanisms was obtained by using shock-layer rake data and established, no-cooling, heat-transfer equations.

17. Key Words (Suggested by Authors(s)) Heat-transfer data, Pressure data, Shock-layer data, Shock shape, Angle of attack	18. Distribution Statement [redacted] Subject Category 34

19. Security Classif.(of this report) Unclassified	20. Security Classif.(of this page) Unclassified	21. No. of Pages 83	22. Price A05

NASA FORM 1626 OCT 86 [redacted]

NASA-Langley, 1988